FROM FRESH- TO SEA-WATER AND FROM SHALLOW TO DEEP - A TURBULENCE PERSPECTIVE

A Dissertation

by

SERGEY MOLODTSOV

Submitted to the Graduate and Professional School of
Texas A&M University
in partial fulfillment of the requirements for the degree of

DOCTOR OF PHILOSOPHY

Chair of Committee,	Ayal Anis
Co-Chair of Committee,	Rainer M.W. Amon
Committee Members,	Alejandro H. Orsi
	Kyeong Park
	Julio Sheinbaum
Head of Department,	Shari Yvon-Lewis

August 2021

Major Subject: Oceanography

ABSTRACT

Turbulence is an important process governing the mixing of fluid properties in nature. Nowadays, it remains a complex topic in oceanography, and other fields, due to its inherent stochastic nature. It is important in many areas of research, and there are many unresolved problems regarding the understanding of turbulence and the role it is playing in different processes. In my research, I am trying to address some of those questions.

The first problem which I am investigating is related to the study of turbulence within the mesoscale eddy system. For the first time, turbulence was estimated from microstructure velocity and temperature fluctuations measured within an anticyclonic eddy originating from the Loop Current in the Gulf of Mexico. This study aims to provide a unique set of measurements that will allow resolving the dynamics of physical and biogeochemical processes related to eddies and shelf processes.

The second problem is devoted to the parameterization and estimation of a gas exchange coefficient in river environments. The gas exchange between water bodies and the air is difficult to measure. Thus the Wanninkhof methodology (Wanninkhof et al., 2014) to approximate air-sea gas exchange solely based on wind speed is widely used. However, this approximation may not work in river environments. In rivers, water currents may play a more important role in governing gas exchange than wind. In this study, I compare different approaches to estimate the gas exchange coefficients using field observations during the summer of 2016 on the Yenisei River.

ACKNOWLEDGEMENTS

I would like to thank my committee chair and co-chair, Dr. Anis and Dr. Amon, and my committee members, Dr. Orsi, Dr. Sheinbaum, and Dr. Park, for their guidance and support throughout the course of this research.

I also want to thank the captain, scientists, and crew of R/V Pelican for their help during the DWDE cruise. I appreciate the work of the Currents Group at the University of Hawaii for the acquisition and preprocessing of the shipboard ADCP data and Alejandro Domínguez for final processing. And I am grateful to Dr. Meunier for constructive discussions. Without the help of the captain and crew of the Yak and the team at the Sukachev Institute, including A. Prokushkin, A. Panov, A. Rubtsov, V. Zyryanov, M. Korets, I. Solnyshkin, N. Sidenko, R. Kolosov the Siberian study wouldn't be possible.

I want to thank my previous scientific advisors: Dr. Nikolai Dronin, Dr. Andrei Kirilenko and Dr. Xiaodong Zhang for showing me an exciting world of science.

Finally special thanks go to my friends and colleagues and the department faculty and staff for making my time at Texas A&M University a great experience. Especially I wanted to thank Dr. Tatiana Williford for help and moral support.

CONTRIBUTORS AND FUNDING SOURCES

Contributors

This work was supervised by a dissertation committee consisting of Professor Ayal Anis [advisor], Professor Rainer M.W. Amon [co-advisor], Professor Alejandro H. Orsi, and Professor Kyeong Park of the Department of Oceanography/Marine Sciences, and Professor Julio Sheinbaum of the Department of Physical Oceanography at Center for Scientific Research and Higher Education.

Without the dedication of the glider pilots of the Geochemical and Environmental Research Group (GERG) at Texas A&M, led by Senior Marine Instrumentation Specialist Mrs. Karen Dreger, this study would not have been possible.

Funding Sources

Gulf of Mexico research has been funded by the Mexican National Council for Science and Technology - Mexican Ministry of Energy - Hydrocarbon Fund, project 201441. This is a contribution of the Gulf of Mexico Research Consortium (CIGoM). We acknowledge PEMEX's specific request to the Hydrocarbon Fund to address the environmental effects of oil spills in the Gulf of Mexico.

Siberia study was funded by US NSF grant OPP-1642851 and the Russian RSF Grant #14-24-00113

NOMENCLATURE

AAIW	Antarctic Intermediate Waters
ADCP	Acoustic Doppler Current Profiler
c	Incident Internal Wave Angle Relative to Horizontal Plane
C_{Da}	Drag Coefficient
Cp	Heat Capacity
CTD	Conductivity Temperature and Depth
DIC	Dissolved Inorganic Carbon
DOC	Dissolved Organic Carbon
FFT	Fast Fourier Transform
GHG	Green House Gases
GOM	Gulf of Mexico
GOTM	General Ocean Turbulence Model
H	Heat Flux
K_p	Eddy Diffusivity
LC	Loop Current
LCE	Loop Current Eddy
LE	Latent Heat Flux
L_{MO}	Monin–Obukhov Length Scale
LOW	The “Law of The Wall”
L_T	Thorpe length scale
LW	Net Long Wave Radiation
ML	Mixed Layer

MLD	Mixed Layer Depth
MLE	Maximum Likelihood Estimate
N	Buoyancy Frequency
NACW	North Atlantic Central Waters
PSD	Power Spectral Density
Re	Buoyancy Reynolds Number
Ri	Richardson Number
R_ρ	Density Ratio
S	Vertical Shear
SACW	South Atlantic Central Water
SE	Sensible Heat Flux
SEM	Small Eddy Model
S(k)	Spectrum of Temperature Gradients
SSH	Sea Surface height
SUW	Subtropical Underwater
SW	Surface Water
SW	Net Incoming Shortwave Radiation
TKE	Turbulent Kinetic Energy
Tu	Turner Angle
u_{10}	Wind speed at 10 m Height
u_s	Velocity Scale
u_*	Friction Velocity
w	vertical velocity

α	Thermal Expansion Coefficient
β	Saline Contraction Coefficient
β	Buoyancy Flux
Γ^{DD}	Mixing Efficiency Ratio
ε	Turbulent kinetic energy dissipation rate
k	Wavenumber
k_B	Batchelor Cutoff Wavenumber
k_T	Molecular Thermal Diffusivity
$\phi(k)$	Wavenumber Spectrum
γ	Buoyancy Flux Ratio
χ_T	Temperature Variance Dissipation Rate
ν	Kinematic Viscosity
γ	Continental Slope Inclination Angle Relative to Horizontal Plane
ρ_{atm}	Density of Air
ρ_{water}	Density of Water
τ	Surface Wind Stress

TABLE OF CONTENTS

LIST OF FIGURES

FIGURE Page

LIST OF TABLES

1. INTRODUCTION

The Earth system is constantly undergoing changes on different spatial and temporal scales. In many cases, this is related to the exchange of properties between different components of the earth system. In many cases, it is associated with the fluxes of energy and elements between the geospheres. For example, recent climate change is posing a threat to humanity. It is associated with the increased greenhouse gas (GHG) concentrations released into the atmosphere due to anthropogenic activity, leading to the Green House effect and overall global warming (IPCC AR5). This, in turn, affects many mechanisms within the Earth system as the system state tries to find a new balance by distributing, e.g., the excess of heat and carbon from the atmosphere to the global ocean and other aquatic and terrestrial environments (Wanninkhof et al., 2013; Gleckler et al., 2016). This can trigger variable feedbacks and complicates overall predictions (e.g., Friedlingstein et al., 2003; Soden and Held, 2006). Thus, studies quantifying the different fluxes within and between the geospheres are helping in understanding the overall global dynamics.

The fluxes in the earth system are often dependent on mixing efficiency in the region of interest, whether the ocean interior or the air-water interface. In many cases, in-situ observations of turbulence can shed light on more broad processes governing the Earth system. Moreover, turbulence observations are very scarce as it is challenging to collect accurate observational data of mixing. The lack of such observations in several critical regions of interest led to an incomplete picture of biogeochemical fluxes and served as the motivation for this dissertation.

In this study, we are trying to understand the dynamics associated with turbulence during observational missions in different parts of Earth's hydrosphere. First, we were interested in how

mesoscale dynamics in the Gulf of Mexico (GOM) affect turbulence and vertical mixing patterns in the GOM. The measurements and analysis targeted two important “hot spots” of elevated mixing in the GOM. The first “hot spot” is related to the Loop Current Eddy (LCE) activity, as LCE is the main driver of mesoscale variability in the GOM (Elliott 1982). The second “hot spot” can be found in regions with rough bathymetry. Such conditions are common in the western GOM with a steep continental slope. Both of our “hot spot” missions were unprecedented in that we deployed a glider with an integrated microstructure sensor in these specific GOM environments. Results of these observations represent a unique dataset of direct microstructure turbulence observations.

The vertical structure of mixing within LCE is important to understand better the heat and salt fluxes associated with the eddy. LCE is formed by the meandering of the loop current (LC) (Rudnick et al., 2015). Thus they are bringing different water masses to the GOM, especially at ~150 m depth where Caribbean Underwater is situated (Portela et al., 2018). Thus, the water within the eddies has higher heat and salt content than the surroundings. The current study helps understand and quantify the heat and salt fluxes associated with the decay and the overall lifespan of an eddy.

The motivation behind the second mission came from the lack of direct turbulence measurements in the western GOM. The region has a steep continental slope where we expect to see higher mixing caused by internal wave breaking (Munk 1966; Polzin et al., 1997). The second glider mission with microstructure package helped identify the regions with elevated mixing rates and quantify the strength of turbulent mixing.

Besides studying the mixing-related processes in open ocean environments, this dissertation also investigated the role of turbulence for gas exchange in freshwater river

environments. Large boreal rivers in Siberia connect the boreal forests of Russia with the Arctic Ocean and serve as a pathway of lateral carbon export towards the ocean. In the context of a rapidly changing climate and permafrost melt, this region becomes an important "blank spot" in quantifying the Global Carbon Cycle. The rate of gas exchange between such big rivers and the atmosphere is still poorly constrained and not well quantified. The observational campaign in Siberia in Summer 2016 led to the collection of a unique dataset along a 2000 km section of Yenisei River to improve our understanding of the role of turbulent mixing. We were particularly interested in coming up with a new way of parametrizing the gas exchange at the air-water interface using current observations and determining the mixing in the surface waters of the river. A direct determination of gas exchange coefficients based on turbulence measurements has not been attempted before. We wanted to see how well the direct measurements compare to other approaches of estimating the gas exchange coefficient. The more commonly used approaches are based on wind speed (Wanninkhof 2014) or the topography paired with discharge measurements (Raymond et al. 2012). This part of the dissertation involves a method development to approximate the air-water gas exchange using an acoustic Doppler current profiler (ADCP) supplemented by measurements of wind speed, radiation, and high-frequency temperature profiles.

Observational oceanography is a challenging field as a sampling of the ocean is associated with poor spatial and temporal resolution and requires an enormous effort with many problems to be addressed. This dissertation tried to cover some of the poorly resolved phenomena within the aquatic environment and address several problems which were not well studied before. Thus Chapter 2 and Chapter 3 focus on the open ocean, using turbulence

measurements to target important features of the GOM in terms of mixing. Chapter 4 is focused on using turbulence measurements to study the gas exchange in a large boreal river.

2. TURBULENT MIXING IN A LOOP CURRENT EDDY FROM GLIDER-BASED MICROSTRUCTURE OBSERVATIONS*

2.1 *Introduction*

The dynamics of mesoscale eddies in the world ocean is an area of intensive oceanographic research. Eddies influence the upper ocean properties by increasing diapycnal and isopycnal mixing and creating shear on the edges and underneath the eddy core (Olson, 1991; Mukherjee et al., 2016). Elevated vertical velocities associated with eddies affect vertical transport of the mass (Baird and Ridgway 2012), heat (Jayne and Marotzke, 2002), and nutrients which, in turn, affect biogeochemical properties and biological production (McGillicuddy et al., 1998; Everett et al., 2012; Mahadevan et al., 2012). Eddies also affect the surface ocean properties by which they influence the air-sea fluxes (Wunsch, 1999; Colas et al., 2012; Villas Bôas et al., 2015). In particular, the parameterization of mesoscale eddies in global ocean models represents one of the main problems for numerical modelers (e.g., Gent and Mcwilliams 1990; Treguier et al., 1997; Griffies et al., 2016). Observational studies of ocean eddies, such as reported here, are a crucial step for the advancement of our understanding of their dynamics as well as their role in ocean circulation.

The Gulf of Mexico (GOM) is one example of a region with intense mesoscale eddy activity, both cyclonic and anticyclonic. The eddies are chiefly produced by the Loop Current (LC) and are the main contributors to the mesoscale variability in the GOM. The baroclinic-barotropic instability of the LC, entering through the Yucatan Channel, forms cyclonic eddies, which in turn control the separation of anticyclonic Loop Current Eddies (LCEs) (Rudnick et al., 2015; Jouanno et al., 2016). After detachment from the LC, LCEs drift westwards and may persist in the GOM for months before they finally dissipate. LCEs are robust geostrophic features with diameters on

*Reprinted with permission from "Turbulent mixing in a Loop Current Eddy from glider-based microstructure observations" by S Molodtsov, A Anis, RMW Amon, P Perez-Brunius, 2020. Geophysical Research Letters, 47(14).

the order of 200-400 km and elevated sea surface heights (SSH). In addition to their importance for the dynamical processes in the GOM, LCEs contribute to hurricane development and intensification (Shay et al., 2000). Furthermore, LCEs variability appears to affect climate extremes in North America through their effect on surface heat fluxes (Putrasahan et al., 2017).

Despite the significance of LCEs as the main player in the dynamics of the GOM, the associated mixing processes are still not well understood. Here, we present the analysis of observations collected during the first glider mission in an anticyclonic LCE ("Poseidon" Meunier et al., 2018) in fall 2016. Double diffusion processes are common attributes of eddies in the ocean (Bebieva and Timmermans, 2016; Fine et al., 2017), and our findings indicate that LCE is not an exception.

2.2 *Data and Methods*

2.2.1 *Mission overview*

This study is based on data from a Webb Research G2 Slocum ocean glider deployed in fall 2016 and spanning a week from October 14 to 21. Our glider was equipped with a Rockland Scientific micro-Rider microstructure sensors suite that included two velocity shear sensors (Osborn, 1974), two FP07 fast response thermistors, a pressure sensor, and two accelerometers. The general payload included a conductivity-temperature-depth (CTD) sensor, Wet Labs ECO PuckTriplet (Chlorophyll a, colored dissolved organic matter (CDOM), Backscatter), and Rinko DO sensors.

The target of the deployment was an anticyclonic eddy ("Poseidon", Meunier et al., 2018) that separated earlier from the LC and was moving westwards (Fig. 2.1).

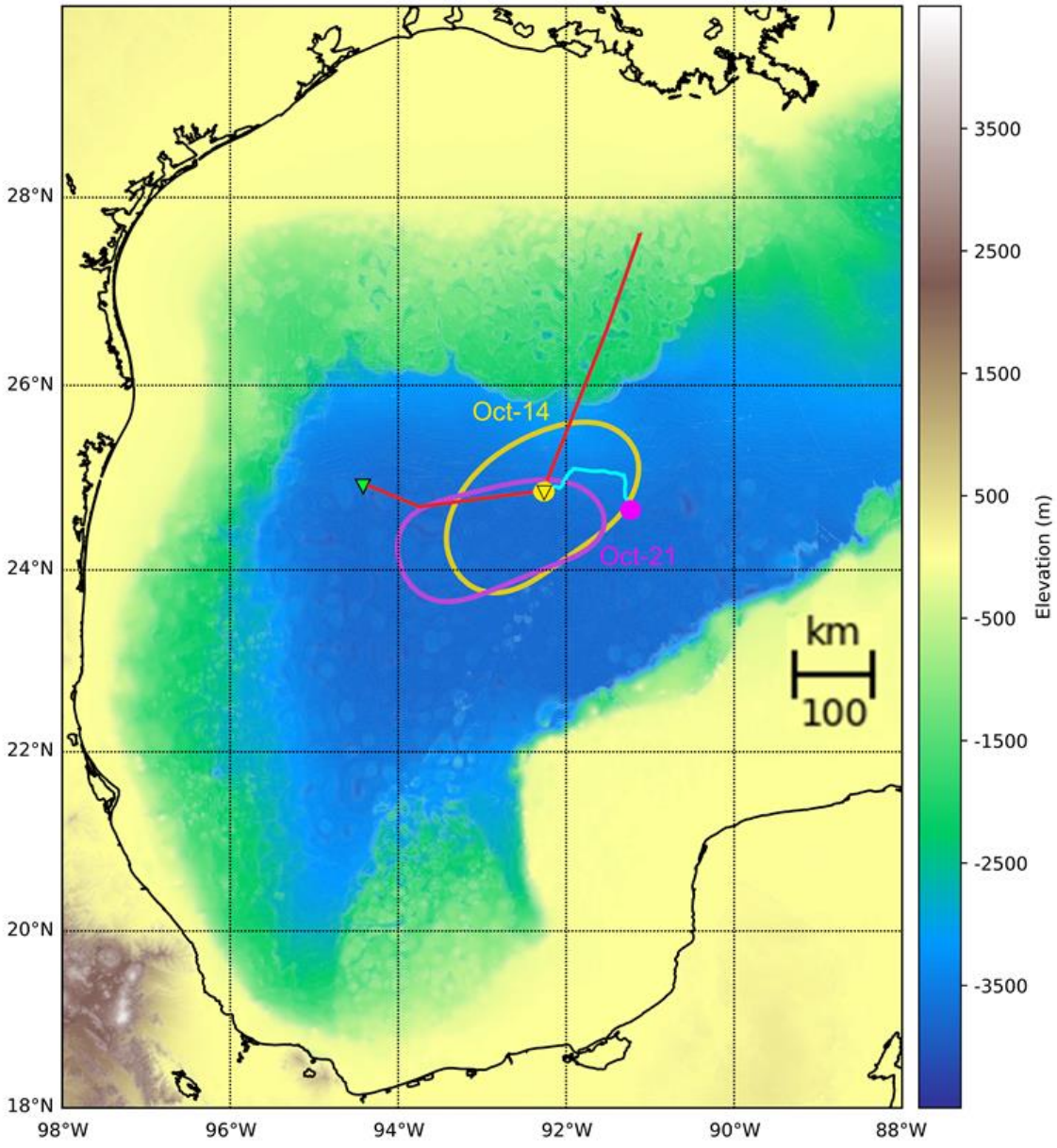

Figure 2.1. Bathymetry map with LCE eddy contours (0.6 m of absolute dynamic topography) for October 14 (yellow) and October 21 (magenta); start of glider mission/1st shipboard-mounted ADCP section for profiles from inside the eddy core (yellow dot); end of mission (magenta dot); 2nd shipboard-mounted ADCP section for profiles from outside the eddy core (green triangle);

glider (cyan) and ship (red) tracks. Sea surface height data was obtained from http://marine.copernicus.eu/services-portfolio/access-to-products/.

Shipboard-mounted Workhorse 75 kHz ADCP data from a transect through the eddy was used in this study to complement the glider-based observations. The ADCP sampling rate was set to 1 Hz, with profiles averaged and logged every 5 minutes. Data processing was done using the CommonOceanographicDataAccessSystem (http://currents.soest.hawaii.edu/docs/adcp_doc/index.html)

2.2.2 *Microstructure data*

The micro-Rider shear sensors provide direct measurements of micro-scale velocity shear allowing estimation of TKE dissipation rates (ε) by integrating the wavenumber (k) spectrum (ϕ):

$$\varepsilon = 7.5\nu \int_{k_l}^{k_u} \phi(k) dk \qquad (2.1)$$

where ν is the kinematic viscosity, and k_l and k_u are the lower and upper integration limits, respectively. A modification (McMillan et al., 2016) of the original Nasmyth empirical spectral model (Nasmyth, 1970) was applied to set k_l and k_u. We followed the procedure outlined by Schultze et al. (2017) and used a flight model by Merckelbach et al. (2010), pitch, pressure, and angle of attack to calculate glider velocity. We used the standard MATLAB ODAS package to process the data. Power spectrum densities of microstructure velocity and temperature shear were estimated from 8-s sections of data (with a total of 4096 points), using Fast Fourier transform on 2-s segments; each spectral point was based on 4 FFT segments with 50% overlapping.

A second, indirect method to estimate dissipation rate utilizes the microstructure temperature observations. Fitting observed spectrum of temperature gradients, S(k), to the Batchelor form via adjustment of the Batchelor cutoff wavenumber can thus provide an estimate of ε (Batchelor, 1959):

$$\varepsilon = k_B^4 \, \nu \, k_T^2 \qquad (2.2)$$

where k_B is the Batchelor cutoff wavenumber and k_T is the molecular thermal diffusivity. We used the Maximum Likelihood Estimate method and the procedures outlined in Ruddick et al. (2000) to fit the power spectral density of the observed microstructure temperature gradient spectrum to the theoretical Batchelor form to estimate the microstructure temperature-based ε values.

The double diffusion processes can be assessed with turner angle, $Tu = \tan^{-1}\left(\frac{1+R_\rho}{1-R_\rho}\right)$ (e.g. Babieva et al., 2015), where $R_\rho = \frac{\alpha T_z}{\beta S_z}$ is the density ratio, T_z and S_z are the vertical temperature and salinity gradients, respectively, α is the thermal expansion coefficient and β is the saline contraction coefficient. Tu <-90 or Tu>90 indicates gravitationally unstable conditions: when 72<Tu<90, salt finger regime favorable conditions are present; -90<Tu<-51, the water column is prone to diffusive convection; -45<Tu<45 indicates gravitationally stable conditions.

In addition to Tu we calculated the buoyancy flux ratio γ, which also differentiates different double diffusion regimes

$$\gamma = \frac{R_\rho \Gamma^{DD}}{R_\rho \Gamma^{DD} + R_\rho - 1} \qquad (2.3)$$

where $\Gamma^{DD} = \frac{\chi N^2}{2\varepsilon\left(\frac{\partial T}{\partial z}\right)^2}$ is the mixing efficiency ratio (Inoue et al., 2007); $N^2 = -(g/\rho)\partial\rho/\partial z$, where ρ is the potential density When $0 < \gamma < 1$, salt fingering might be possible and when $\gamma > 1$– conditions are favorable for diffusive convection.

Finally, the buoyancy Reynolds number (e.g. Gargett, 1984), $Re = \frac{\varepsilon}{\nu N^2}$, was calculated, which allows the differentiation between double diffusion and turbulence mixing (Inoue et al., 2007).

2.3 *Results and Discussion*

The observed temperature, salinity, and density fields show a well-defined vertical eddy structure, a surface mixed layer (ML), and the deeper, weakly stratified layers of the GOM (Fig. 2.2). The ML tends to be shallower (~50 m) within the eddy compared to its outside (~70-80 m). Beneath the surface ML, an eddy core, clearly defined by the tracer fields (temperature, salinity, and density), appeared to be well mixed ($N < 0.01$ s^{-1}). Beneath the eddy core was a region with different salt and temperature distribution. The temperature was lower compared to the near-surface and core regions. However, the salinity field showed a maximum in the region underneath the core. Such an "accumulation" of higher salinity levels underneath the eddy core was also observed in other in-situ eddy studies (Kolodziejczyk et al., 2012; Barceló-Llull et al., 2017). Two high salinity "tongues" can be identified on the edge of the eddy, at about 200 m deep, and the formation of such "tongues" is believed to be part of a layering process caused by the formation of temperature/salinity anomalies in a shape of elongated patches beneath the eddy (Menesguen et al., 2009; Meunier et al., 2015). The velocity data from the ship's ADCP also clearly showed the presence of eddy characteristics in the velocity magnitude field (Fig. 2.2d). The velocities in the eddy reached values up to 1 m/s, whereas the background velocities were

found to be less than 0.25 m/s. The eddy's signature is clearly visible down to 400 m and coincides with the scalar and mixing fields from the glider/micro-Rider (Fig. 2.2 and 2.3, respectively).

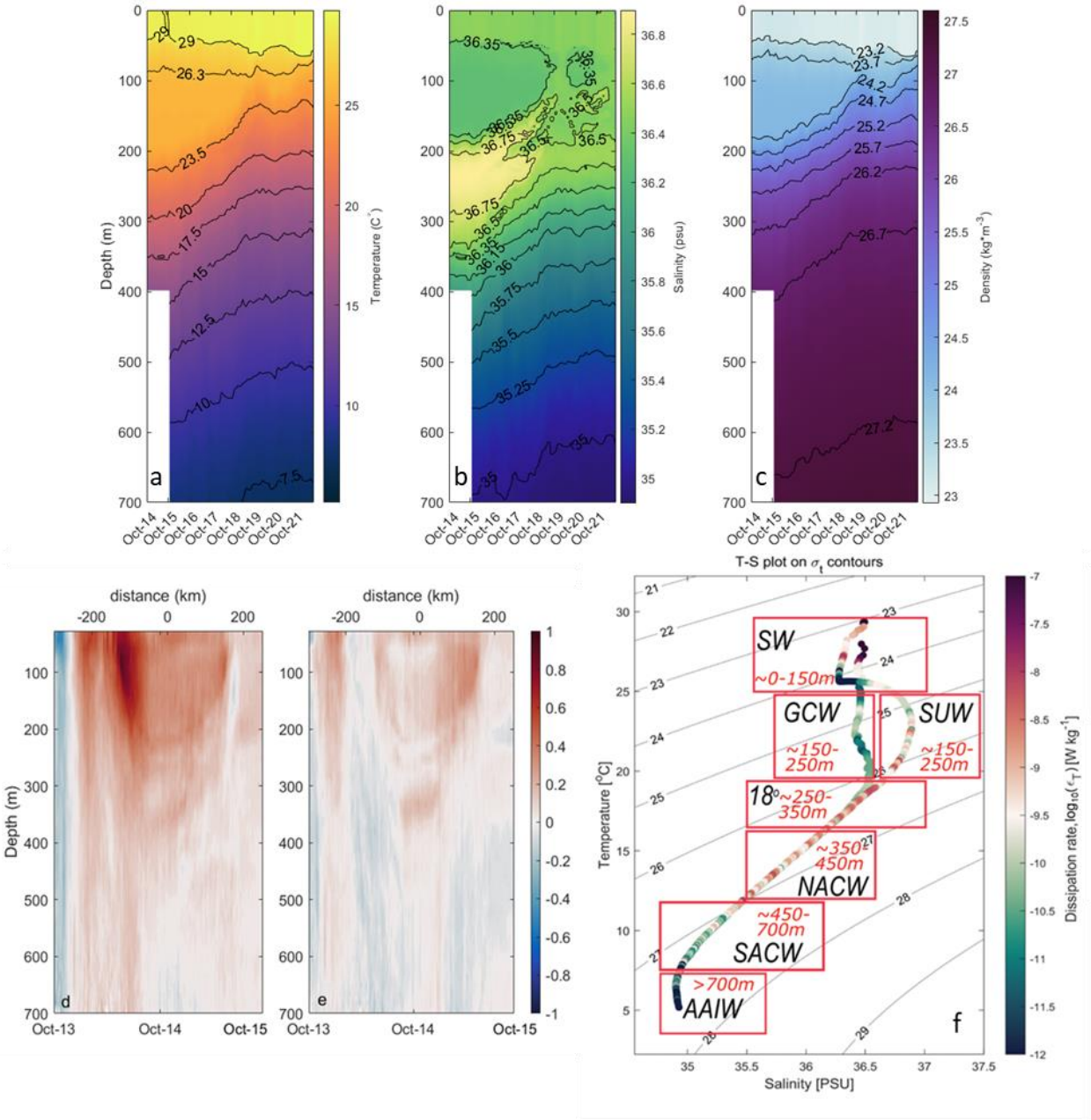

Figure 2.2. Temperature (a), salinity (b), and density (c) profiles during October 14 – October 21, 2016. Radial (d) and azimuthal (e) ADCP velocity profiles (m/s). Top axis represents the distance from the approximate eddy center (yellow dot in Figure 2.1). Temperature–Salinity diagram (e) for the two glider profiles inside/outside the eddy with color-coded ε. Water masses, and their depth ranges (Rivas et al., 2005), are given in the red rectangles: Surface Water (SW,

~0-150 m); Subtropical Underwater (SUW, ~150-250 m) or Gulf Common Water (GCW, ~150-250m); 180 Sargasso Sea Water (~250-350 m); North Atlantic Central Waters (NACW, ~350-450 m); South Atlantic Central Water (SACW, ~450-700 m); and Antarctic Intermediate Waters (AAIW, ~700-1000 m); North Atlantic Deep Water (NADW) is located below 1000m depth and is not observed by glider (Portela et al., 2018).

The eddy structure is also evident in data derived from ECO Puck Triplet observations (Fig. 2.3). Chlorophyll a showed deepening of the Chlorophyll maximum from around 100m outside the eddy to around 120m inside the eddy. The CDOM values showed higher values inside the eddy, comparing to the surroundings. The red light backscattering also indicated the deepening of the surface layer with higher values towards the center of the eddy.

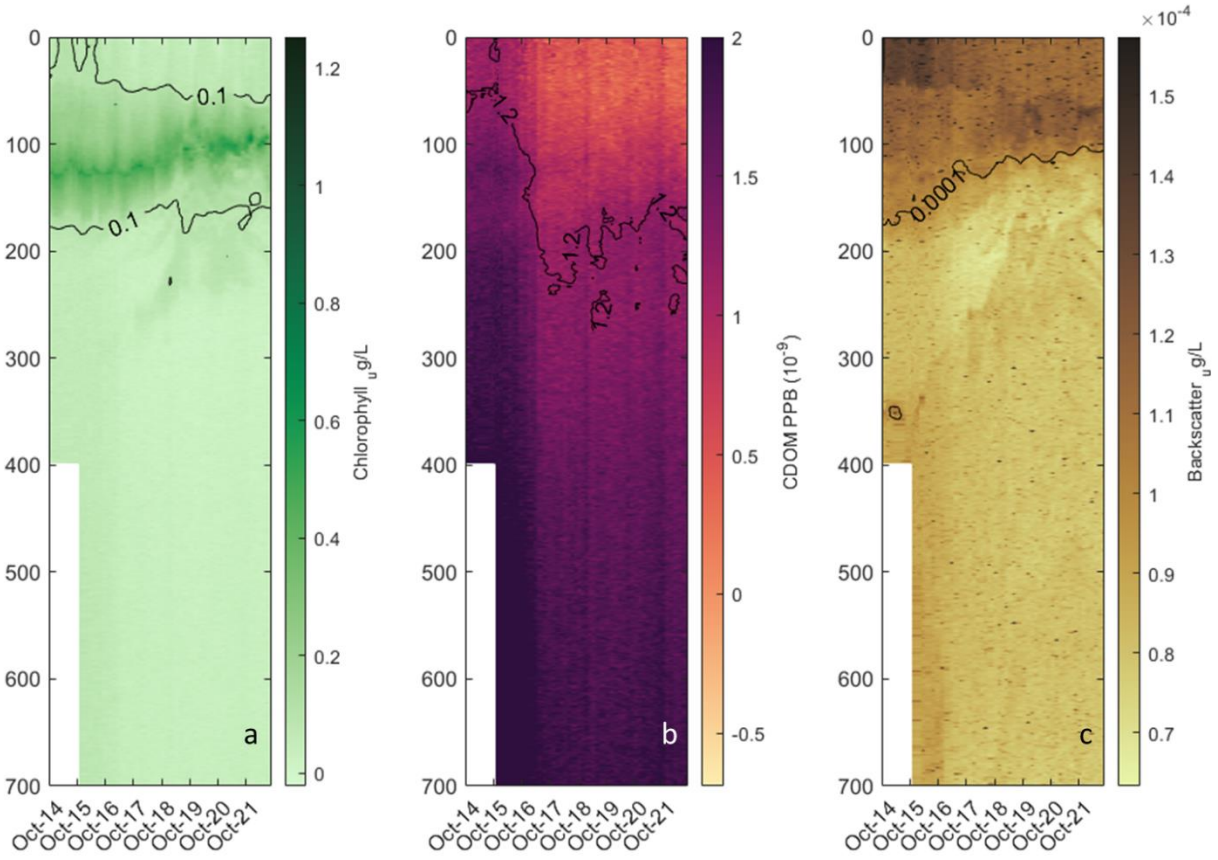

Figure 2.3 Chlorophyl a (a), CDOM (b), and Backscatter (c) profiles during October 14 – October 21, 2016.

The pattern of buoyancy frequency, N, TKE dissipation rates, ε, and eddy diffusivities ($K_p = 0.2\ \varepsilon/N^2$; Osborn, 1980) clearly underline the eddy structure within the water column (Figure 2.4). N values showed well mixed regions in the surface ML, eddy core, and "deep" waters (> 300 m) where $N < 0.01\ s^{-1}$. Elevated values of ε up to 10^{-8} W/kg were found beneath the eddy core, where the highest shear levels occurred based on the ADCP measurements (Figure 2.2d,e). The surface ML can be clearly identified from the elevated ε values up to 10^{-7} W/kg. The

eddy core and "deep water" exhibited quiescent regions with ε values $\leq 10^{-10}$ W/kg. K_p estimates tend to follow the pattern of ε and show the highest values (up to10^{-3} m^2s^{-1}) in the ML. Underneath the eddy core, K_p values are ~10^{-4} $m^2s^{-1,}$ while in deeper waters, $K_p<10^{-7}$ m^2s^{-1}. The results based on the microstructure temperature data allow detection and estimation of very low ε levels of O(10^{-12} W/kg) (Fig. 2.4c), which are more than an order of magnitude lower than estimates based on velocity shear microstructure data.

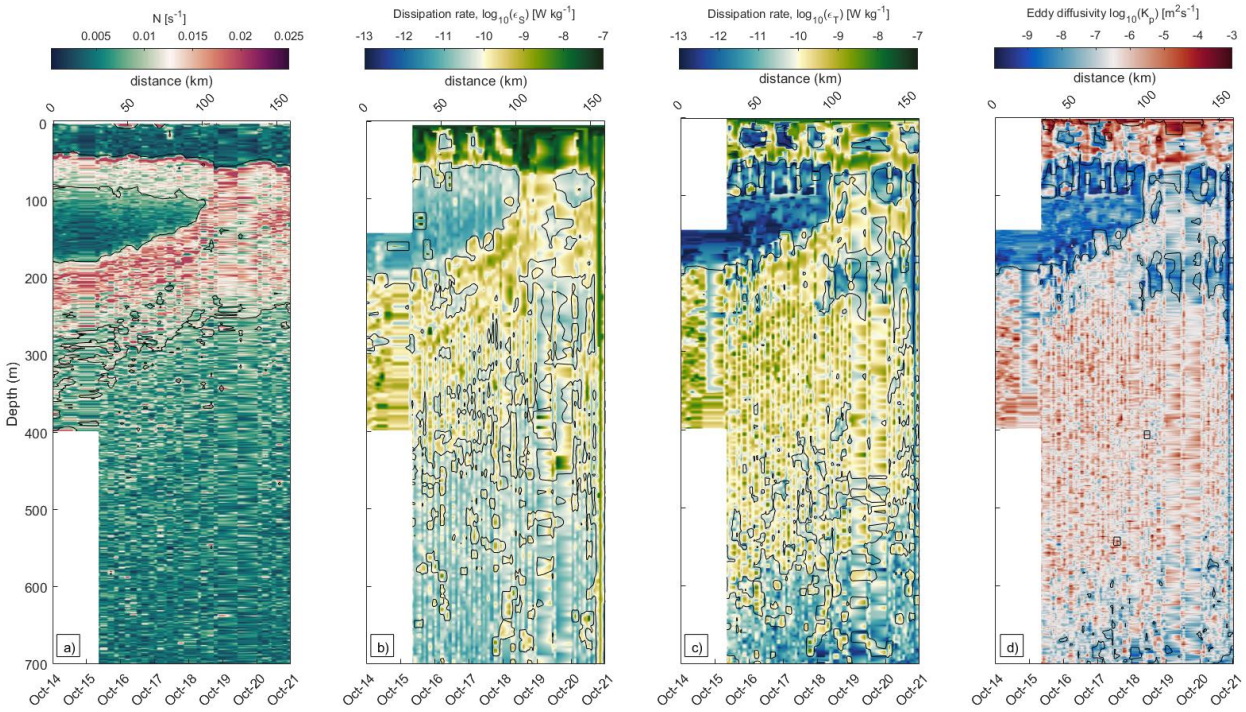

Figure 2.4. Buoyancy frequency N with the contour interval of 0.01 isoline (a); Turbulent kinetic energy dissipation rate ε profiles estimated from microstructure velocity shear (b) and temperature gradient (c) with the contour interval of 10^{-10} isoline; and eddy diffusivities (d; the contours represent 10^{-7} isoline). Top axis same as in Figure 2.2.

Below this patch, around 300 m, the water becomes less salty and colder. The Tu angle in this region is between 72^0 and 90^0, with γ being lower than 1 and Re lower than 25, which indicates salt finger favorable conditions (Fig. 2.5). All parameters indicate salt finger favorable conditions, which can be observed in temperature profiles, just below the eddy (Fig. 2.6a – red square, b). This region also shows small ε values$\leq 10^{-10}$ W/kg; with higher χ values around $\sim 10^{-9}$ $^0C^2/s$ (Fig. 2.6c). On the edge of the SUW patch, the thermohaline intrusion favorable conditions occur. The thermohaline intrusions help lateral mixing of salt and temperature gradients, resulting in lateral heat and salt fluxes. Such intrusions occur in situations when saltier and warmer waters are situated next to fresher and colder ones (e.g. between 150 and 300m, Fig. 2.2). These intrusions represent alternating layers of salt fingers and diffusive convection regions (Fig. 2.6a – blue square, d, e), thus they are characterized by alternating regions of Tu and γ ($72^0<Tu<90^0$, $\gamma<1$ and $-90^0<Tu<51^0$, $\gamma>1$ correspondingly). The turbulence mixing is very weak in this area, with $\varepsilon \sim 10^{-11}$ W/kg and χ values up to $\sim 10^{-8}$ $^0C^2/s$ (Fig. 2.6e).

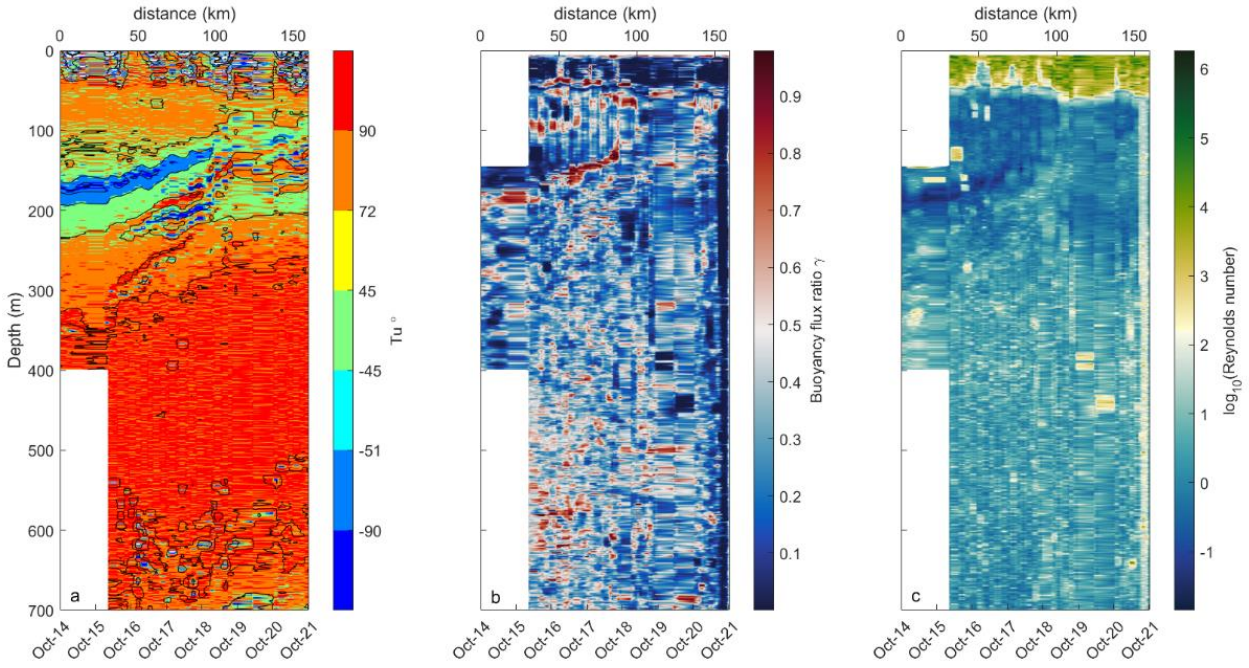

Figure 2.5. Tu (a); γ (b) and Re (c). Top axis same as in Figure 2.2.

Loop current eddies transport Caribbean Underwater to the GOM, which is different from the surrounding Common Gulf Water (Fig. 2.2f). Additional salt and heat brought into GOM through this process were assessed in this study and summed up to be $1.84*10^{19}$ J and $4.59*10^{11}$ kg of salt (integrating the heat and salt within of 2 ^{0}C and 0.3 psu, respectively; Fig. 2.7a,d – areas within the red lines). The rate at which these anomalies dissipate is calculated using microstructure measurements. The two main processes discussed above, and which are known to remove heat and salt from eddies are shear driven mixing beneath the eddy and lateral fluxes through thermohaline intrusions on the flanks of the eddy.

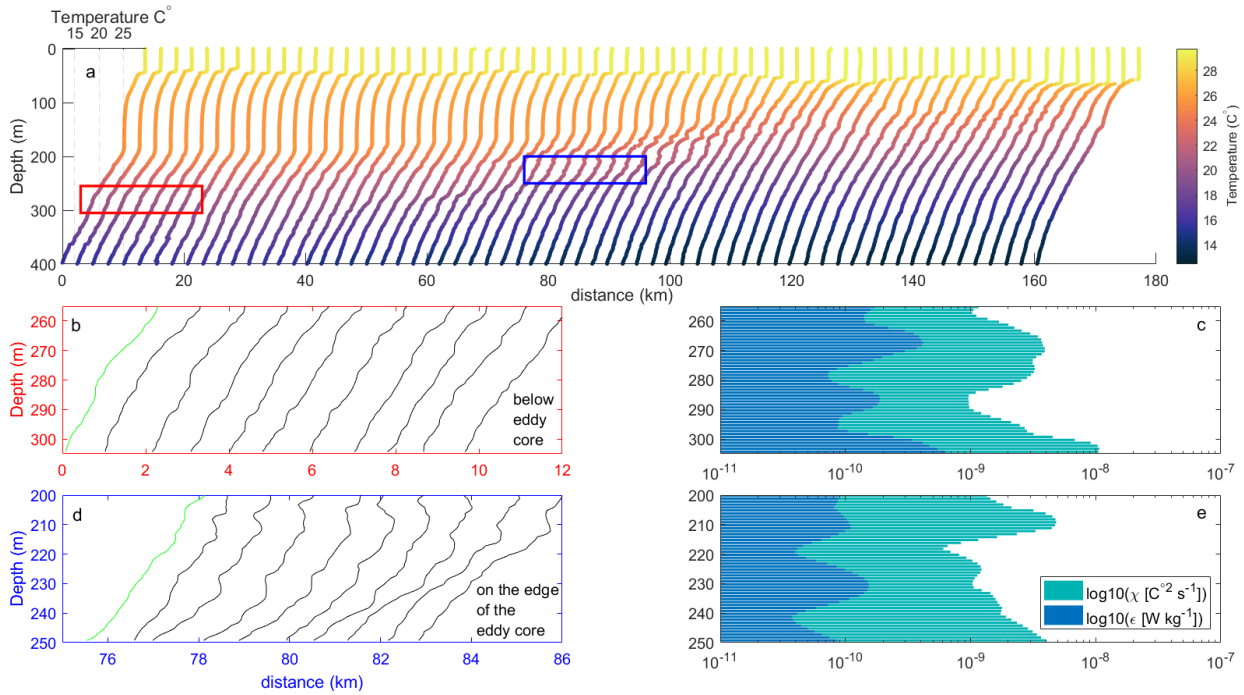

Figure 2.6. Temperature profiles (a) with highlighted regions of salt finger conditions (red square) and thermohaline intrusions (blue square). The temperature scale is shown as the top axis in (a). The profiles are 2^0C shifted. Temperature and ε/χ profiles from the region below the eddy core (b,c) and on the edge of eddy core (e,d). Green profiles in (b) and (d) were used in calculations of ε/χ profiles in (c) and (e) correspondingly. Horizontal axes same as top in Figure 2.2

Shear driven heat (F_H) and salt fluxes (F_s), which occur beneath the eddy core (green box, Fig. 2.7a), were calculated as $F_H = \rho C_p K_T T_z$ and $F_s = K_s S_z$ (Kelley, 1990), where C_p is the heat capacity, T_z and S_z are temperature and salinity vertical gradients, respectively, and assuming that salinity and thermal diffusivities are equal, $K_T = K_s$ with an average value of $1.9*10^{-6}$ m^2/s within the green box in Figure 2.7a. The resulted fluxes for heat and salt were equal to 0.24 W/m^2 and $9.8*10^{-9}$ psu m/s, respectively. Horizontal fluxes associated with lateral

intrusions were calculated using horizontal diffusivities (K_h) calculated $F_h = \rho C p K_H^{sides} Tz$, with horizontal diffusivity $K_H^{sides} = K_T T_z^2 / T_x^2$ (Ruddick et al., 2010) and for salt $K_{Hs}^{sides} = K_S S_z^2 / S_x^2$ (Hebert et al., 1990); T_x, and S_x are the thermal and saline lateral bulk gradients, respectively. We chose the region highlighted with magenta contours on Figure 2.7b,e as this is the region where we observed thermohaline intrusions (Fig. 2.4; Fig. 2.5). Horizontal diffusivities for heat and salt were estimated to be 2.8/0.15 m^2/s, which is in agreement with other studies (Hebert et al., 1990; Ruddick et al., 2010; Fine et al., 2018; Meunier et al. 2020) and calculated averaged fluxes (within regions highlighted with magenta contours on Fig. 2.7b,e) resulted in 2800 W/m^2 and $2.36*10^{-5}$ psu m/s of heat and salt transport. To quantify the total heat and salt transport, we modeled the eddy as having a radius of 100km and a vertical extent of 200m and assumed azimuthal symmetry. The shear-driven turbulent heat flux beneath the eddy was ~7.3 GW, while the horizontal heat flux due to lateral intrusions was ~358 GW. Total salt flux underneath the eddy was ~310 kg/s underneath and $\sim 8.6*10^3$ kg/s on the flanks of the eddy. Time scales for salt and heat fluxes to dissipate the respective anomalies were ~79/46 years for heat/salt shear driven vertical fluxes and 1.6/1.7 years for lateral heat/salt flux. Our results coincide with those of other studies, e.g., Fine et al. (2018) analyzed a smaller arctic eddy using microstructure measurements and found similar decay times of eddy heat anomalies of ~60 years for shear driven fluxes underneath the eddy and ~1year for horizontal fluxes associated with lateral intrusions.

We find that our result contradicts Sosa-Gutiérrez et al. (2020) findings, where the authors state that vertical diffusion is the main factor for the erosion and transformation of LCE. The authors indicate that the strong Northern winds during winter will produce strong turbulent vertical fluxes, which eventually will homogenize the salinity within the LCE. In our study, we clearly observe the quiescent eddy core, which separates the surface ML and salinity maximum

of SUW, which supports that in such conditions, the observed horizontal fluxes will play a key role in the eddy dissipation. However, we agree that under stronger wind forcing the vertical fluxes might play a more important role in the eddy dissipation.

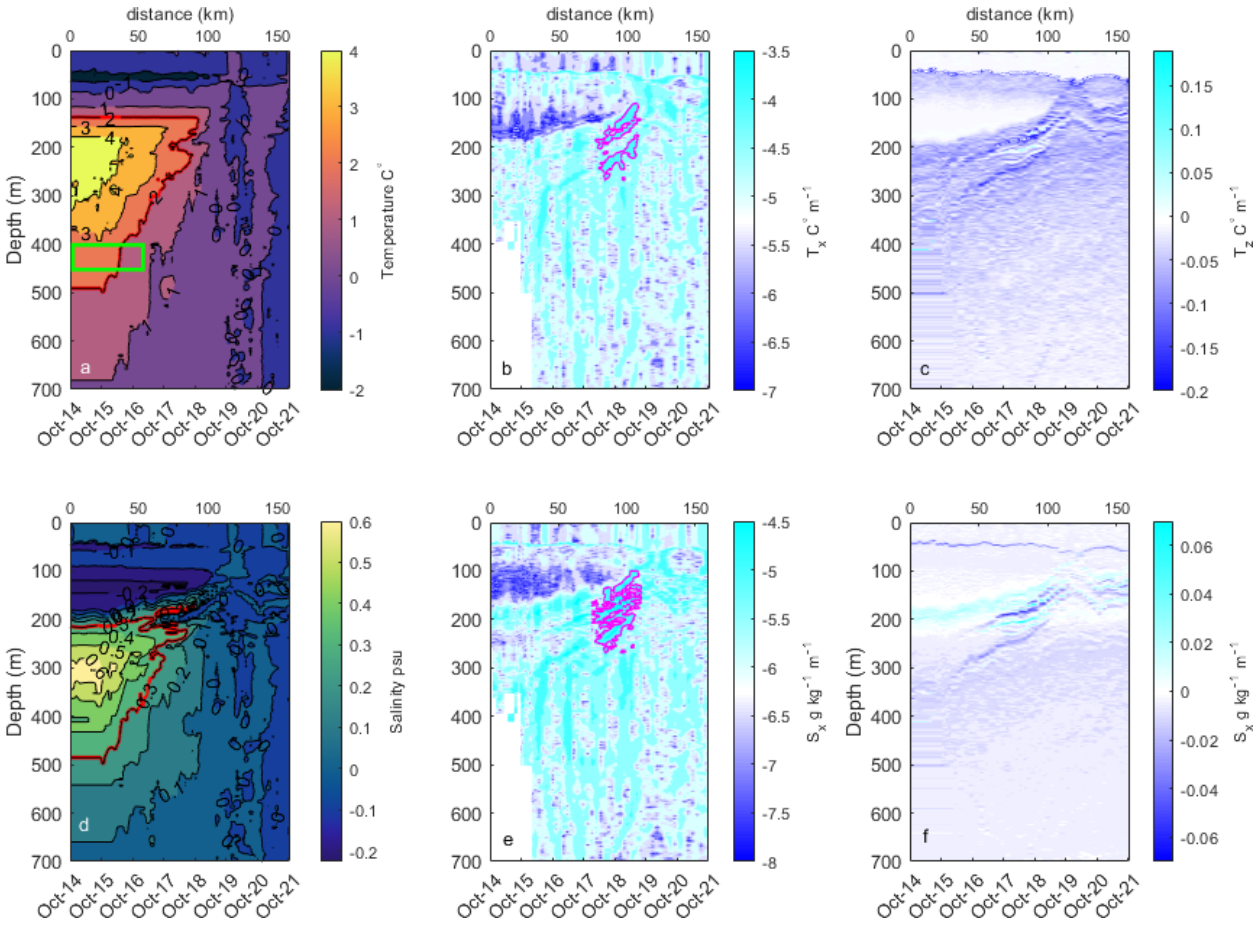

Figure 2.7. Thermal and haline anomalies (a,d), lateral gradients (b,e) and vertical gradients (c,f). Areas within the red lines (panels a,d, within 2 ^{0}C and 0.3 psu isolines, respectively) were used to calculate total heat and salt anomaly. The green box underneath the eddy core in panel (a) was used to calculate vertical fluxes associated with shear; magenta contours in panels (b) and (e) were used to highlight the regions associated with lateral intrusions and relatively large lateral gradients of O(10^{-4} ^{0}C/m)and O(10^{-5} psu/m) for heat and salt, respectively.

Scheifele et al. (2018) demonstrated the ability of temperature microstructure measurements to detect very low levels of TKE dissipation rates. Here we show similar results observed in a Loop Current eddy. Temperature fluctuations spectra followed the theoretical Batchelor spectral shape in very quiescent regions allowing the expansion of the range of ε estimates down to O(10^{-12} W/kg), which is about two orders of magnitude lower is currently possible with shear based microstructure estimates.

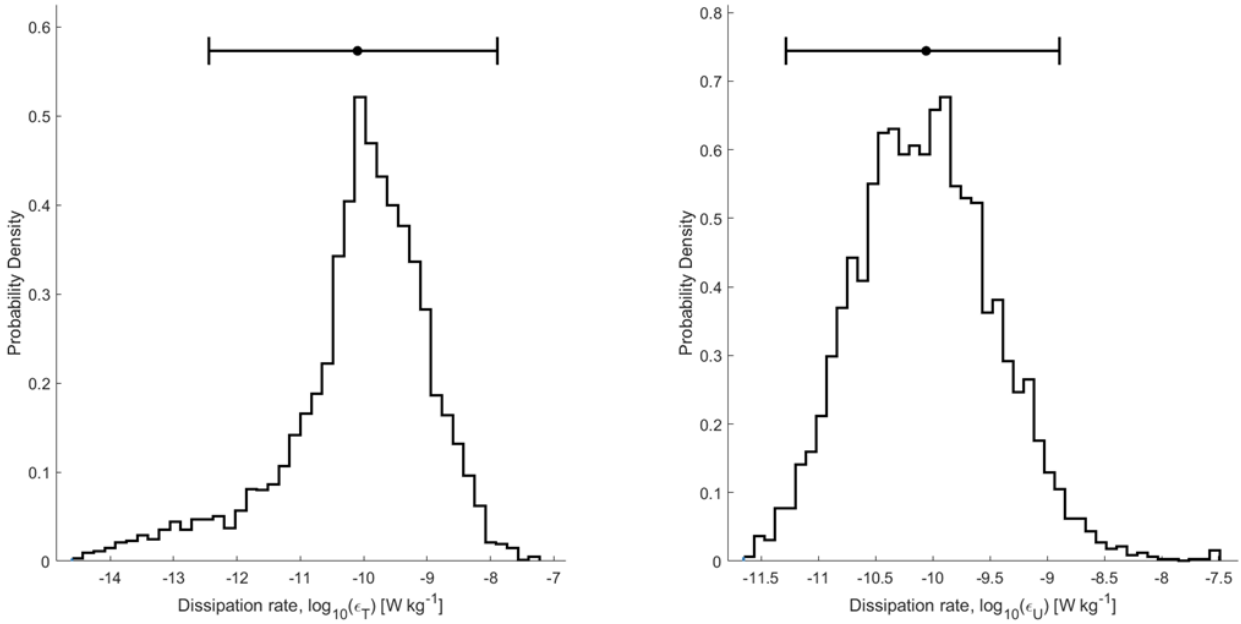

Figure 2.8. Histograms showing the distributions of the microstructure temperature ε_T (left panel) and shear ε_U (right panel) derived TKE dissipation rates. Dots and error bars indicate means and bootstrap confidence level of 95%, respectively, computed from $\log_{10}$ values of all ε data as data exhibit a lognormal distribution in stratified ocean (Baker and Gibson, 1987).

The ε values derived from microstructure temperature observations allow to resolve a wider range than those derived from velocity shear microstructure (Fig. 2.8), mainly because the temperature gradient based computations allow estimation to lower ε values (Scheifele et al., 2018). This appears to be consistent with results from a recent study using microstructure observations in a low energy region in the southeastern Beaufort Sea. That study showed that temperature microstructure data allowed estimation of ε to two orders of magnitude below those based on microstructure shear (Scheifele et al., 2018). Spectral analysis of our data showed that the theoretical Batchelor form conformed to ε values down to O (10^{-12} W/kg, Fig. 2.9), similarly to the results reported by Scheifele et al. (2018). Values lower than O (10^{-12} W/kg) were found to be below the spectral noise level of the temperature sensors. Such measurements are best suited for low energetic environments such as we observed in the eddy core in the Gulf of Mexico and allow expanding the range of observations of mixing intensities. This might be important for numerical ocean models as it provides a more precise estimation of dissipation rates in low energetic environments.

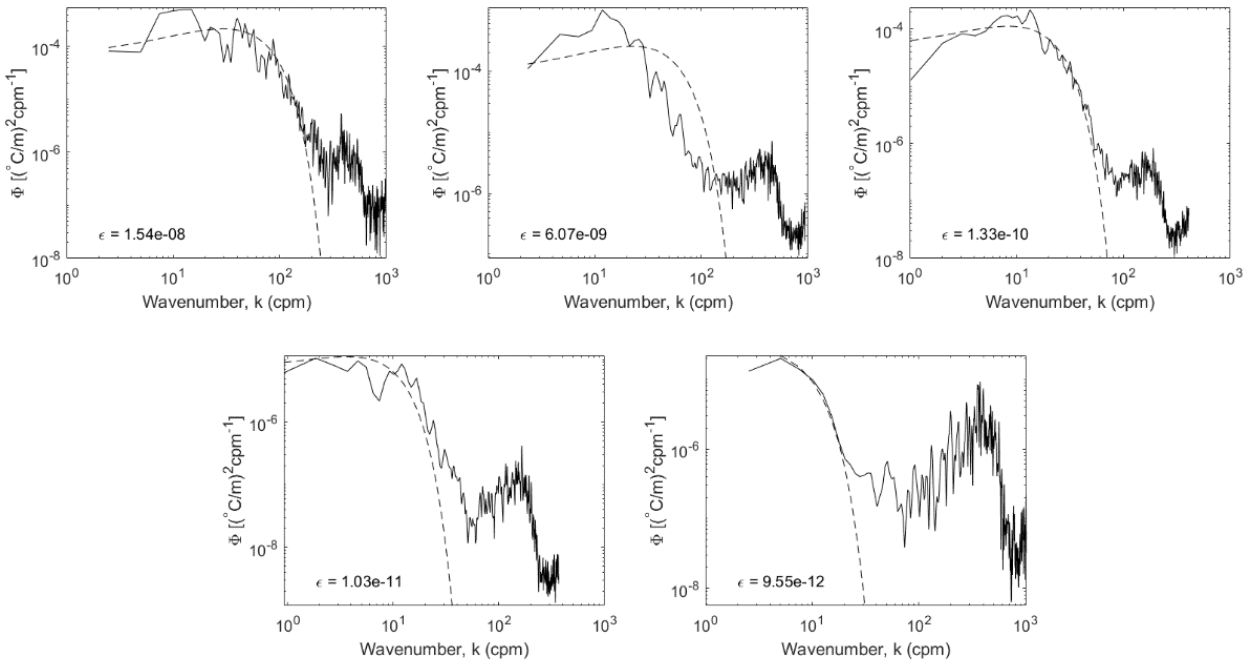

Figure 2.9. Sample of individual temperature microstructure spectra for ε values ranging from ~10^{-8} and down to ~10^{-12} W/kg.

The histograms of microstructure shear and temperature ε values show the notable difference in the distribution of these parameters (Fig. 2.8). The distributions of $\log_{10}$ (ε_U) shear based estimates appear to be slightly positively skewed (s ~ 0.34), while temperature-based estimates are slightly negatively skewed (s ~ -1). As was found by Scheifele et al. (2018), the temperature based estimates appear to span a larger range of values, allowing to expand the lower range down to 10^{-12} W/kg, as Batchelor form of the spectrum can be observed at such low values of TKE dissipation rate (Fig. 2.9; Scheifele et al., 2018). It appears that microstructure temperature observations are likely better suited than shear-based observations for studies of low energy, quiescent regions, such as we observed during this study. To check the quality of data, we compared upward to downward profiles averaged for the deployment (Fig. 2.10). Upcasts and

downcast exhibit only very small differences for both shear and temperature microstructure derived ε values.

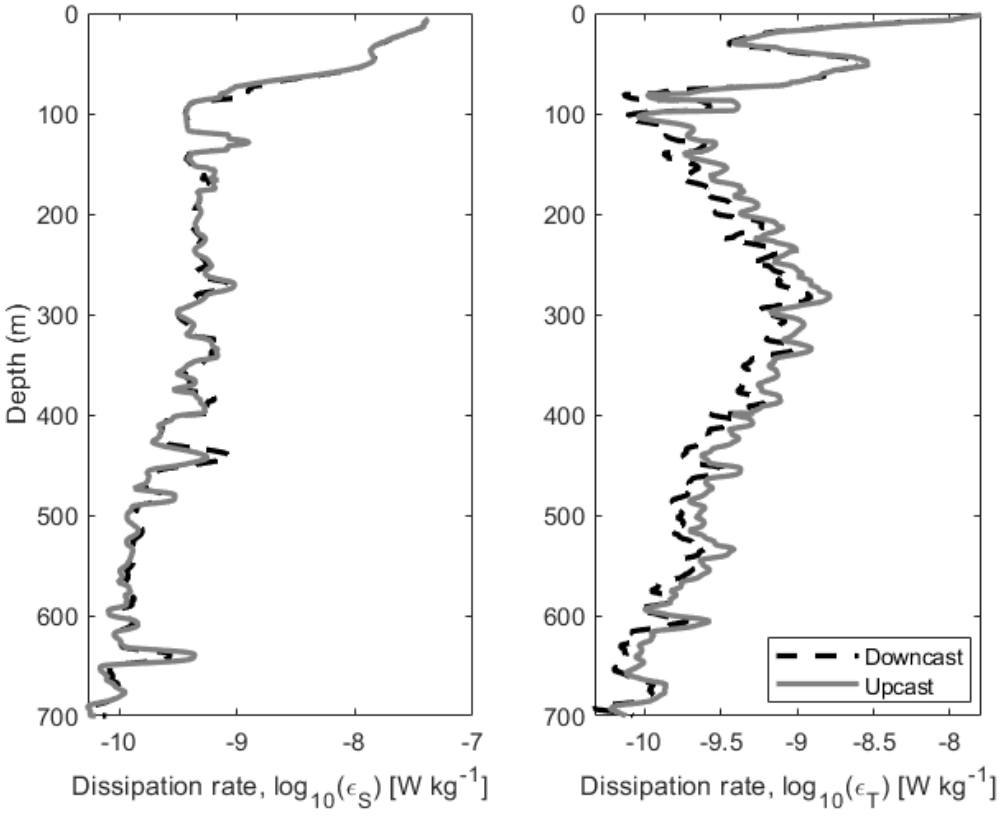

Figure 2.10. Overview of upward (solid line) and downward (dashed line) average vertical profiles of TKE dissipation rates estimated from microstructure velocity shear, ε_U (left panel) and temperature gradient, ε_T (right panel).

2.4 *Conclusions*

Here we demonstrated the mixing properties within LCE in the GOM, which, to the best of our knowledge, are the first glider-based microstructure observations in a large anticyclonic eddy (with a radius of ~100km). Well-defined regions with different mixing levels, deduced from observed TKE dissipation rates, were identified in the LCE. In general, regions with higher

TKE dissipation rates were confined throughout the glider mission in the ML. Below, the ML turbulence is low within the first 100 km of the glider mission in the eddy core at 70-200 m depth. Mixing becomes stronger in the eddy border within 100-150km of glider mission, at 70-200 m depth. Also, we observed higher mixing rates below eddy core at 200-400 m depth. (Fig. 2.4). The SUW patch underneath the eddy core created salinity anomalies, which allowed the development of double diffusion favorable conditions. While Meunier et al. (2019) showed that the layering, which occurs on the sides of SUW patch, is due to mesoscale azimuthal perturbations and not due to double diffusion, the latter process is likely to appear after the layers develop, as they create double diffusion favorable conditions, evident from this study. Salt finger regime was observed below the eddy core while thermohaline intrusions were found on the side of the eddy. Heat and salt fluxes beneath eddy and on the sides of the eddy showed its decay time of about 1.5 years. The data presented can be used to improve/validate numerical simulations of the GOM system, in particular dynamics associated with LCEs, which would benefit model skills to predict hypoxia events, and transport paths of oil, chemicals, and nutrients. Future glider missions at different stages of the eddy lifespan will be required for improvement of our understanding of mixing dynamics and eventual decay of LCEs.

ENHANCED MIXING ALONG THE CONTINENTAL SLOPE IN THE WESTERN GULF OF MEXICO OBSERVED BY MICROSTRUCTURE GLIDER MEASUREMENTS

3.1 *Introduction*

Deep GOM dynamics and circulation pathways are presently not well understood. The deep gulf is filled with upper North Atlantic Deep Water (NADW) entering through the Yucatan straight, ventilating the deep GOM with an average residence time of ~100 years (Ochoa et al., 2021; Amon et al., in preparation). This water mass then leaves the deep gulf through the Yucatan straight as Florida straight is too shallow. The pathways and mechanisms of the outflow from the deep GOM are still not clear. Ochoa et al. (2021) and Amon et al. (in preparation) suggested that the ventilation of the deep GOM is achieved by the transformation of the deep waters into intermediate and thus forming an outflow on top of the incoming NADW, which occupies the deep GOM. Ochoa et al. (2021) discussed that the constant inflow of deep waters through the Yucatan channel should be compensated by upwelling within the deep gulf. Using the canonical Munk's model (Munk 1966), the deep waters can be transformed to intermediate water through mixing induced upwelling. However, the mixing and associated upwelling wouldn't have a uniform distribution within the GOM (Ochoa et al., 2021).

Internal waves are a widespread and important phenomenon in the World Ocean. They are responsible for the generation of vertical mixing through their breaking over rough bathymetry (Ivey and Nokes,1989). Internal wave reflection and dissipation depends on the angle (c) at which the incident waves approach the continental slope and the angle of the continental slope inclination relative to a horizontal plane (γ). The ratio γ/c determines the reflection of internal wave: $\gamma/c<1$ creates subcritical conditions leading to the reflection of the wave upslope; $\gamma/c\sim=1$ leads to the critical conditions with intense wave breaking; and $\gamma/c>1$ results in

supercritical conditions with offshore wave reflection (Thorpe and Haines,1987; Lamb, 2014; Reiche et al., 2018). Reiche et al. (2018) identified that γ values $>1^0$ create critical and supercritical conditions for the incoming internal waves and tides. Many studies investigated the behavior of internal wave interaction with topography using in-situ measurements (e.g., Ivey and Nokes, R. I. 1989; Polzin et al., 1997; Toole et al., 1997; Eriksen, 1998); remote sensing data (Apel et al., 1975; Lavrova and Mityagina, 2017); seismic images (Holbrook and Fer, 2005); laboratory studies (Mowbray and Rarity, 1967; McEwan, 1983); and modeling studies (Willmott and Edwards, 1987; Grimshaw et al., 2007; Klymak et al., 2012).

Moreover, the breaking of internal waves has a direct impact on global ocean circulation (Whalen et al., 2020) as it generates upwelling, which compensates for deep water formation in the Global Ocean. Nikurashin and Ferrari (2013) showed that the internal wave-induced mixing can account for about 20 to 30 Sv of water upwelling, thus affecting the global ocean circulation. Usually, the abyssal ocean is characterized as a quiescent place in terms of turbulence generation. However, elevated mixing spots have been found along regions with rough bathymetry (e.g., Polzin et al., 1997, Toole et al., 1997). We hypothesize that one of such regions suitable for generation of turbulence, due to breaking of internal tides, followed by water transformation, is the western GOM, where the continental slope is the steepest (where depths drop from 0.3 to 3.3 km over 100-150 km distance).

To date, most of the research related to the circulation and mixing in GOM has been based on modeling, remote sensing, or drifter studies and was related to the investigation of surface dynamics of the GOM. For instance, oil spill dynamics were studied using global satellite altimetry assimilated into a model (Olascoaga and Haller, 2012); horizontal surface mixing in the western GOM was analyzed using drifter data analysis (Sansón et al., 2017); surface altimetry

studies targeted the mesoscale surface GOM dynamics (Olascoaga et al., 2013). Pérez-Brunius et al. (2017) used deep water floats together with mooring data to investigate the main circulation patterns in GOM. Authors found that there is persistent evidence for a cyclonic deep boundary current presence in the GOM (Pérez-Brunius et al., 2017). Although these and similar studies have focused on the dynamics and circulation of the GOM, the pathways for deep ventilation remain poorly understood.

As part of the Gulf of Mexico Research Consortium experiment (in Spanish Consorcio de Investigación del Golfo de México, CIGoM), we have conducted ocean glider missions focusing on mixing processes the western GOM. Here, we present an analysis of observations collected during a glider mission along the steepest part of the continental slope in the western GOM during fall 2017. To the best of our knowledge, this is the first time that microstructure data was collected near the western GOM slope. Dynamical processes associated with the bathymetry were observed, and enhanced mixing along the continental slope was detected.

Ocean gliders have been a reliable tool for oceanographic data acquisition (Rudnick et al., 2004). They are particularly well suited for microstructure measurements due to the stable and low-noise characteristics of gliders. Fer et al. (2014) compared glider-based microstructure observations to those from shipboard deployed profilers in the Faroe Bank Channel and showed that the glider and profiler observations agreed within a factor of 2. Other glider microstructure missions confirmed the value of such datasets for ocean mixing research (Palmer et al., 2015; Scheifele et al., 2018; Molodtsov et al., 2020). In addition to glider data, we used Thorpe length scales (L_T; see details next) estimated from CTD casts from two cruises in the GOM to infer the mixing intensity in depths larger than the glider's depth range of 1000 m.

3.2 *Data and Methods*

3.2.1 *Data collection*

Our glider was deployed on November 6, 2017, beginning the mission at 15:51 UTC at 25 26.445 N, 95 39.080 W (Fig. 3.1). Deployment was done from the R/V Pelican's inflatable after the routine deck and water test procedure (~2.5 hours). It was completed successfully at 16:00 UTC after the R/V Pelican received the "all clear" to leave the area and resume regular cruise operations. The target of the deployment was an area of the steepest continental slope in the GOM, where we expected to observe higher mixing rates resulting from possible internal wave breaking (Polzin et al., 1997).

The glider started its mission inside a cyclonic eddy and further aimed to navigate across the steepest part of the continental slope in the Western GOM (Fig. 3.1). Overall, the glider covered a distance of about 90 km during this mission. The glider initially was commanded to escape the strong eddy currents and was moving southwards. After crossing the eddy wall, it started the transect across the steep part of the continental slope. It covered a 60 km transect across the continental slope with depth varying from ~1980m to 680m at the start and end of the transect, respectively. Our Slocum G2 glider – unit 199 (nickname "Dora") was equipped with the MicroRider turbulence package (https://rocklandscientific.com/products/modular-systems/microrider/), which contained two microstructure shear sensors and one FP07 thermistor, payload CTD

3.2.2 *Microstructure shear based measurements*

MicroRider shear probes allow observations of micro scale velocity shear which in turn allow calculation of turbulent kinetic energy (TKE) dissipation rates, ε, by integrating the wavenumber (k) spectrum (ϕ):

$$\varepsilon = 7.5\nu \int_{k_l}^{k_u} \Phi(k)dk \quad (3.1)$$

where ν is the kinematic viscosity, k_l and k_u are the lower and upper integration limits, respectively, estimated using a Nasmyth empirical spectral model (Nasmyth, 1970; Lueck, 2013).

Data processing such as deconvolution of the data, removal of the part of shear spectrum coherent with the accelerometer signal, and despiking was done using the standard MATLAB ODAS package (https://rocklandscientific.com/support/introducing-odas-matlab-library-4-0/). In addition to the ODAS package, we used the flight model suggested by Merckelbach et al. (2019) to calculate the angle of attack and the glider's velocity. Also, we used the Maximum Likelihood Estimate (MLE) method (Ruddick et al., 2000) to fit the power spectral density of the observed microstructure shear spectrum to the Nasmyth form.

3.2.3 *Microstructure temperature based measurements*

MicroRider FP07 fast-response thermistors provide estimations of the temperature variance dissipation rate, χ_T. The advantage of this method is that it is not related to the velocity measurements and thus is much less affected by signal contamination from glider motion or movement of mechanical parts inside the glider. χ_T is defined as

$$\chi_T = 6k_T \int_0^\infty S(k)dk = 6k_T \left(\frac{\partial T'}{\partial z}\right)^2 \quad (3.2)$$

where $S(k)$ is the spectrum of the vertical gradient of temperature fluctuations, $\frac{\partial T\prime}{\partial z}$, and k_T is the molecular thermal diffusivity. A theoretical form for the power spectra of temperature gradients was first suggested by Batchelor (1959):

$$S_B(k;k_B;\chi_T)=\left(\frac{q}{2}\right)^{1/2}\frac{\chi_T f(a)}{k_B k} \quad (3.3)$$

where $f(a)=a(e^{\frac{a^2}{2}}-a\int_a^{\infty} e^{-x/2}dx)$ and $a=kk_B^{-1}\sqrt{2q}$, where q is a universal constant and has a range of 3.7±1.5 (Oakey, 1982), and k_B is the Batchelor cutoff wavenumber. Fitting observed spectrum to the Batchelor form via adjustment of the Batchelor cutoff wavenumber can thus provide an estimate of ε:

$$\varepsilon = k_B^4\, \nu\, {k_T}^2 \quad (3.4)$$

The MLE method (Ruddick et al., 2000) was applied to the microstructure temperature data to fit observed power spectra to theoretical Batchelor form to estimate k_B and thus ε. In order to get a reliable ε estimate, we followed the selection process described in Ruddick et al. (2000) and first calculated the signal-to-noise ratio (SNR) between the average spectral variance and variance of the noise spectrum. We required SNR to be greater than 1.3 value. Another criterion that was used to select data was the mean absolute deviation (MAD). MAD between the theoretical and observational spectra should be greater than $2\sqrt{2/\mathrm{d}}$ (Ruddick et al., 2000) for data in order to pass the quality control. The third criterion which was used is likelihood ratio which is defined as

a ratio of MLE power law fit and MLE theoretical spectrum fit. We required $\log_{10}$(LR) to be greater than 2 in order for data to pass quality control.

3.2.4 *Thorpe scale parametrization*

In addition to glider data, we used CTD profiles from 2016 and 2017 GOM cruises, which covered the same area of the continental slope in the western GOM. We used Thorpe scale (L_T; Thorpe 1997) parameterization to calculate TKE dissipations rates. L_T values were calculated using ship-based CTD temperature data together with MATLAB toolbox (Gargett & Garner, 2008). The Thorpe displacements are estimated by finding the vertical displacement of the measured density/temperature from the prescribed value, which is found by sorting the observational data profile from top to bottom with the densest waters at the bottom. L_T values were used as a complementary source, independent from the MicroRider, to estimate mixing along the continental slope as well as beneath the glider's depth limit of 1000m. L_T is associated with turbulent overturns which disturb the vertical profiles of, e.g., temperature/density and are related to the TKE dissipation rate, ε through:

$$\varepsilon_{Thorpe} = 0.2^* L_T^2 {}^* N^3 \qquad (3.5)$$

where N is buoyancy frequency ($N^2 = -(g/\rho)\partial\rho/\partial z$, where ρ is the potential density)

To provide better spatial coverage, we used data from a 2016 cruise in addition to the 2017 cruise CTD (Fig. 3.1).

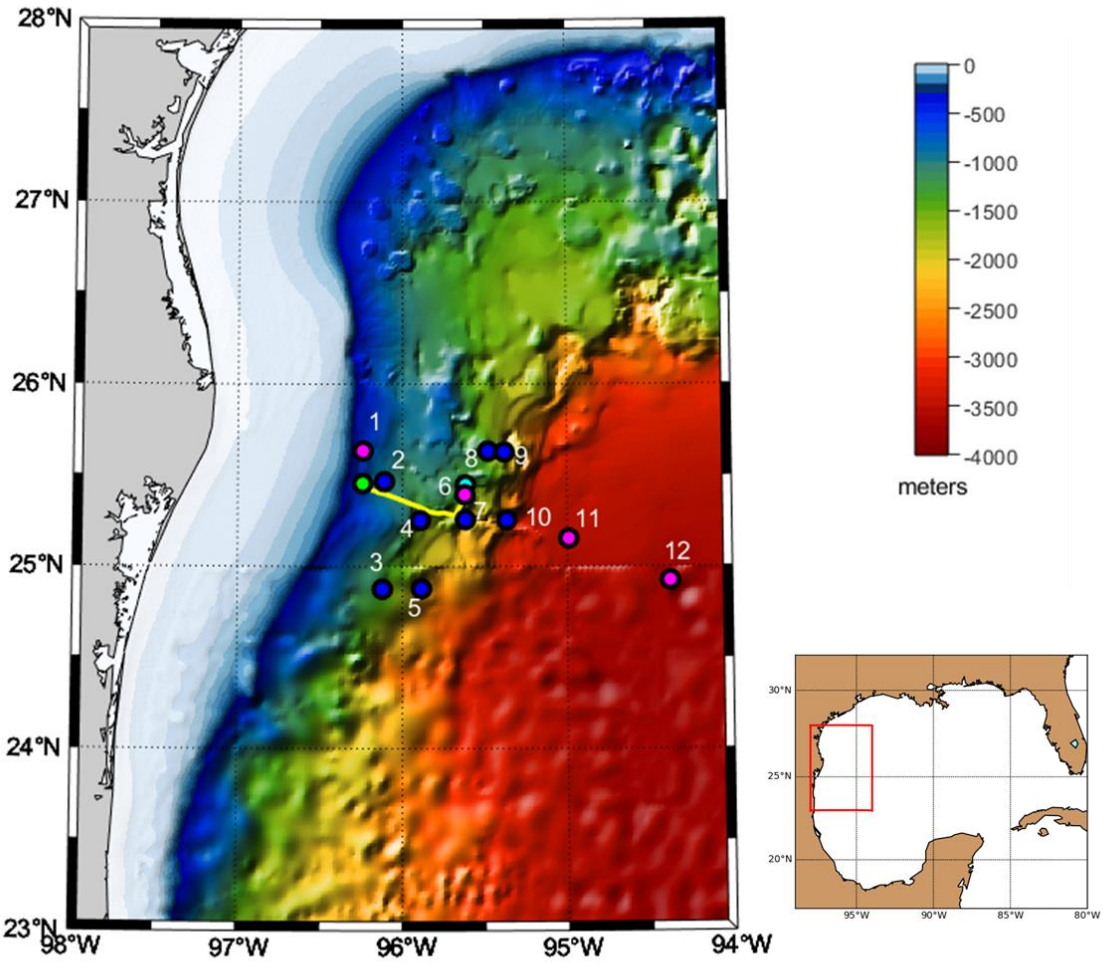

Figure 3.1. Map of the glider mission route (yellow line), deployment (cyan), and recovery (green dot) locations. CTD stations are numbered by proximity to the shore (with numbering increasing with offshore distance); 2016 cruise stations are shown as dark blue dots; 2017 stations are shown as magenta dots. Map was created using Pawlowicz (2020) matlab toolbox.

3.3 *Results*

The temperature, salinity, and density fields from the glider (Fig.3.2) show relatively strong stratification (N^2 up to 0.04 s^{-2}, Fig.3.3a) along the glider path (Fig.3.1). Freshwater runoff (related to heavy precipitation events) from the continent resulted in a patch of lower salinity in the near-surface layer (0-10 m depths) (Fig. 3.2b). Beneath the relatively fresh water, we can observe relatively homogeneous mixed layer (ML) in both the density and temperature fields and is ~20-80m deep, while beneath the thermocline (~80-180 m), with a pronounced density gradient (N^2 ~ 0.02-0.04 s^{-2}, Fig.3.3a), the ocean interior exhibited a homogeneous density structure (~ below 180m, Fig. 3.2c). Also, we can note a salinity maximum located at ~120m depth.

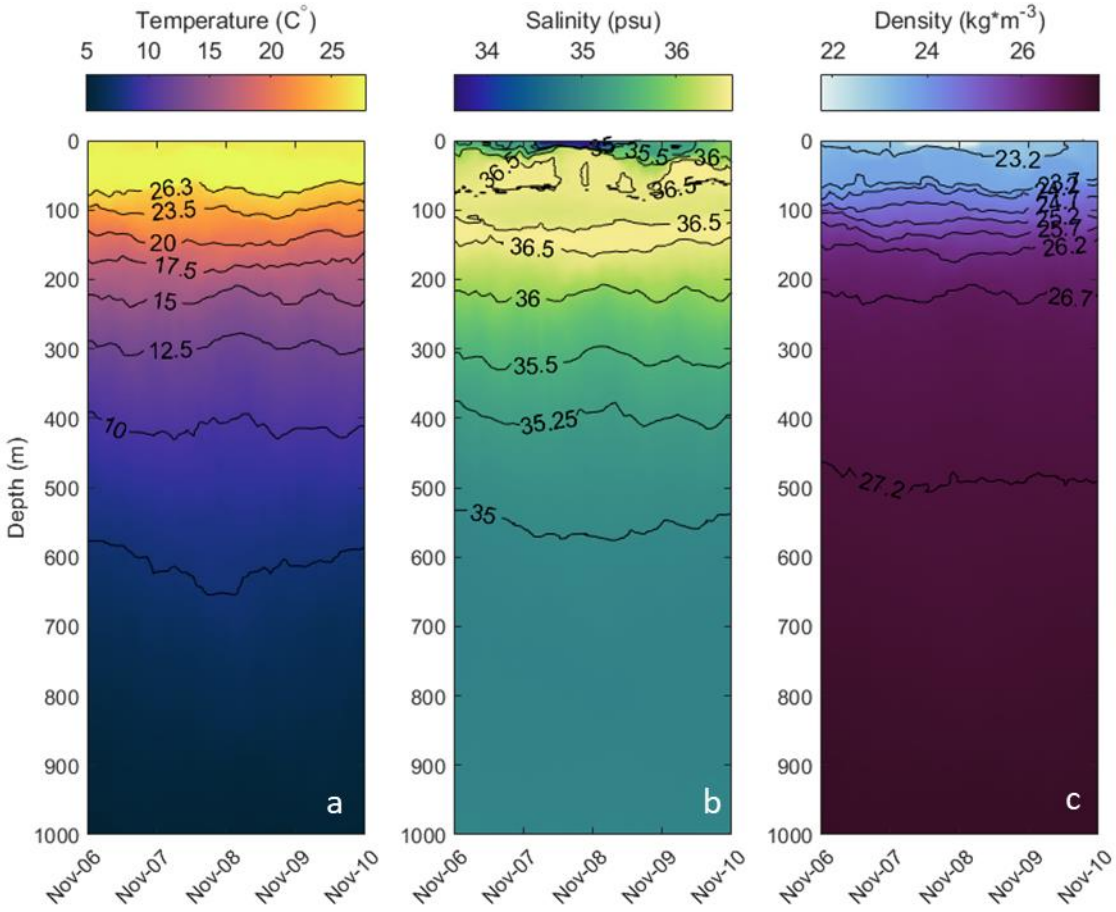

Figure 3.2. Glider's CTD profiles of temperature (a), salinity (b), and density (c). The beginning of deployment coincides with CTD station #6 (Fig. 3.1).

Besides higher ε values within the surface ML, the ε pattern showed elevated values in the ocean interior (Fig. 3.3b,c), as might be expected from internal wave breaking over continental slopes (Polzin et al., 1997). Near-bottom values of ε reached 10^{-8} W/kg, much higher than commonly observed deep ocean values of $\leq 10^{-10}$ W/kg (e.g., Molodtsov et al., 2020). This translates into higher values of eddy diffusivities (Fig. 3d). The observed diffusivity values reach up to 10^{-4} m^2/s along the continental slope.

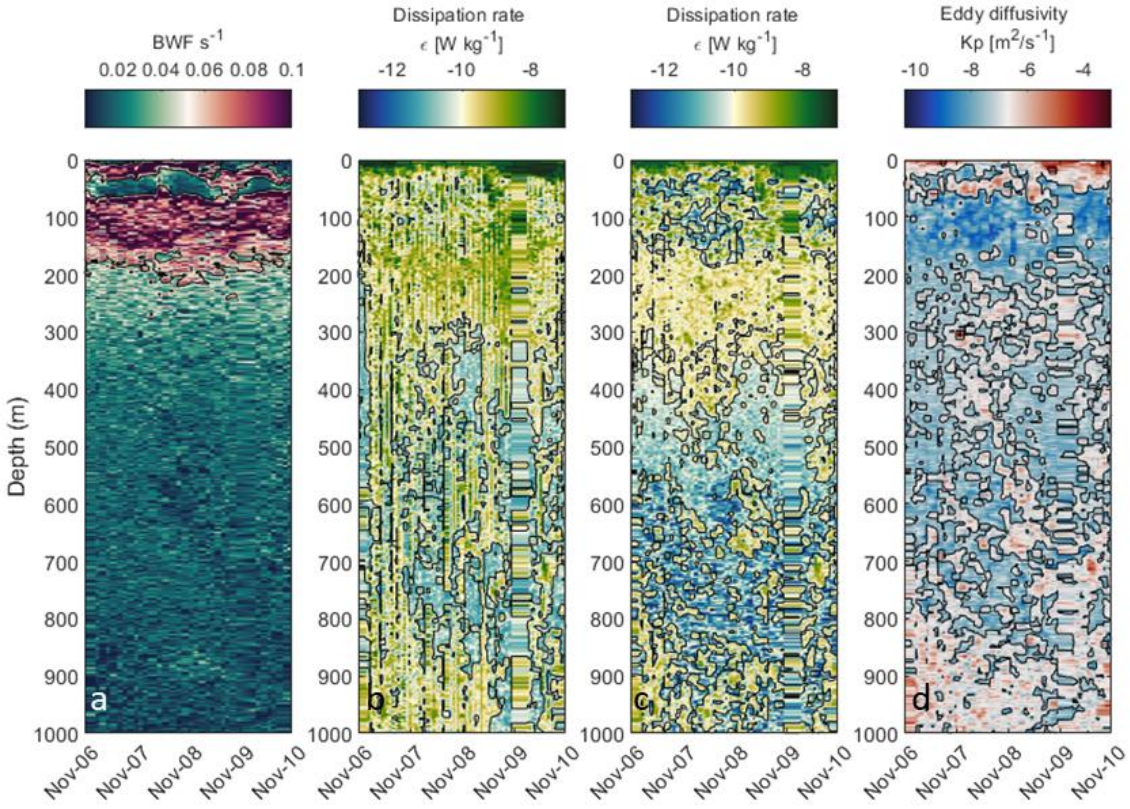

Figure 3.3. Buoyancy frequency, *N* (a; contours represent 0.05 isoline); Turbulent kinetic energy dissipation rate, ε, profiles estimated from microstructure velocity vertical shear (b), and from microstructure temperature vertical gradient (c; contours represent 10^{-10} isolines); and eddy diffusivities (d; contours represent 10^{-7} isolines). The beginning of deployment coincides with CTD station #6 (Fig. 3.1).

The difference in mixing intensity in deep parts of glider observations is also noticeable when we compare the continental shelf 2017 glider deployment data with the deep GOM deployment from 2016 (section 2.2; Fig. 3.4). The histograms clearly show the higher amount of

mixing in the 2017 deployment, with an overall distribution of values covering a larger range in comparison to the 2016 histogram shape.

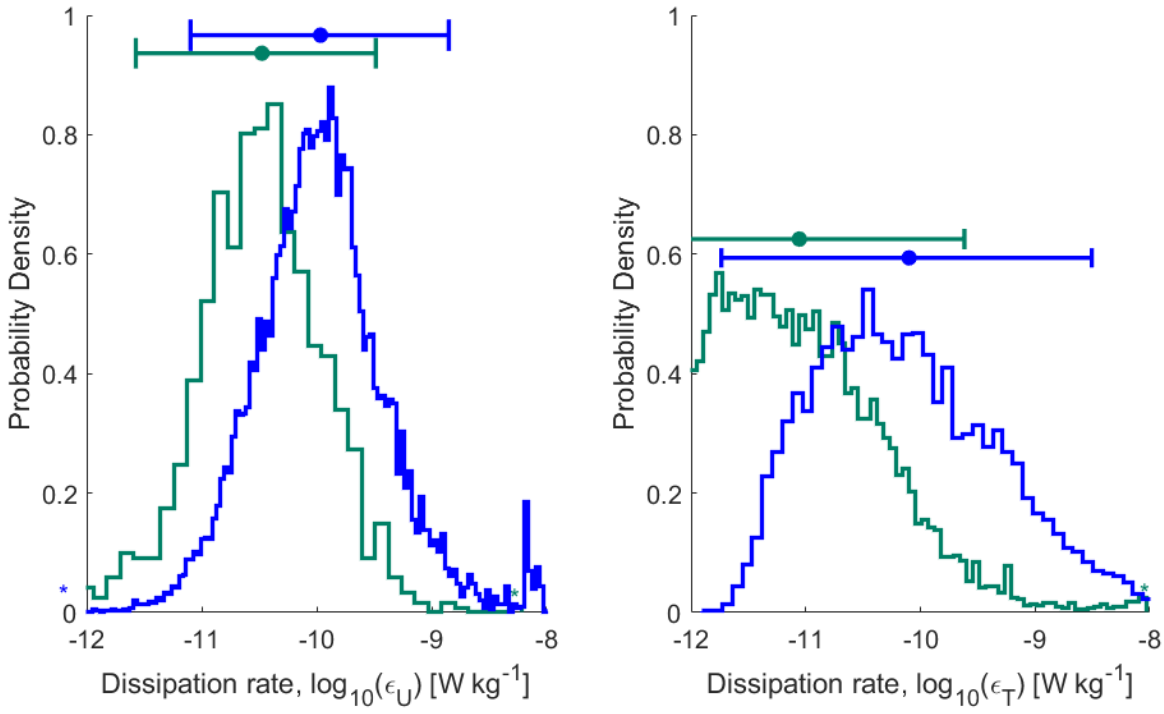

Figure 3.4. Histograms representing the microstructure velocity shear (left panel) and microstructure temperature (right panel) based $\log_{10}$ values of ε between 650 and 1000 m for 2016 (green line, 1039 data points) and 2017 (blue line, 12536 data points). Dots and error bars indicate the means and 95% bootstrap confidence levels, respectively.

It is important to note that microstructure temperature-based ε values on both histograms (Fig. 3.4) span a wider range of values than shear-based estimates. It was found that the microstructure temperature based observations allow estimation of lower ε values (down to O(10^{-12} W/kg)) compared to estimates based on microstructure shear (down to O (10^{-11} W/kg)), mainly because the temperature gradient spectra can be resolved at such low ε levels (Scheifele

et al., 2018). Thus, the values below 10^{-11} W/kg and 10^{-12} W/kg are below the instrument noise levels for shear and temperature microstructure observations, respectively, and should not be taken into account.

We used Thorpe length scale analysis applied to CTD data to infer "hot spots" of mixing within the water column along the continental slope (Fig. 3.5). Thorpe scales identify the region of relatively large temperature disturbances along the bottom of the continental slope down to a depth of more than 2000m. Below this level, the GOM stays relatively quiescent with a homogeneous water mass (~27.7 kg/m3), which represent the NADW (Portela et al., 2018). Also, the results from L_T parametrization were able to capture the pattern of mixing, which was observed using microstructure data (Fig. 3.3) – elevated mixing up to 10^{-7} W/kg in the mixed layer and the relatively quiescent region below with values ~10^{-10} W/kg, till the measurements start to approach the bottom where the mixing intensifies again.

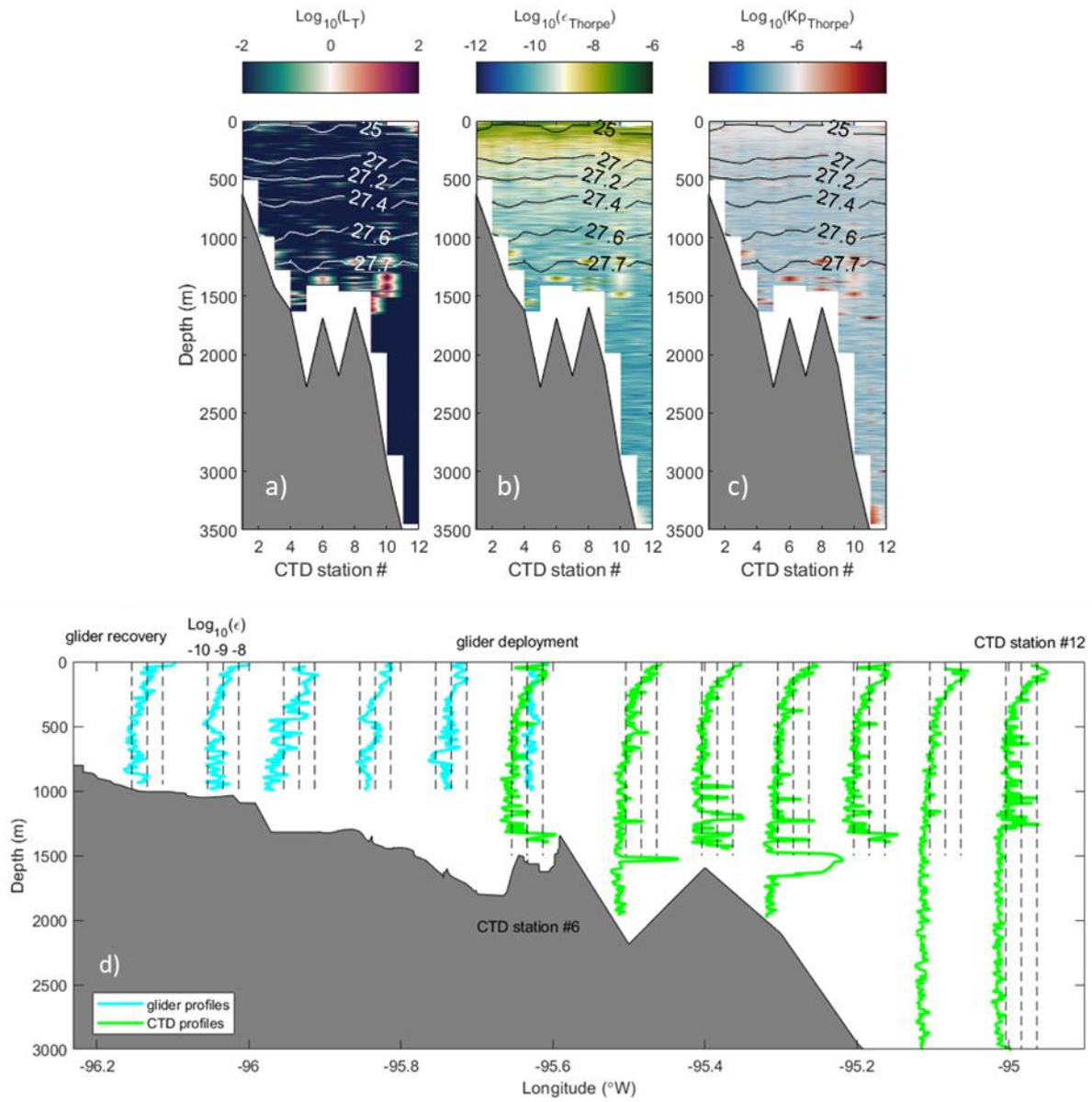

Figure 3.5. a) Log values of Thorpe displacements $\log_{10}(L_T)$ computed using shipborne CTD data from GOM cruises in 2016 and 2017; b) Log values of dissipation rates $\log_{10}(\varepsilon_{Thorpe})$; c) Log values of eddy diffusivities $\log_{10}(Kp_{Thorpe})$; x axis represent the CTD stations number; contours represent isopycnals; d) averaged glider profiles of $\log_{10}(\varepsilon_U)$for each 0.1^0 longitude (blue) and $\log_{10}(\varepsilon_{Thorpe})$ profiles from CTD stations 6-12.

Individual profiles of ε calculations using microstructure data were compared to the profile of ε estimates based on Thorpe scale (Fig. 3.6). CTD-based Thorpe scale mixing rates tend to overestimate microstructure-based values in upper layers, but overall estimates resemble a similar pattern in vertical mixing structure. All three profiles show elevated mixing rates in the mixed layer, with ε values up to 10^{-7} W/kg and a less turbulent region below with ε values spanning the range 10^{-10} to 10^{-8} W/kg.

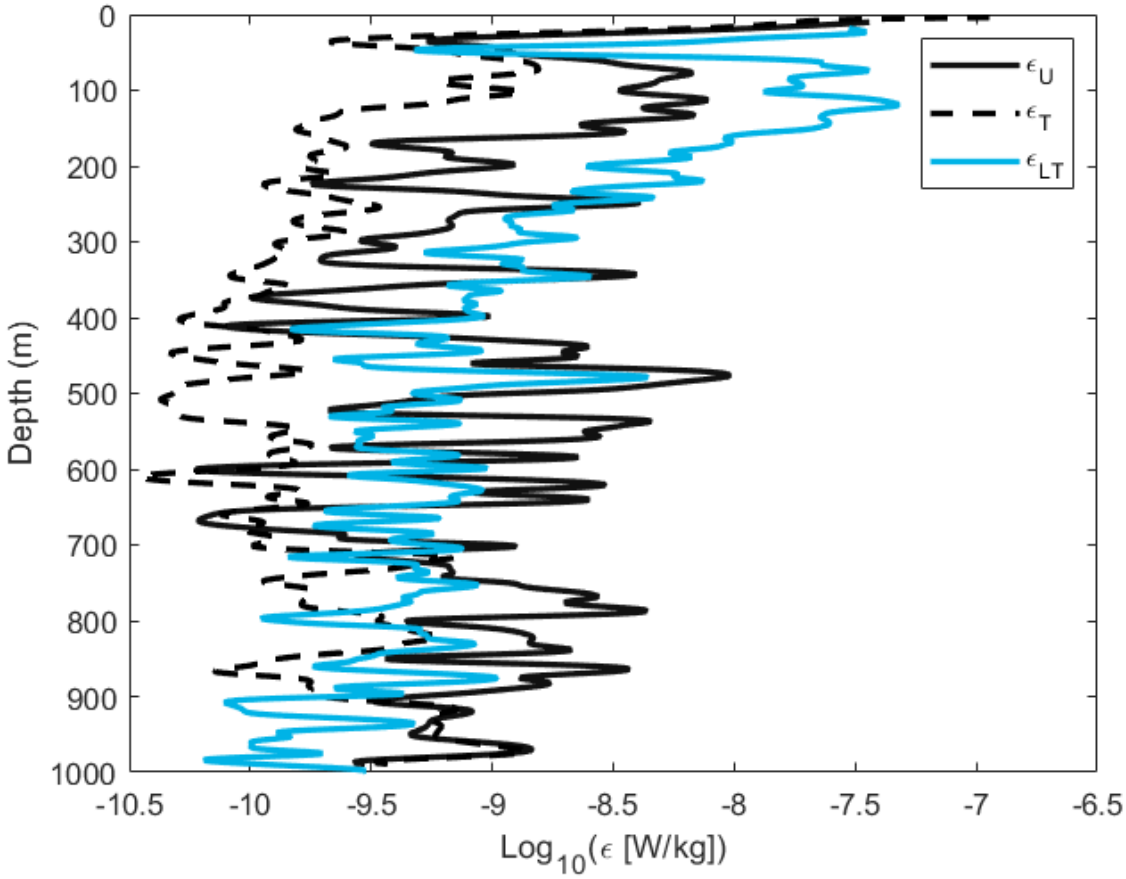

Figure 3.6 Profiles of $\log_{10}(\varepsilon)$ values computed using glider microstructure velocity (black dashed line), microstructure temperature (black line) and Thorpe scale (L_T, blue line; stations 6 (Fig.3.1)).

3.4 *Discussion*

The deepest water mass which can flow into GOM through the Yucatan channel (with the sill depth of ~2040m) is NADW (with a density below 27.7 kg/m^3, Portela et al., 2018). After entering the GOM, this water sinks and fills up the deep GOM (below ~1500m). Previous studies showed that the residence time of deep GOM waters is of the order of 100 years (Ochoa et al., 2021; Amon et al., in preparation). Ochoa et al. (2021) suggested that in order to ventilate deep GOM, there should be the generation of upwelling velocities of O(1cm/day), which using Munk's model (Munk 1966), implies levels of *Kp* values of ~10^{-4} m^2/s (Ochoa et al., 2021).

The upwelling velocities could be estimated if the vertical scale or *Kp/ w* ratio is known, where *Kp* is the vertical eddy diffusivity, and *w* is vertical velocity. We take the vertical scale of 700m calculated by Ochoa et al. (2021) and different values of *Kp,* form O(10^{-4} m^2/s) to a maximum observed value (Fig.3.5c) of O(10^{-3} m^2/s) to estimate the upwelling velocities (Table 3.1). We also consider different inflow rates through the Yucatan channel provided by Candella et al., 2019 and as discussed in Ochoa et al. (2021). Finally, we estimated the area needed for such upwelling to take place to compensate for the inflow through the Yucatan. This estimate can be compared to the total area of a region where the bottom slope exceeded 1^0 (Figure 3.7). The calculated area of a relatively steep slope and the inflow of 0.1 Sv will require the upwelling velocities to be around 6 cm/day and result in a total area of upwelling of $1.4*10^5$ km^2. We find that the maximum values of observed *Kp* would result in 12 cm/day velocities, which will require an overall upwelling area of ~10^5 km^2 in order to compensate for 0.2 Sv inflow. The 0.2 Sv will result in ~100 years of residence time for the GOM waters below 2000m to be completely refilled when 0.1 Sv will result in 200 years residence time. According to the

previous studies (Ochoa et al., 2021; Amon et al., in preparation), 100-year estimate is more realistic for deep GOM.

Table 3.1 a) Different *Kp* values; b) resulted in upwelling velocities; c) total area required to compensate 0.1 SV inflow through Yucatan to ventilate GOM on a 100yr timescale; d) same as c) but for 0.2 SV inflow through Yucatan.

a) *Kp* (m^2/s)	**b)** *w* (cm/day)	**c)** Total area (km^2) for 0.1 Sv Yucatan inflow	**d)** Total area (km^2) for 0.2 Sv Yucatan inflow
10^{-3}	12.34	$7*10^4$	$1.4*10^5$
$5*10^{-4}$	6.17	$1.4*10^5$	$2.8*10^5$
10^{-4}	1.2	$7*10^5$	$6.4*10^6$

In this study, we hypothesize that the regions with a steep continental slope in the GOM represent a major pathway for deep water upwelling and transformation to intermediate waters. The observed mixing intensity shows stronger turbulence along the western GOM with a steep continental slope using both direct and indirect mixing observations. We propose that this is a likely region of deep water transformation in the GOM, where the internal tidal waves break and generate conditions for vertical mixing hot spots. This is supported by observations (Fig.3.3, Fig.3.5) and the continental slope values (Fig. 3.7). A slope larger than 10 can become a critical slope for several types of internal waves. I.e., Reiche et al. (2018) found that the slope around 1^0 is critical for the semidiurnal tide, the steeper slope is critical, and supercritical for the internal waves on the Israeli Mediterranean continental slope. Moreover, this region lays in the pathway of a cyclonic boundary current (Molinari and Mayer, 1982; Hamilton 1990; Pérez-Brunius et al., 2018), which might also contribute to the elevated mixing found along the continental slope. Pérez-Brunius et al. (2018) showed that the deep eastern part of GOM is subjected to strong

mixing conditions which can be attributed to the NADW downslope transit to the deep gulf (their Fig. 5a). Besides that the authors detected a hot spot of mixing in western deep GOM in the region of this study (their Fig. 5b).

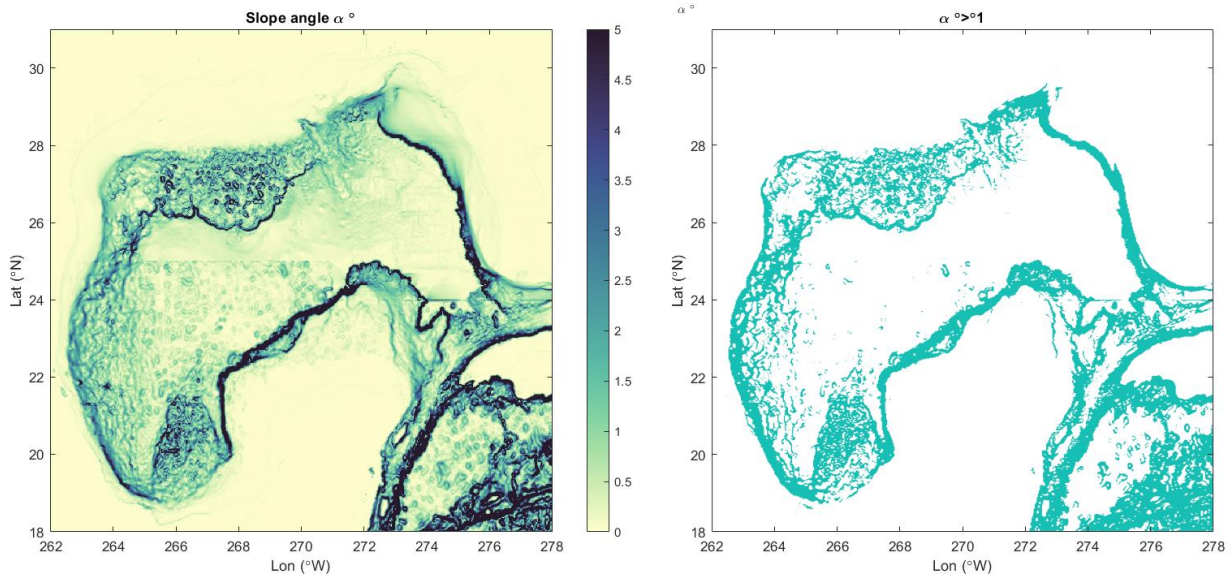

Figure 3.7 Map of slope values (α) in GOM (left panel); regions with α values greater than 1^0 with total area estimated to be $1.3*10^5$ km^2 (right panel).

We propose that regions with elevated mixing intensity, like in the study area, provide a possible conduit for NADW transformation into lighter waters through the upwelling. Then these lighter waters are mixed upward and form the outflow from the GOM, closing the deep ventilation loop in the GOM. We would like to contribute to the conceptual model proposed by Ochoa et al. (2020) and Amon et al. (in preparation). The original spilling model (Ochoa et al., 2021 Fig.7) states that the deep GOM is filled by the NADW entering the Yucatan channel. NADW, after entering Yucatan, sinks along the continental slope of the Yucatan channel, creating highly turbulent downslope transit of waters and homogenizing deep GOM. Then the

authors state that deep waters are upwelled along with other sloping areas of GOM. We add a pathway for deep water upwelling, specifically in regions of the steep continental slope in the GOM (Fig. 3.8). The authors also suggest that the original Munk's model cannot explain the warming trends in the deep GOM as it will produce unrealistic upwelling velocities (Ochoa et al., 2021). However, Munk's model can be used in the explanation of the deep water transformation to lighter waters in GOM through slow upwelling in areas of the interaction of internal waves with continental slope. The Western GOM most likely is, however, not the only possible region with upwelling favorable conditions. Thus, future studies targeting other parts of GOM with steep continental slopes are required to complete the overall understanding of deep GOM circulation.

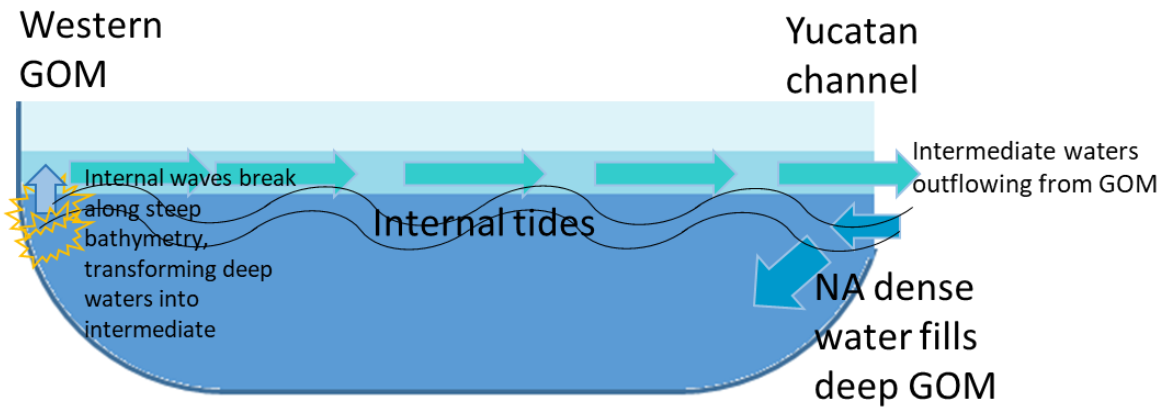

Figure 3.8 Schematic representation of deep circulation in the Gulf of Mexico.

3.5 *Supplementary material*

An example of the power spectral density (PSD) estimates are presented in fig. 3.9 a,b. The shear spectrum and MLE fit to the Nasmyth empirical spectrum, and the MLE fit to the Batchelor spectrum corresponds to ε values spanning a range of 10^{-11} to 10^{-8} W/kg. The MLE-based ε estimates using microstructure temperature data were compared to the values based on the integration of shear spectra, and MLE fit of Nasmyth theoretical spectra to the observations (fig. 3.9c,d, respectively). The results show better agreement between MLE fit of temperature and MLE fit to shear data than between MLE fit of temperature and integration of shear spectrum based estimates.

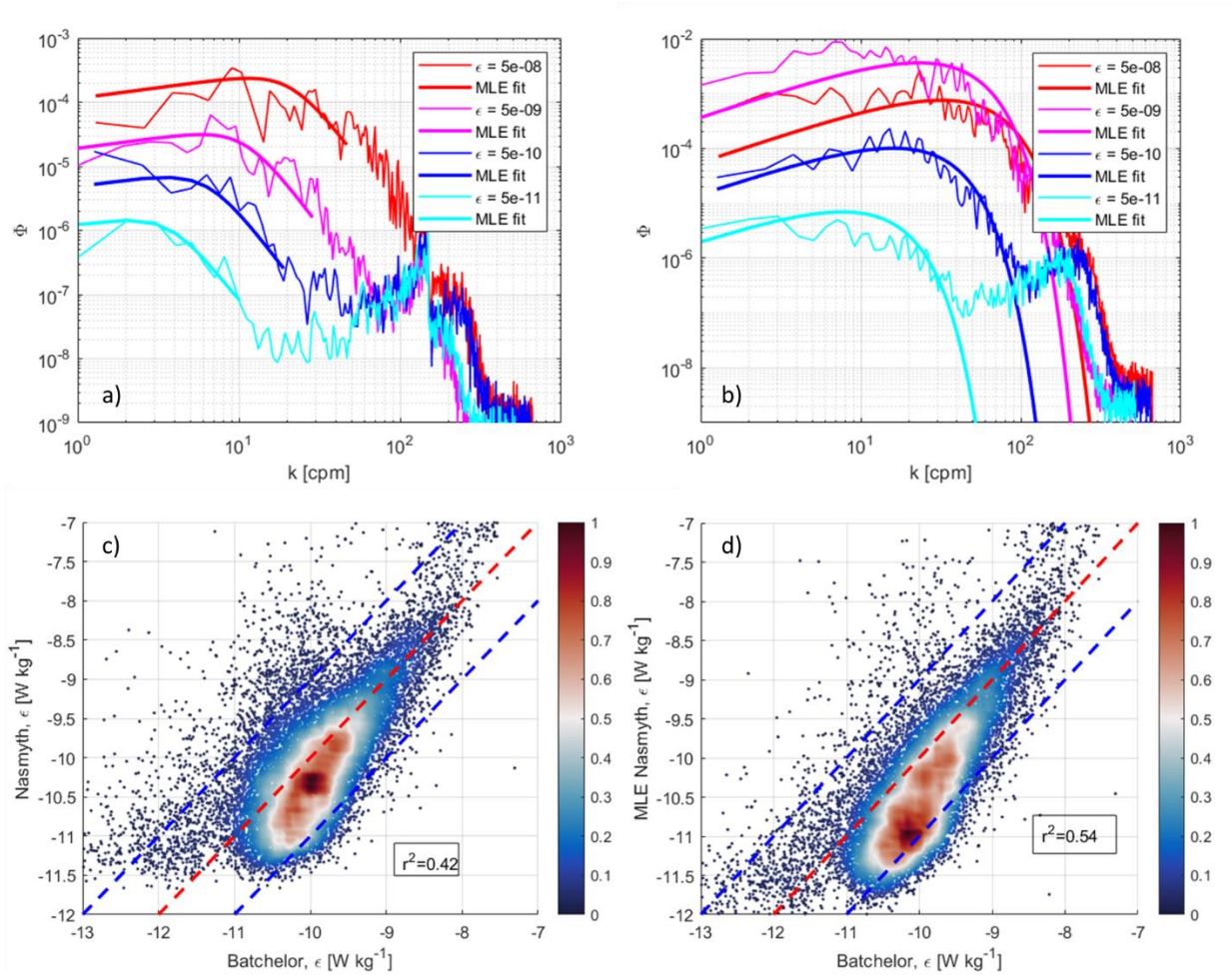

Figure 3.9 a) Example of Nasmyth spectra color-coded for different ε values with the corresponding MLE best fit lines; b) example of Batchelor spectra color-coded for different ε values with corresponding MLE best fit lines; c) comparison of Batchelor MLE fitted ε values to those computed by integration of the PSD of the microstructure velocity shear; d) comparison of Batchelor and Nasmyth MLE fit based ε estimates.

A comparison of the downcast and upcast profiles from microstructure shear and temperature sensors is presented in Fig.3.10. The upcast and downcast profiles coincide well for both shear and temperature microstructure ε estimates.

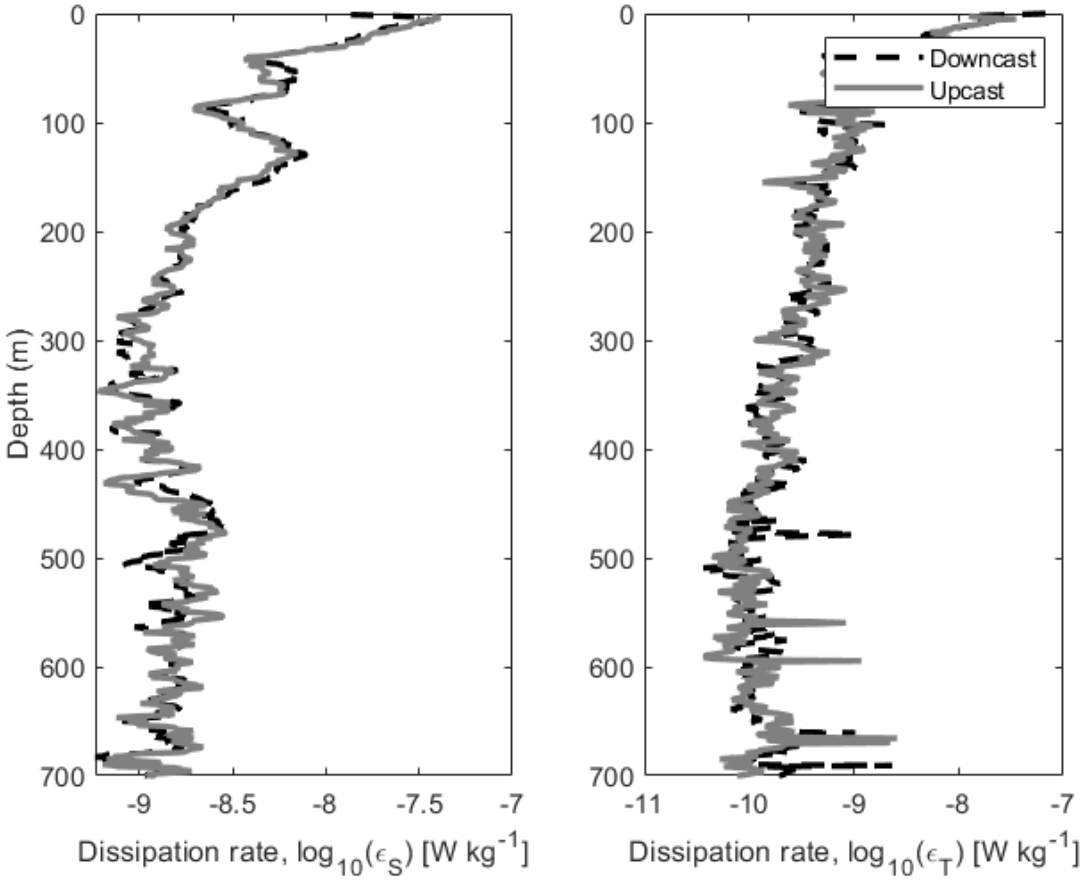

Figure 3.10. Overview of upward (solid line) and downward (dashed line) average vertical profiles of TKE dissipation rates estimated from microstructure velocity shear, ε_U (left panel) and temperature gradient, ε_T (right panel).

4. ESTIMATION OF GAS EXCHANGE COEFFICIENTS FROM OBSERVATIONS FROM THE YENISEI RIVER, RUSSIA

4.1 *Introduction*

Measuring turbulence in high latitude river environments to directly determine the air-water gas exchange coefficients requires new approaches. There is currently no established efficient direct method to determine the gas exchange coefficient in rivers. Current methodology, which was developed for the open ocean using wind speed, appears inadequate, particularly for river environments, where flow dynamics may dominate over wind effects. Moreover, a direct method for determining the gas exchange coefficient would allow a more realistic evaluation of greenhouse gas (GHG) exchanges in boreal aquatic ecosystems. In particular, carbon fluxes that are associated with large Siberian Rivers that drain watersheds representing frozen carbon reservoirs playing a significant role as positive feedback to the rapidly changing high latitude climate.

The problem of intensifying biogeochemical cycles was acknowledged as a global issue in the 20th century. The increase of greenhouse gases (GHG) and their consequences has drawn attention in many research disciplines focused on the carbon cycle. In fact, changes in climate are caused by and are causing perturbations in the global carbon cycle (e.g., IPCC 2014, Stocker et al., 2014).

Russian boreal forests, wetlands, and tundra ecosystems play an important role in the global carbon cycle and represent a large carbon sink of ~692 Tg C yr^{-1} (Dolman et al., 2012), mostly because of CO_2 uptake during photosynthesis in the vast boreal forests which represents about 20 % of the global uptake by terrestrial ecosystems (Keenan et al., 2018). More than half of the Russian territory lies in regions with permafrost soils. Climate-sensitive future changes in

permafrost may cause potentially dramatic shifts in the boreal carbon cycle (McGuire et al., 2009; Schuur et al., 2013; Schuur et al., 2015). Therefore, it is crucial to understand the controls and to quantify the fluxes of all components of the high latitude carbon cycle. Carbon flux studies in this area are mainly focused on the analysis of terrestrial carbon budgets, using methods such as eddy-covariance (Dolman et al., 2012; Laurila et al., 2012), landscape inventory methods (Shvidenko et al., 2010), and atmospheric inversion models (Dargaville et al., 2006). However, there are still many uncertainties remaining as observational data is scarce and modeling approaches are constrained as well (Dargaville et al., 2006; Dolman et al., 2012). The observations from eddy towers are limited (e.g., Dolman et al., 2012), thus upscaling of these data provides generalized results. Other methods such as inverse modeling show quite different outcomes between several studies (e.g., Dargaville et al., 2006), which can be attributed to differences in model setup and different model biases (Dargaville et al., 2006). For this reason, the quantification of carbon cycle stocks and fluxes is still challenging, which leaves many aspects of the boreal carbon system poorly understood.

One such uncertainty is the lack of carbon release estimates from lakes and streams into the atmosphere as part of the lateral ecosystem carbon export from boreal environments to the Arctic Ocean. This can lead to an overestimate of the boreal carbon sink strength by 20% (Kling et al., 1991). There are only a few direct studies addressing the river-driven lateral fluxes of carbon in boreal regions that include GHG exchange between freshwater bodies and the atmosphere due to the complexity of monitoring such processes. Most studies (e.g., Dolman et al., 2012) use river discharge data and low-resolution river concentrations to calculate lateral carbon fluxes and thus do not account for the air-water gas exchange between rivers and the atmosphere. Based on our own observations, dissolved organic carbon (DOC) at the downstream

sampling sites (PARTNERS program) showed signs of extensive bacterial degradation (Kaiser et al. 2017) and lower DOC concentrations (Raymond et al. 2007, Amon et al. 2012) relative to upstream tributaries in Central Siberia, which had high DOC concentrations, particularly during the freshet period (>30 mg/l) and a trend of increasing DOC and lignin phenol concentrations with decreasing stream order in the Yenisei river network (Prokushkin et al. 2008, 2011, unpublished data). Respiration of terrigenous DOC within the rivers is suggested by the observed isotopic shift towards more depleted values found in dissolved inorganic carbon (DIC) during freshet and increasing isotopic depletion further up in the river network (unpublished data). This indicates that without measuring the CO_2 exchange between river and atmosphere, we could miss a significant portion of the lateral carbon transport from these boreal watersheds.

The development of an accurate methodology to estimate air-water gas transfer velocities is a complex task. The original studies were based on lab experiments and field observations (Davies et al., 1964; Ledwell, 1984; Nightingale et al., 2000). The difficulty of collecting in-situ data leads to the poor temporal and spatial coverage of data products and thus incomplete understanding of large-scale processes and variability associated with air-water gas exchange. Thus, Wanninkhof et al. (2014) proposed to use wind speed solely as the base for the parameterization of a gas transfer coefficient. While this approach has been widely used in oceanic environments, it may lead to erroneous results in some cases, specifically in river environments, where air-water gas exchange is likely to be governed by river currents and less by simply the wind. Previous studies have suggested that gas exchange coefficients are driven by turbulence strength in water, which might be produced not only by wind forcing (Kitaigorodskii, 1984; Zappa et al., 2007). Raymond et al. (2012) proposed to use stream hydraulics such as stream slope and velocity in order to parametrize the gas transfer between rivers and the

atmosphere. Still, the authors argue that this approach is best suited for large-scale studies. Esters et al. (2017) was using the small eddy model (SEM, Lamont and Scott, 1970) to approximate gas transfer coefficient (*k)* with water side friction u_* using eddy covariance measurements. However, their approach is dependent on a proportionality coefficient and wave conditions.

In this study, we suggest a simpler parameterization method suitable for river environments. We hypothesize that the air-water gas transfer in rivers with strong currents is regulated mainly by near-surface water turbulence and less so by the winds. In this study, we provide high-resolution estimates of gas exchange coefficients based on a new approach using observational data collected during a ship-based expedition on the Yenisei River and compare the turbulence-based estimates of gas exchange coefficients to the wind-based estimates. We accomplished this by using the ADCP to determine the current velocity and deriving the turbulent kinetic energy dissipation rate, which was then used to derive the friction velocity. Finally, the friction velocity was used in the General Ocean Turbulence Model (GOTM) to calculate a continuous value for the gas exchange coefficient. Based on our field experience, we also make recommendations for the most promising instrumental setup to derive high-resolution estimates for gas exchange coefficients in rivers of different scales.

4.2 *Methodology*

The classical Wanninkhof (2014) approach determines the air-water gas exchange coefficient (*k*) assuming that the wind is the sole forcing factor and is given by the following equation,

$$k = 0.251 * u_{10}^2 * (Sc/660)^{-1/2} \qquad (4.1)$$

where u_{10} is the wind speed at 10 m height, and *Sc* is the Schmidt number of the gas.

However, relative to the open ocean, river environments represent a very different case, and wind might not be the main or sole factor driving gas exchange. We hypothesize that in rivers, especially rivers with strong currents, there would be a significant dependence of air-water gas exchange on flow velocity. Thus, our goal was to account for the flow's contribution to surface water mixing by modifying the original Wanninkhof (2014) Eq.4.1 to include the near-surface river flow speed.

We carried out a pilot study on the Yenisei River to directly determine and compare gas exchange in surface waters using a variety of approaches. The expedition lasted from July 23 to Aug 11, 2016, and we collected data on a section of the Yenisei River from ~56^o to ~68^o N (Fig. 4.1a). For that purpose, we chartered a small vessel (Fig. 4.1b) and outfitted it with the necessary instruments. These included an Airmar 220WX Weather Station, which was installed on the mast approximately 10m above the river surface (Fig. 4.1b), a Rio Grande workhorse ADCP (600 kHz) which was mounted on the starboard side of the boat (Fig. 4.1c), and two radiation sensors, a Hukseflux SR11 pyranometer (incoming shortwave radiation) and a Hukseflux IR02 pyrgeometer (incoming longwave radiation), which were installed on the ship's bow (Fig. 4.1b). In addition, we implemented several deployments of high-frequency temperature sensors (RBR fast and RBR duo for profiling) mounted on standard fishing gear; and we made 12 cross-section transects in different parts of Yenisei River (Supplementary material, Fig. 4.6).

In order for the original methodology to account for the effects of the river's flow, we are trying to modify eq.1 by replacing the wind speed derived friction velocity u_* with a suitable near-surface water velocity scale. First, the wind speed and the surface stress (τ) are related via

$$\tau_{air} = \rho_{atm} * C_{Da} * u_{10}^2 \quad (4.2)$$

where ρ_{atm} is the density of air, and C_{Da} is the drag coefficient.

At the same time, the water friction velocity u_* is related to the wind stress by

$$\tau_{water} = \rho_{water} * u_*^2 \quad (4.3)$$

where ρ_{water} is water density.

In low wave conditions, we may assume that the stress of wind acting on the water surface from above will equal the stress acting on the surface from beneath (Thorpe 2007). Combining (2) and (3) we get:

$$u_{10} = u_* / [(\rho_{atm} / \rho_{water}) * C_{Da}]^{1/2} \quad (4.4)$$

So, we substitute the wind speed term in equation 1 (Wanninkhof 2014) with the friction velocity u_*.

$$k = 0.251 * \frac{u_*^2}{(\frac{\rho_{atm}}{\rho_{water}} * C_{Da}) * (Sc/660)^{1/2}} \quad (4.5)$$

In low wave conditions, we also can derive the friction velocity from beneath the surface using the "law of the wall" (LOW) to relate turbulent kinetic energy dissipation rates (ε) to u_*:

$$u_* = \sqrt[3]{\varepsilon \kappa z} \quad (4.6)$$

where κ is the von Karman constant (~ 0.4; Wieringa, 1980) and z is the distance from the boundary.

We will refer to estimate using eq. *4.*6 as a velocity scale (u_s) hereafter and assume that it could be used together with eq.*4.5*. In this case u_s and u_* are not equal but are related and u_s can be better suited to represent gas transfer dynamics in eq. 4.5. Thus we substitute u_* with u_s and get

$$k = 0.251 * \frac{u_s^2}{\left(\frac{\rho_{atm}}{\rho_{water}} * C_{Da}\right) * (Sc/660)^{1/2}} \qquad (4.7)$$

During the expedition we had mostly wave-free conditions thus the applicability of LOW was justified with our dataset, as the LOW relationship would be valid in the absence of wave conditions with shear-induced mixing (Lorke and Peeters, 2006). Finally, *k* was calculated with both the commonly used wind-based Wanninkhof (2014) approach and the new methodology proposed in this study given in Eq. 4.7.

We compute ε using the ADCP and meteorological data in conjunction with the General Ocean Turbulence 1D model (GOTM) framework (Burchard et al., 1999; Umlauf et al., 2005). The vertical mixing was parameterized using the two-equation k-ε turbulence model.1 minute averaged velocity profiles from the ADCP and 1 minute averaged wind data from the meteorological suite were used as the forcing input for model simulations with a vertical bin size of 0.5 m and a time step of 1 minute. Four different experiments under different forcing conditions were implemented in GOTM: 1) wind only forcing; 2) River currents only forcing; 3) Wind + River currents forcing 4) 12 river cross-section simulations under Wind + River currents forcing. The velocity scale (u_s) was then derived using the LOW equation (Eq. 4.6) applied to

the first bin (located at 0.5 m depth): The quality control of ADCP data was based on the correlation and percentage of good criteria, which were above 120 counts and 25 % correspondingly. The quality of the ADCP data was further confirmed by comparing our Yenisei River discharge estimates (based on ADCP cross-sections) with the discharge estimates from the Russian Roshydromet. The two independent estimates agreed well with a correlation coefficient r^2= 0.99 (Fig. 4.9).

In order to further analyze the vertical structure of mixing we used RBR duo temperature profiles and ADCP velocity profiles to compute the buoyancy frequency field ($N^2 = -(g/\rho)\partial\rho/\partial z$, where ρ is the potential density); the Richardson number ($Ri = N^2/S^2$, where S is the vertical shear of the horizontal currents (Miles, 1964)) and Thorpe overturn scales (L_T). L_T was calculated by sorting the density profiles computed using temperature RBR duo profiles and finding to which depth the original density had to be shifted vertically in order to produce a stable density profile (Gargett and Garner, 2008).

Besides using the ADCP and wind data in *k* computations, we also used the approach of parametrizing k with river stream hydraulic geometry. We used three best performing parametrizations (r^2>0.7 when comparing results with observations) from Raymond et al. (2012, table 2, eq.1,2,7)

$$k_{600} = (VS)^{0.89}D^{0.54}5037 \quad (4.8)$$

$$k_{600} = 606(1-2.54Fr^2)(VS)^{0.89}D^{0.58} \quad (4.9)$$

$$k_{600} = 445(VS)^{0.86}Q^{-0.14}D^{0.66} \quad (4.10)$$

where k_{600} is standardized k ($k_{600}=(600/Sc)^{-0.5}*k$); V is stream velocity; S is slope; D is depth; Fr is Froude number ($Fr=V*(gD)^{-0.5}$); Q is discharge.

In addition, several atmospheric parameters were used to identify the effects of wind and heat fluxes on the water column. Thus, heat flux (H) was computed using

$$H = SW+LE+SE+LW, \quad (4.11)$$

where SW is net incoming shortwave radiation, LW is net longwave radiation, SE sensible heat flux, and LE is latent heat flux and were calculated using the COARE 3.6 code (Fairall et al., 2003). The fluxes were also used to calculate the Monin–Obukhov length scale ($L_{MO}= u_*^3/\kappa\beta$, where β is buoyancy flux) which assists in identifying the relative importance of momentum flux vs. buoyancy flux in driving water mixing (Csanady 2001).

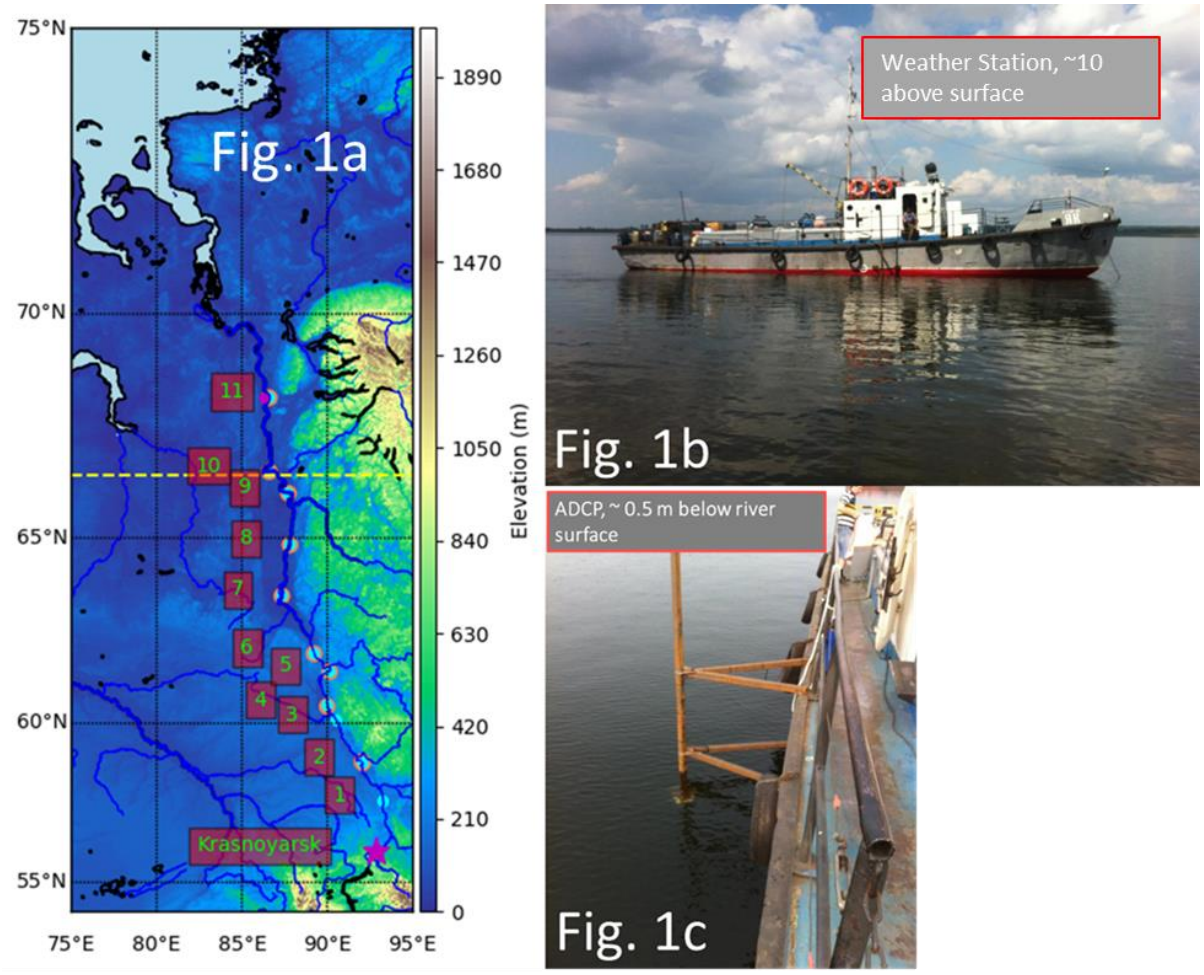

Figure 4.1 Study area (a), with station numbers where temperature profiles were taken; the ship with Weather Station setup (b), and ADCP mount (c).

4.3 *Results and Discussion*

The meteorological data shows the expected daily cycle for several parameters (Fig. 4.2a,b,c,d). Besides the obvious daily cycle, there is a relatively large change in water temperature around 58° N. This is explained by the confluence of Angara River, which is warmer than the Yenisei River, which is supplied with cold bottom waters from a reservoir south

of Krasnoyarsk. Overall the air temperature drops towards the North. In contrast, water temperatures remain nearly constant after the Angara confluence, resulting in increased heat flux loss to the atmosphere towards the higher latitudes (Fig. 4.2d). LMO values increase towards higher latitudes. As the measurements were collected mainly during the daytime, we can see positive values of LMO during the expedition. This implies that there were no convective forcing conditions observed, suggesting that the wind was mainly influencing turbulence production relatively to buoyancy forcing (Fig. 4.2d). The overall negative heat fluxes can also be explained that the measurements were taken mainly during the daytime, resulting in a net heat flux into the water. The measured wind speeds showed relatively high values towards the end of the cruise, with values exceeding 10 m/s (Fig. 4.2e). This resulted in the higher wind stress and thus higher surface u_* values (Fig. 4.2f). The average direction of the wind was southwest during this expedition (Fig. 4.2e).

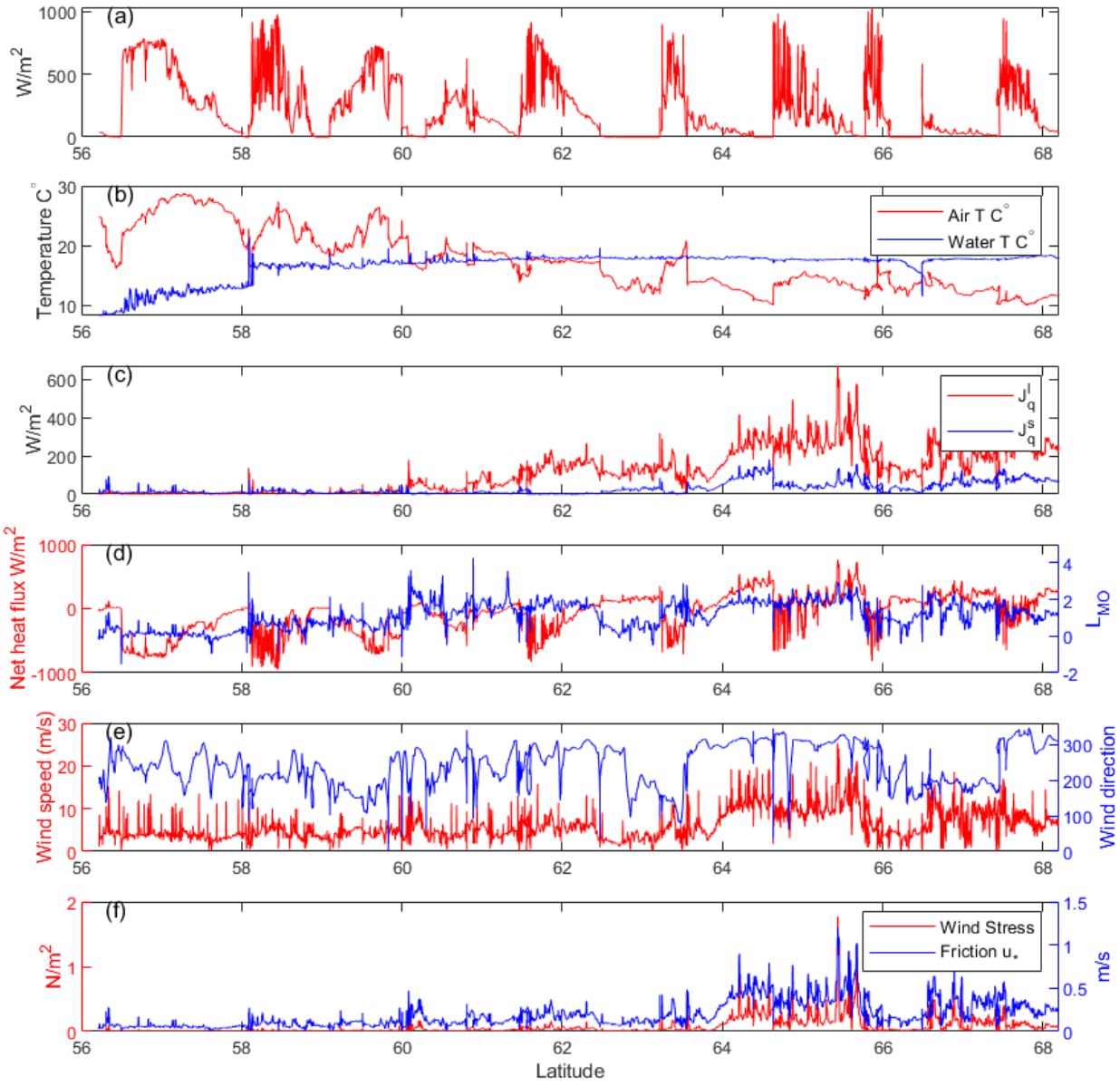

Figure 4.2 Meteorological data a) shortwave radiation; b) air (red) and water (blue) temperatures (at .5m depth); c) latent (red) and sensible (blue) heat fluxes; d) buoyancy flux with positive/negative values indicating flux from/into water (red) and the Monin–Obukhov length scale – (L_{MO},blue); e) wind speed (red) and wind direction from the origin (blue); f) wind stress (red) and u_*computed from wind.

The observed temperature profiles indicate a well-mixed water column and homogeneous temperature patterns (Fig. 4.3a). We can see an increasing temperature pattern towards the end of the expedition in the north. However, the vertical structure of temperatures doesn't show any sign of stratification in the water column. The *N* pattern confirms a well-mixed environment along the observed river stretch (N < 0.01 s-1; Fig. 4.3b). These results are also confirmed by the squared vertical shear (S^2) and Richardson number values (Fig. 4.3c,d). Thorpe displacement estimates show rather large overturns of O (1m, Fig. 4.3e), i.e., occupying a significant vertical portion of the water column. This also points to the strong mixing conditions in the Yenisei River. The fields presented in Figure 4.3 suggest a very homogeneous, well-mixed environment without any detectable vertical structures within the water column. This is not surprising considering that average current velocities exceeded 1 m/s in the main channel of the Yenisei River.

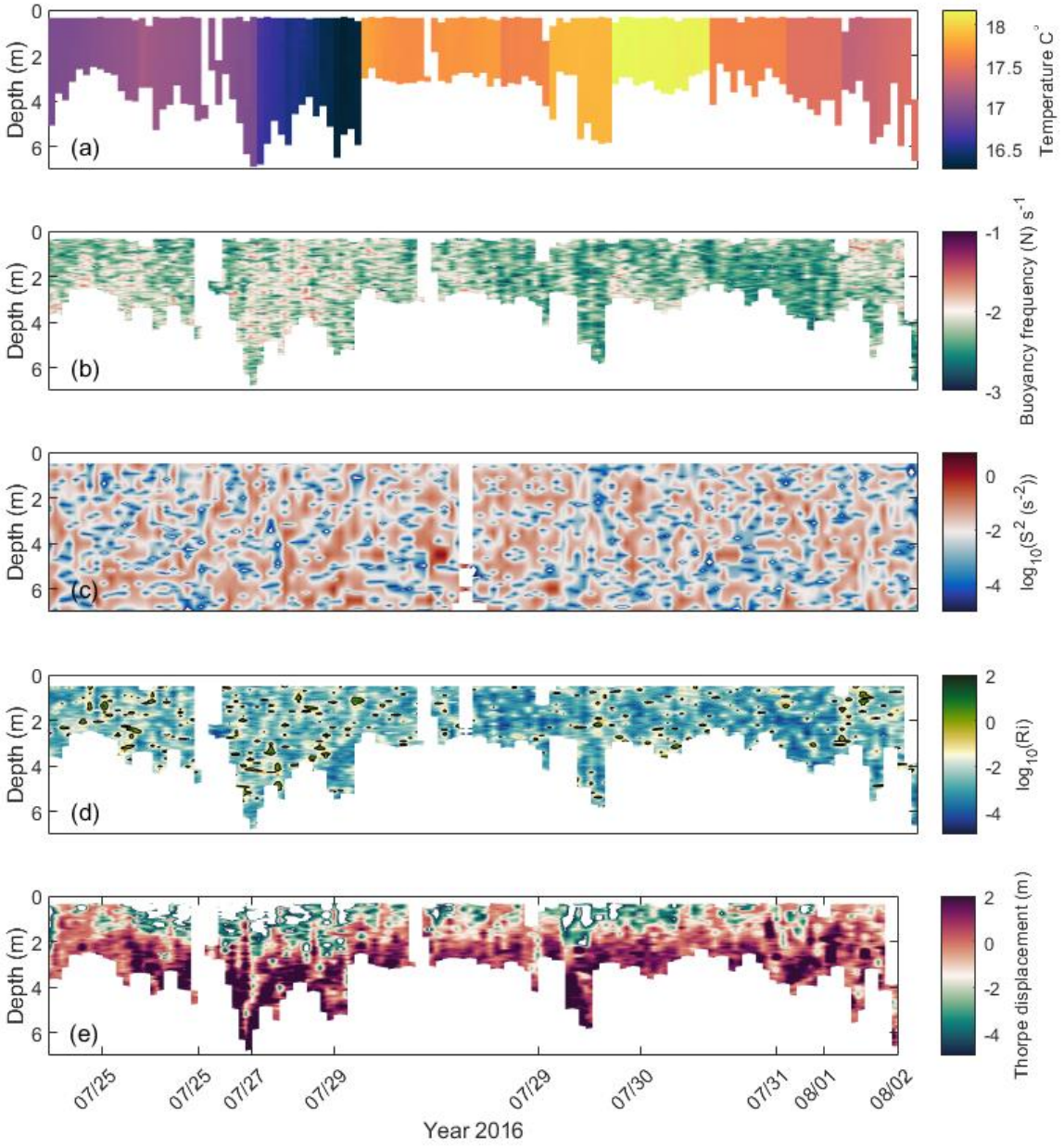

Figure 4.3 Profiles of Temperature (a), Buoyancy frequency (N, b), vertical shear (S^2; c), Richardson number (*Ri*, d) and Thorpe overturn scales (L_T; e).

Turbulent kinetic energy (TKE) dissipation rates, estimated using the GOTM (Fig. 4.4a) forced by the ADCP measured currents and the observed surface meteorological parameters,

show that the Yenisei river is a highly turbulent environment with ε values ranging from 10^{-6} to 10^{-4} W/kg. Generally, GOTM produces a wider range of ε values for the "wind scenario" while "currents" and "currents plus wind" scenarios produce very consistent ε values, typical of highly mixed environments, during the entire observational period. This is consistent with the results above, using temperature profiles. When comparing the u_* based on the wind (Eq. 4.4) and the results from the GOTM "currents plus wind" output, it becomes evident that the wind-based estimates underestimate the gas exchange coefficients for the majority of the observational record. The wind based estimates only agreed with the turbulence derived estimates towards the end of the expedition, when the data showed strong winds (> 10m/s; Fig. 4.2e). The wind-only approach underestimates the current and turbulence based values for most of the observational record, consistent with previous comparison of u_s results (e.g., Esters et al., 2017).

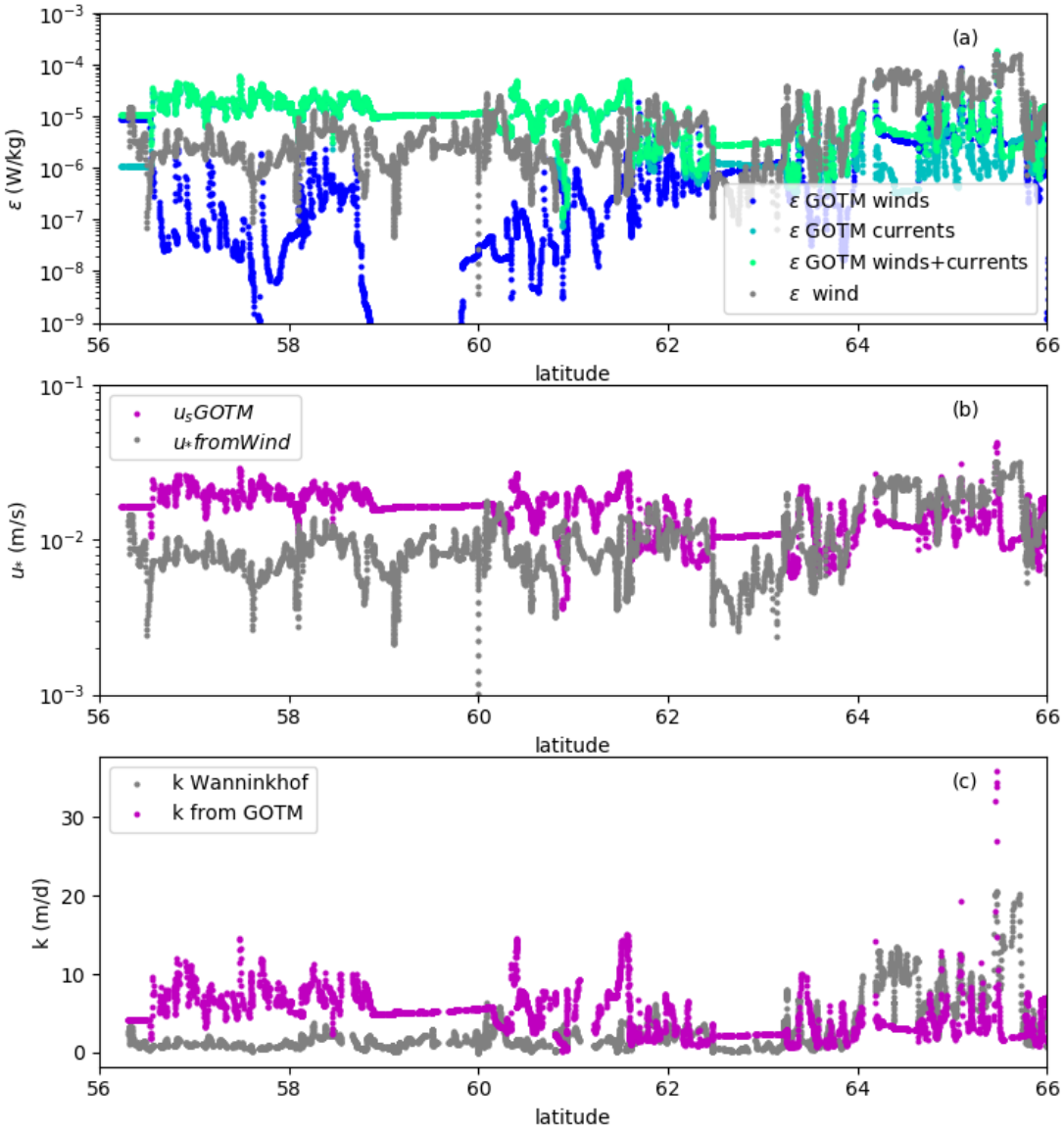

Figure 4.4 a) ε estimated by the GOTM, forced with meteorological and/or velocity profiles; b) u_* computed from wind only (gray) and u_s from GOTM simulations forced by currents + wind scenario (purple); c) *k* computed from wind only (grey) and from GOTM simulations forced by currents + wind scenario (purple).

River cross-sections taken along the expedition's route showed different channel and flow structures (Supplementary material, Fig. 4.8). Yenisei river channel usually consists of the deeper east part with higher velocities and the shallower western part with the slower flow. Thus, the importance of streamflow velocity and mixing is obvious in cross river sections where on average, the western side of the river is characterized by a slower flow and the eastern side by more rapid flow and more turbulent conditions (ADCP current data), translating into higher ε and *k* values on the eastern side of the Yenisei river (Fig. 4.9). However, after the confluences of big rivers (e.g., Angara, Podkamennaya Tunguska, etc.) there are so-called two-channel structure regions located along the Yenisei, which exhibit two deep parts, which also affect the mixing pattern across the river. The cross-sections which were taken in the northern part of the expedition show that towards the north, Yenisei gets deeper, and velocities are decreasing across the whole river channel. This translates to mixing strength and thus *k* values, with lateral *k* values dropping towards the north if we exclude strong wind events (fig. 4.4c).

Our results suggest that large Arctic boreal rivers represent highly turbulent environments with low wave conditions, where the gas transfer velocity *k* depends more on the river flow conditions rather than solely on the wind conditions. Recent studies tried to parametrize *k* with ε data using a SEM, which implies a direct relationship between *k* and ε (Zappa et al., 2007; Esters et al., 2017). Esters et al., 2017 validated the SEM model and derived an approximation of k based on the results of their study (Fig. 4.5 yellow and green lines). In comparison to their derived functions and results from Wanninkhof (Fig. 4.5 light and dark blue lines) the function derived in our study (Fig. 4.5, red line) falls below the other estimates. This can be explained by the fact that waves were not taken into account in our approach, as conditions during our cruise represented mostly wave-free conditions. Overall we can see that the method proposed by this

study has the slowest increasing curve compared to other methodologies (Fig. 4.5, red line), while wind-based approaches have faster-increasing functions (Fig. 4.5, blue lines). In the case of this study, the proposed method is giving higher gas exchange coefficients for the Yenisei River compared to solely wind-based estimates, even though it has a slower growing function.

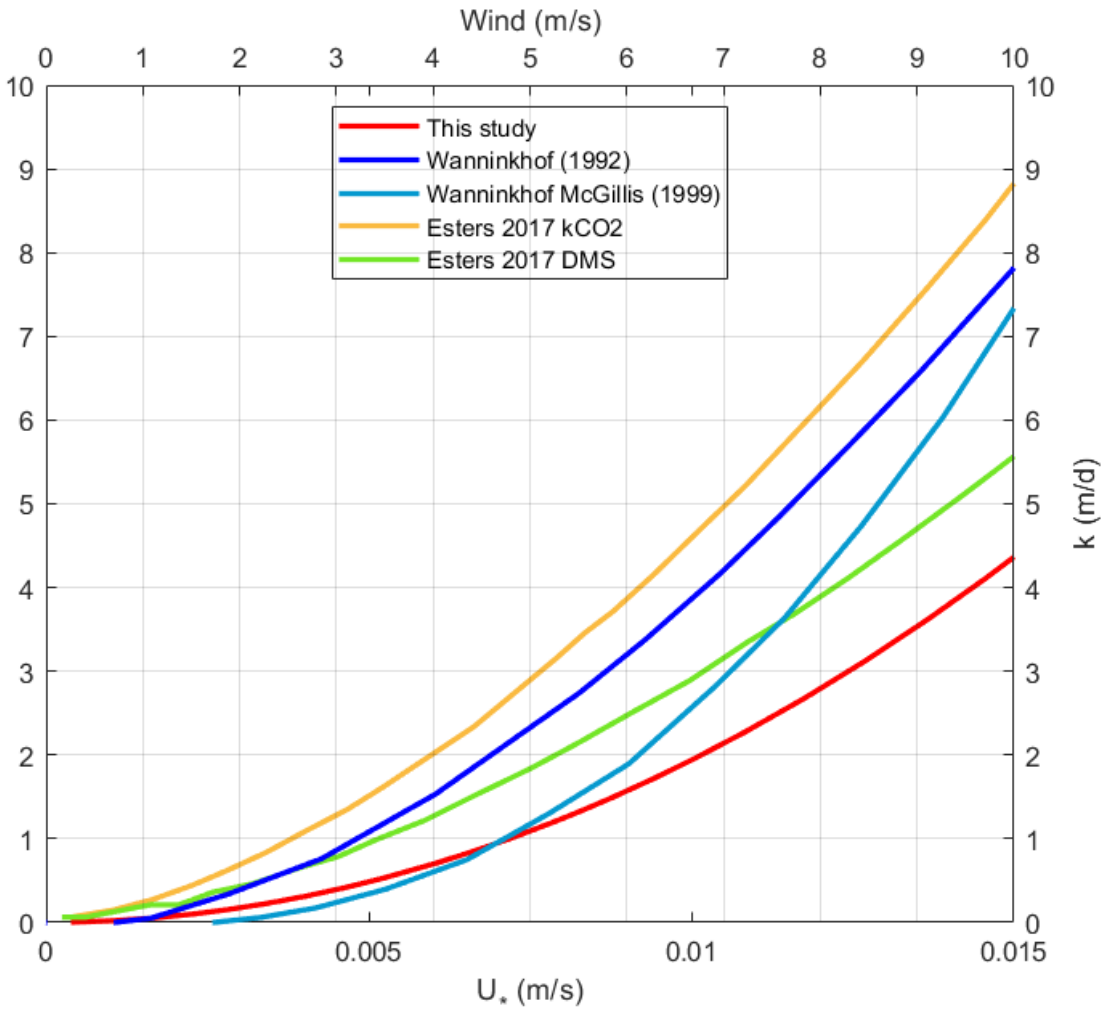

Figure 4.5 Comparison of different parameterization schemes for gas transfer velocity: red line – this study, using u_* (based on GOTM run with ADCP and wind data) and Eq.5; blue line (Wanninkhof, 1992); light blue line (Wanninkhof and McGillis, 1999); green line (Esters et al., 2017) DMS; orange line (Esters et al., 2017).

Comparing the results of this study to other boreal environments, it is evident that the Yenisei River has higher gas exchange rates than other Northern Hemisphere boreal environments but agrees very well with other large Arctic rivers (Fig. 4.6). Striegl et al. (2012) reported mean values of k 0.3, 1.9, and 3.6m/d for the upper, middle, and lower Yukon delta, respectively; MacIntyre et al. (2020) showed that the average *k* value is ~ 0.79 in a boreal lake in Sweden. The mean *k* value for the Yenisei River observed in this study is 4.48 m/d and coincides rather well with an in-situ average value of 4.46 observed in the Ob River using floating chambers (Karlsson et al., 2021). Wind-based estimates show the average *k* values for the Yenisey River around 2.7 m/d and 1.6 m/d, excluding high wind conditions at the northernmost portion of the study region. Thus, it becomes evident that approaches based solely on wind tend to underestimate the gas transfer in the Yenisei River due to the significant water velocities, which is the main driver of turbulent mixing and the gas exchange coefficient (Fig. 4.4a,c).

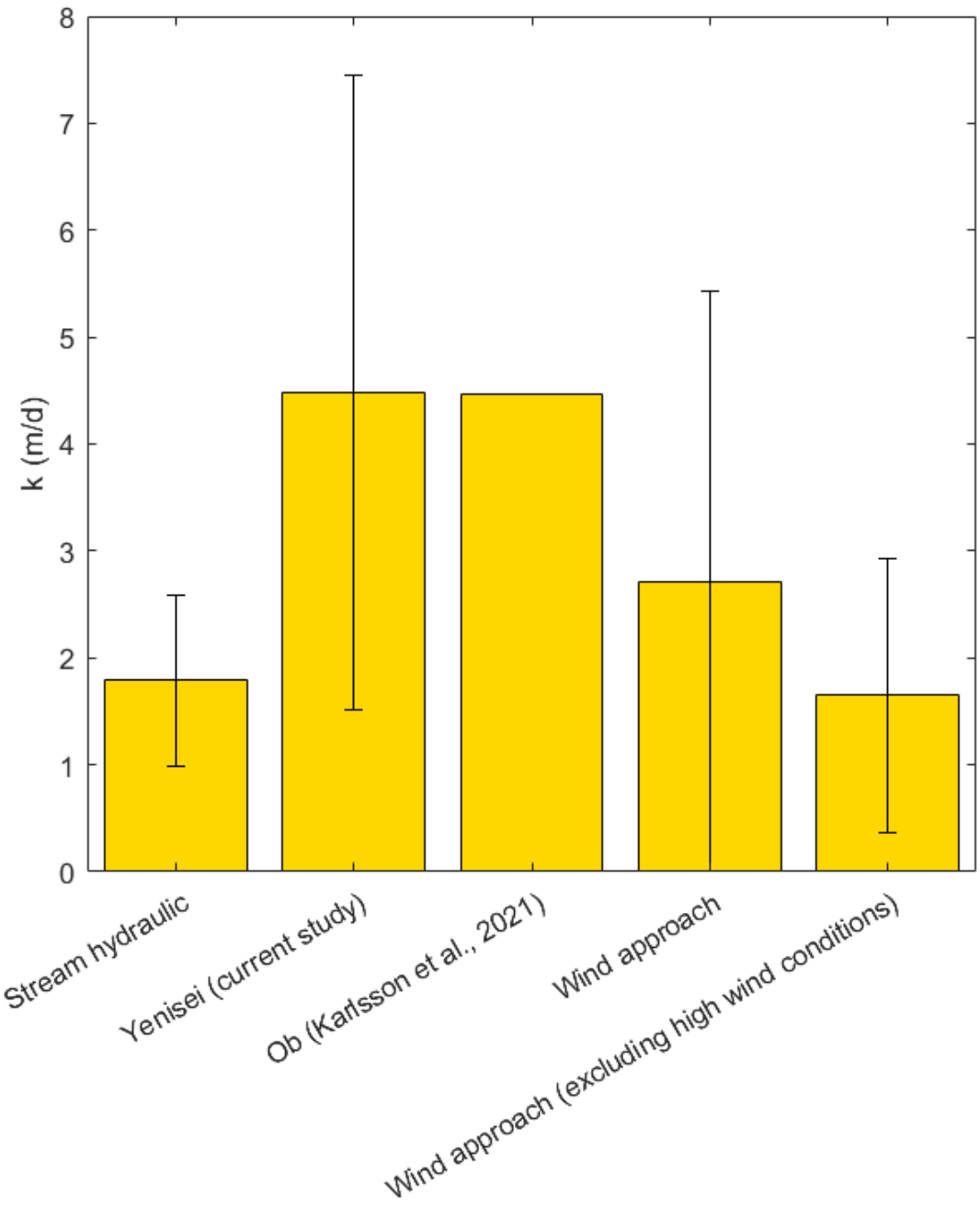

Figure 4.6 Barplot of k values using different approaches and observations from Karlson et al. 2021. Error bars indicate 1 standard deviation.

Furthermore, the estimations of *k* using the proposed methodology are within the range of values reported by Raymond et al. (2012), which were calculated using the stream hydraulic geometry. Equations 1, 2, and 7 (Raymond et al., 2012, table 2) resulted in *k* values of 1.97, 2.49, and 0.92 m/day, respectively, and would therefore somewhat underestimate our observed values. The Yenisei River can be divided into two sections based on the slope, as the slope of the river decreases substantially north of ~65^0 N from O(10^{-5}) to O(10^{-6}). Thus, if we calculate *k* based on stream hydraulics separately for these two regions, we get average values for the three equations of ~2.49/0.59 m/d for the region South/North of 65^0 N, correspondingly. This difference in the elevation change affects stream velocities and is also reflected in the values based on direct ADCP measurements. The region south of 65^0 N yields an average *k* value of 5.17 m/day, while the northern region yields a *k* value of 2.57 m/d (Fig. 4 c).

4.4 *Conclusions and future recommendations*

In this study, we showed that the parameterization for gas exchange coefficients in rivers is strongly dependent on the flow conditions rather than the wind speed. The alternative SEM methodology (Esters et al., 2017), which relates k to ε, depends on direct ε observations, which are usually challenging to collect, especially as continuous observations in rivers. Thus, the proposed methodology of using the GOTM offers an improvement to the original wind-only-based approach (Wanninkhof 2014), allowing a more realistic estimation of k in river environments. We showed that the wind-based approach underestimates the air-water gas transfer coefficients in most of the study area. This, in turn, would underestimate the overall GHG fluxes in this region.

The proposed methodology could be further improved and validated using instruments designed to observe turbulence directly. For future studies, we recommend using a high-

frequency ADCP (such as Nortek Signature 1000; Shcherbina et al., 2018) to continuously collect current data, which can be used to derive direct estimates of ε. In addition, it would be beneficial to use turbulence profilers (i.e https://rocklandscientific.com/products/profilers/microctd/) at discrete stations to collect direct observations of turbulence profiles in river water columns. The direct measurement of turbulence will allow further improvements of the accuracy of air-water gas exchange coefficients relative to the other approaches described here. Also, a high-frequency ADCP will allow measurements in shallow tributaries, which will contribute to the understanding of the overall gas exchange pattern in large boreal river networks.

The carbon cycle in boreal environments is still poorly studied. The lateral transport of carbon from these large boreal watersheds is dependent on DOC run-off, and in-channel respiration and the gas exchange between rivers and the atmosphere represents an underappreciated component and needs to be taken into account. Variable approximations of *k* may introduce further uncertainties in total carbon flux calculations. The observed data and the methodology proposed in this study showed that wind-based approaches underestimate the gas exchange, suggesting that the strong currents of the Yenisei River likely govern much of the gas transfer at the air-water interface. Thus, the results of this study might be used to better quantify the net lateral carbon fluxes from these vast boreal watersheds.

4.5 *Supplementary material*

During the ship expedition we performed 10 cross river sections at different latitudes (Fig.4.7). Transects show the velocity structure of the main channel from the western to the eastern river banks along the expeditions route (Figure 4.7b).

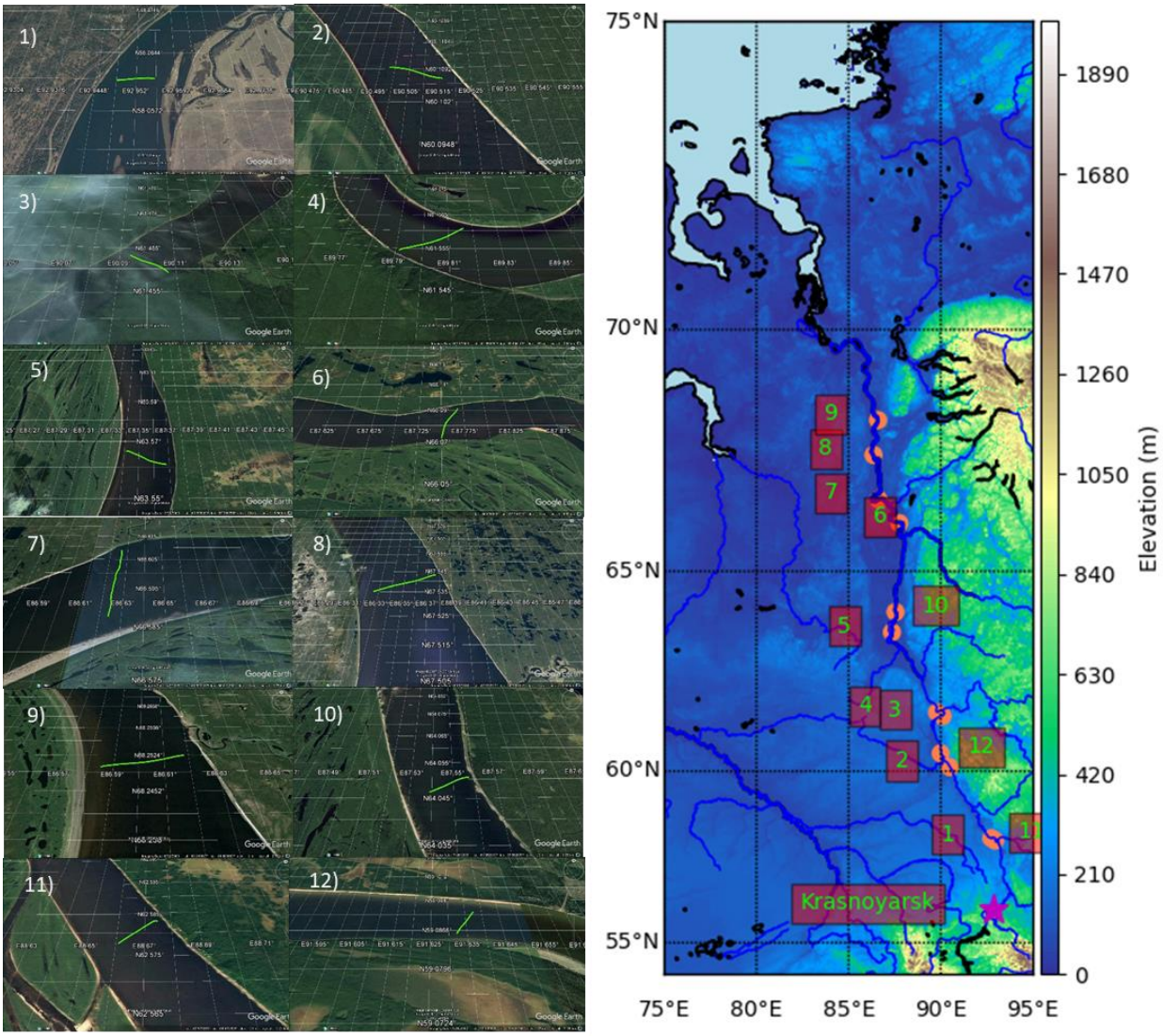

Figure 4.7 transect locations along Yenisei River: separate locations on Google Earth images (panels 1-12 on the left); map with the locations (right panel).

The channel structure can be separated into three different groups: 1) the Yenisei before the confluence with the big tributaries, with a well-defined main channel showing relatively large river currents; 2) the Yenisei after the confluence of a big tributary (i.e., Angara confluence) with two main channels; 3) the northern part (above polar circle) of the study area where the river channel relatively deeper and wider with slower flow velocities. Only one transect (Fig. 4.8, transect 1) was taken before the Angara river confluence, and another was taken right after the Angara confluence (Fig. 4.8, transect 11). We can see a clear two-channel structure on transect 11. Transect 3 (Fig. 4.8) was taken before the Podkamennaya Tunguska confluence and transect 5 (Fig. 4.8) right after the confluence. Here we can also see the two-channel structure of the river with higher velocities inside these channels. Transect 6 (Fig. 4.8) was taken after Nizhnyaya Tunguska River and exhibited a similar structure, with the second channel being more shallow with smaller velocities (Fig. 4.8, transect 6). Transect 8 and 9 are the most Northern ones with wider and deeper channel cross-sections. It is evident from ADCP data (Fig. 4.8) that water velocities were smaller compared to more southern transects. This might also be an effect of low water and drought conditions prevailing in summer 2016 in this region.

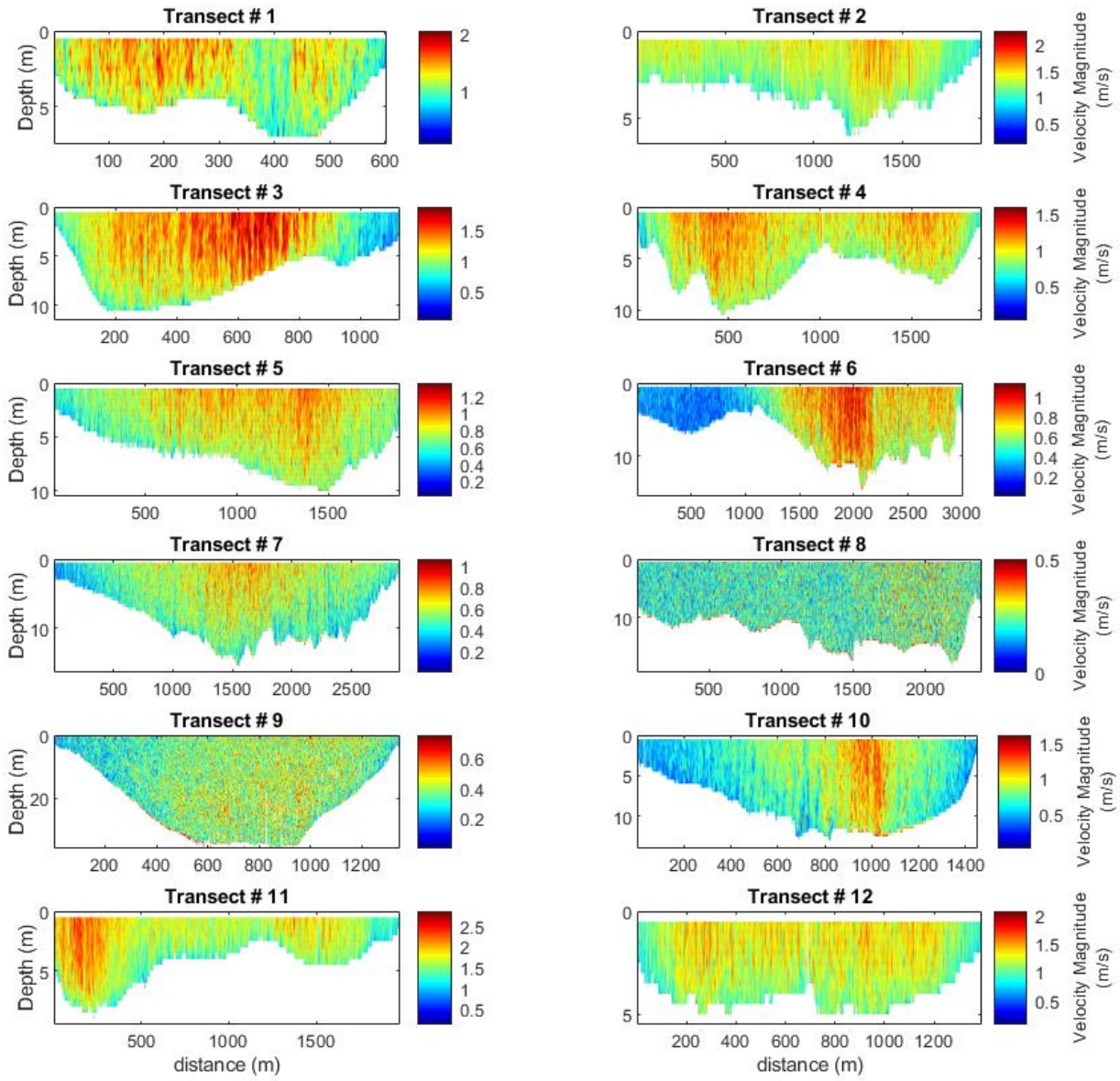

Figure 4.8 ADCP velocity magnitude (m/s) transects across Yenisei River at different latitudes. Transects are plotted in west-east orientation.

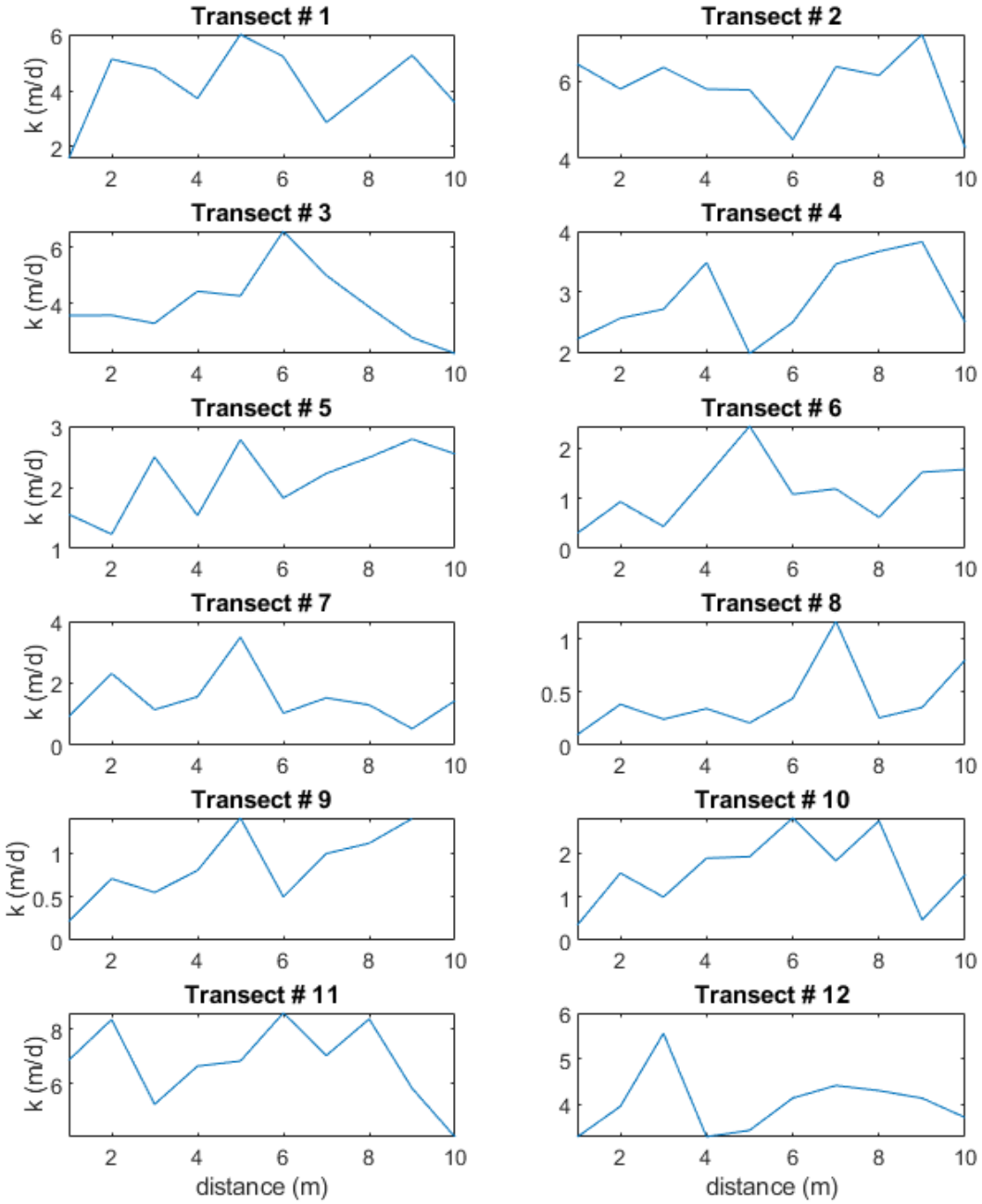

Figure 4.9 *k* values derived using ten different points along each transect across Yenisei River.

It is also evident from the data that the current velocities were dropping with increasing latitude. This affected the k values, which were also lower in the northern part of the expedition (Fig.4.9 transects 6,7,8,9,10). There is a detectable gradient in currents across the river. Sometimes there is the main channel with higher velocities, and sometimes there is two-channel system in the river, usually after the confluence of a big river. It also translates to the k value gradient across the river, with one shore having larger k values than another (Fig.4.8-4.9 transects 1,4,11). The results of computed discharge (Q) from ADCP transect observations agree very well with Roshydromet river gage data (Fig.4.10) with R^2 value of 0.98 between two datasets, showing the reliability of ADCP measurements.

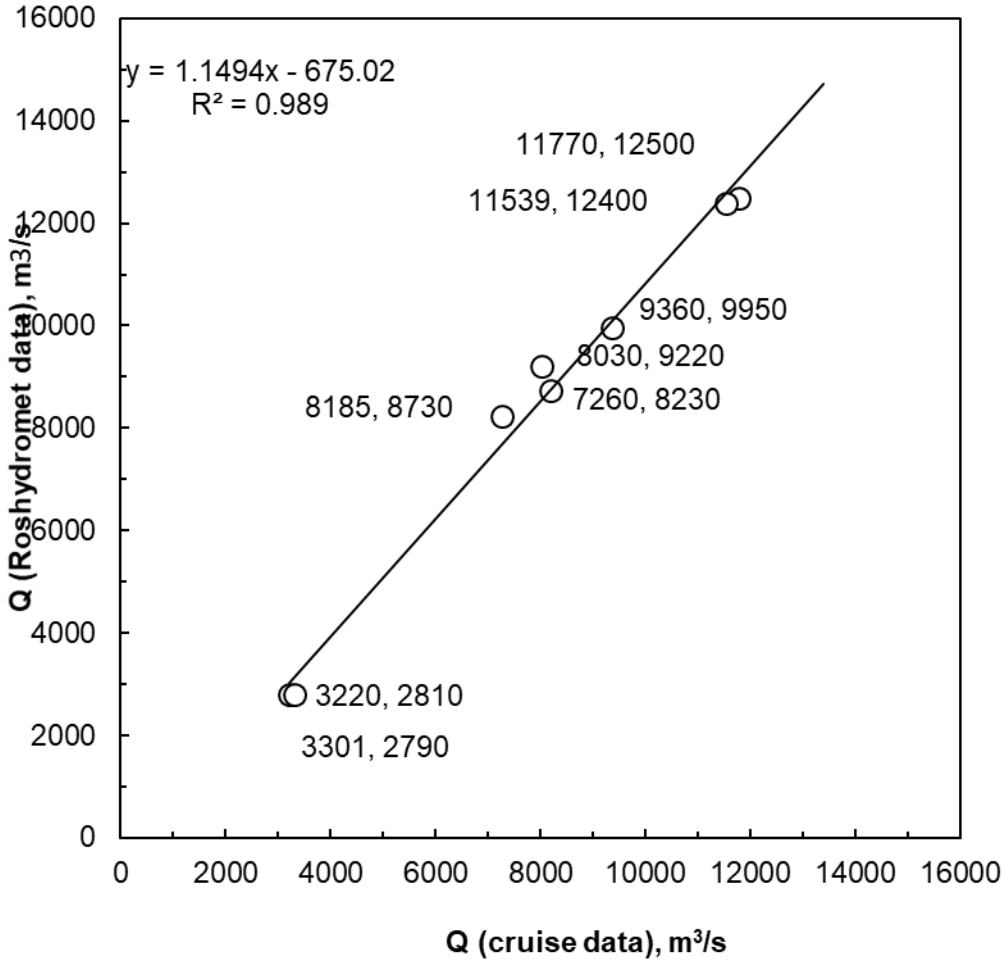

Figure 4.10 Linear regression fit between ADCP discharge estimates (x axis) and river gage data (y axis).

Separate temperature profiles taken during the expedition (Fig. 4.1b) show very mixed vertical temperature structure within the river water column (Fig.4.11).

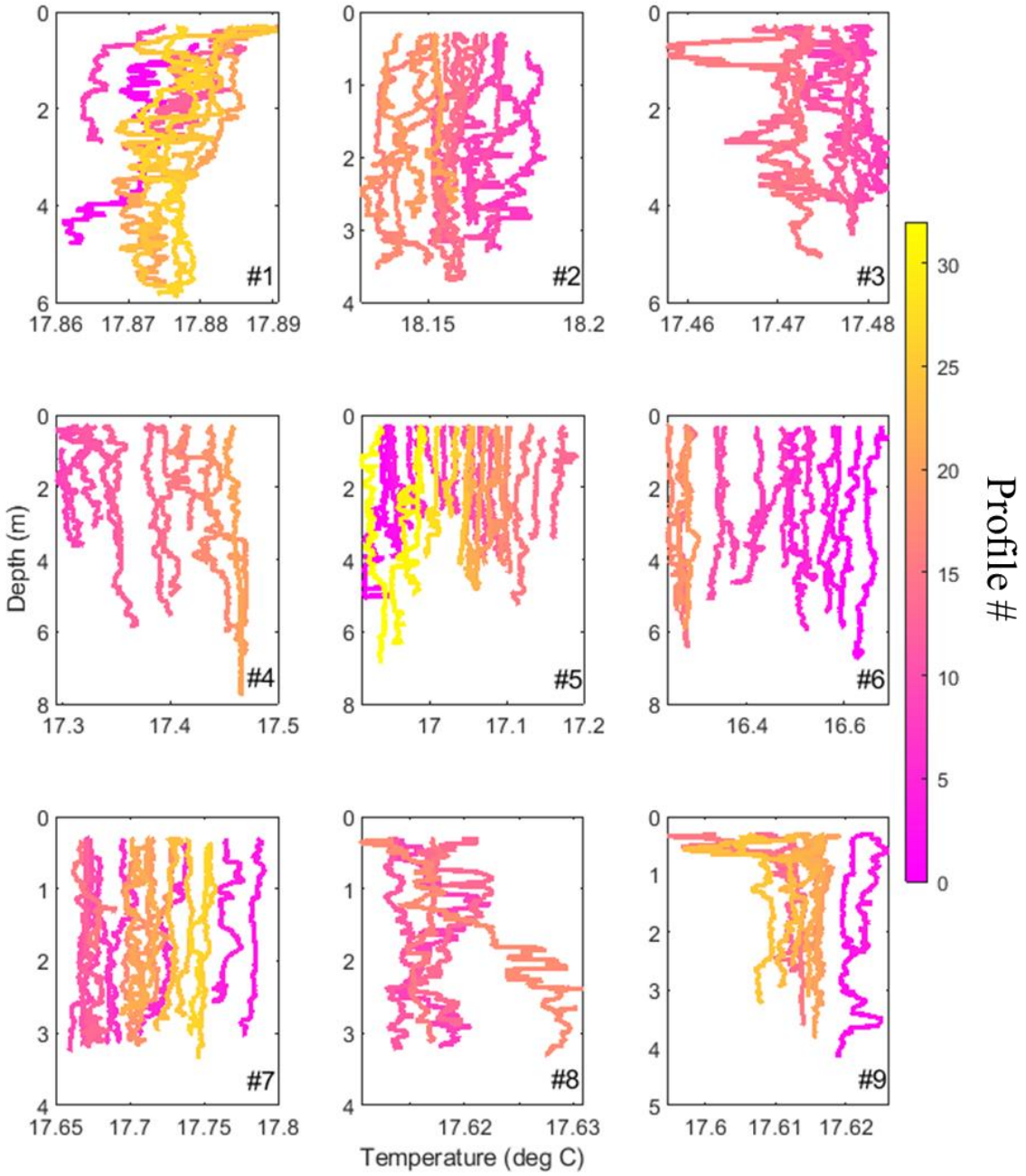

Figure 4.11 Individual temperature profiles suing RBR duo sensor.

5. SUMMARY AND CONLUSION

This work presented the analysis of turbulence observations in different parts of Earth's hydrosphere – open/coastal ocean and large boreal rivers. The results of this work are improving our understanding of the dynamical processes important in these regions. The first two chapters are devoted to better understanding mixing processes in the GOM.

The first study is focused on the investigation of the vertical mixing structure within large anticyclonic LCE and assessing the heat and salt fluxes associated with such an eddy. LCE introduces heat and salt anomalies to the GOM, bringing Subtropical underwater water mass to the region. This water is different from the surroundings in terms of salt and heat content. With the dissipation of LCE, this water is being mixed into the GOM, bringing additional salt to the region and balances for the freshwater inflow by rivers, including the Mississippi, to GOM. The so-called Double Diffusion process of thermohaline intrusions was found to take place on the eddy edge, representing the primary driver of eddy dissipation. The thermohaline intrusions produce relatively large horizontal fluxes compared to vertical fluxes and resulted in a lifespan of the eddy of ~1.5 years, which is very consistent with the eddy lifetime estimates by other studies (Fine et al., 2018; Meunier et al., 2020).

The second GOM study targeted the western part of the GOM, particularly the southwestern coastal area with the steepest continental slope. We observed stronger turbulence along the continental slope, which was caused by the breaking of internal tides. This leads to increased vertical diffusivity values (up to 10^{-3} m^2/s), which in turn create upwelling favorable conditions (e.g., Munk 1966; Hasumi and Suginohara, 1999). Based on our results, we think that this region can be a pathway for deep waters of the GOM to upwell and therefore help to ventilate the deep GOM. Recent studies (Ochoa et al., 2021, Amon et al., in prep) proposed a

conceptual model of deep GOM circulation where the Yucatan Channel sill water entering the GOM sinks and fills the deep GOM through the Yucatan channel. In order to retain mass balance, this continuously supplied deep water has to upwell and create intermediate waters, which form the outflow of the GOM, thus ventilating the deep GOM on time scales <100 years (Ochoa et al. 2021). The western GOM has the steepest continental slope within the gulf, thus being the best location to facilitate upwelling. Our findings confirm higher mixing values along the slope in this region and support the proposed theory.

The 3rd study is focused on the role of mixing processes for the gas exchange coefficient in one of the largest boreal Russian rivers, the Yenisei River. We proposed a new methodology to derive gas exchange coefficient using ADCP and high-frequency temperature sensor data and compared the results to the traditionally used approach based on wind data (Wanninkhof 2014). We proposed to use the water velocity scale to derive the gas exchange coefficient (*k)*. As we were limited with the observational tools, we determined the velocity scale (u_s) using the law of the wall (Lorke and Peeters, 2006) applied to GOTM output, forced with ADCP current and observational wind data. The results showed a clear difference of *k* estimates based on two parametrizations in the wind absent conditions, while during strong wind events, *k* values derived from two approaches matched better. This clearly shows the lack of skill of representation of air-water gas exchange for the river environments by wind-based approaches. During calm conditions, the currents still are capable of producing relatively large *k* values. The results of this study are important for assessing the lateral carbon fluxes from boreal ecosystems to the Arctic. It is not well understood how much carbon gets washed into rivers from the boreal forests and is transformed and transported to the Arctic Ocean. Moreover, it is uncertain how much of the riverine carbon escapes from rivers to the atmosphere through air-water gas

exchange. Determining this particular flux will require an accurate methodology to calculate *k* values. In order to further improve our results, we recommend directly observe turbulence in river surface waters rather than using the GOTM model approach. In order to do so, the new generation of high-resolution current profilers should be used because they allow direct observations of the turbulent kinetic energy (TKE) dissipation rates and provide a more accurate estimate of *k*.

In this dissertation, I showed that turbulence is responsible for controlling a wide range of processes in very different environments – from freshwater to marine systems and from shallow to deep waters. The direct observation of mixing strength was always a difficult metric to determine directly, leading to poor spatial and temporal data coverage of such observations. This dissertation contributed to the closing of this gap in data scarcity and shed more light on some of the important processes in the complex Earth System.

REFERENCES

Amon, R.M.W., Rinehart, A.J., Duan, S., Louchouarn, P., Prokushkin, A., Guggenberger, G., Bauch, D., Stedmon, C., Raymond, P.D., Holmes, R.M., McClelland, J.W., Peterson, B.J., Walker, S.A., (2012). Dissolved organic matter sources in large Arctic Rivers. Geochem. Cosmochim. Acta 94, 217–237.

Apel, J. R., Byrne, H. M., Proni, J. R., & Charnell, R. L. (1975). Observations of oceanic internal and surface waves from the Earth Resources Technology Satellite. Journal of Geophysical Research, 80(6), 865-881.

Baird, M. E., & Ridgway, K. R. (2012). The southward transport of sub-mesoscale lenses of Bass Strait water in the centre of anti-cyclonic mesoscale eddies. *Geophysical Research Letters, 39*(2)

Baker, M. A., & Gibson, C. H. (1987). Sampling turbulence in the stratified ocean: Statistical consequences of strong intermittency. *Journal of Physical Oceanography, 17*(10), 1817-1836.

Barceló-Llull, B., Sangrà, P., Pallàs-Sanz, E., Barton, E. D., Estrada-Allis, S. N., Martínez-Marrero, A., . . . Rodríguez-Santana, Á. (2017). Anatomy of a subtropical intrathermocline eddy. *Deep Sea Research Part I: Oceanographic Research Papers, 124*, 126-139.

Batchelor, G. K. (1959). Small-scale variation of convected quantities like temperature in turbulent fluid part 1. general discussion and the case of small conductivity. *Journal of Fluid Mechanics, 5*(1), 113-133.

Bebieva, Y. and Timmermans, M.L. (2016). An examination of double-diffusive processes in a mesoscale eddy in the Arctic Ocean. *Journal of Geophysical Research: Oceans*, *121*(1), pp.457-475.

Bôas, A. V., Sato, O. T., Chaigneau, A., & Castelão, G. P. (2015). The signature of mesoscale eddies on the air-sea turbulent heat fluxes in the South Atlantic Ocean. *Geophysical Research Letters, 42*(6), 1856-1862.

Burchard, Hans, Karsten Bolding, and Manuel R. Villarreal. GOTM, a general ocean turbulence model: theory, implementation and test cases. Space Applications Institute, 1999.

Candela, J., Ochoa, J., Sheinbaum, J., Lopez, M., Perez-Brunius, P., Tenreiro, M., ... & Arriaza-Oliveros, L. (2019). The flow through the gulf of Mexico. Journal of Physical Oceanography, 49(6), 1381-1401.

Colas, F., McWilliams, J. C., Capet, X., & Kurian, J. (2012). Heat balance and eddies in the Peru-Chile current system. *Climate Dynamics, 39*(1-2), 509-529.

Csanady, G. T. (2001). Air-sea interaction: laws and mechanisms. Cambridge University Press.

Dargaville, Roger, David Baker, Christian Rödenbeck, Peter Rayner, and Philippe Ciais. "Estimating high latitude carbon fluxes with inversions of atmospheric CO 2." Mitigation and Adaptation Strategies for Global Change 11, no. 4 (2006): 769-782.

Davies, J. I., & Evans, W. C. (1964). Oxidative metabolism of naphthalene by soil pseudomonads. The ring-fission mechanism. Biochemical Journal, 91(2), 251.

Dolman, A. J., Shvidenko, A., Schepaschenko, D., Ciais, P., Tchebakova, N., Chen, T., ... & Schulze, E. D. (2012). An estimate of the terrestrial carbon budget of Russia using inventory-based, eddy covariance and inversion methods. Biogeosciences, 9(12), 5323-5340.

Elliott, B. A. (1982). Anticyclonic rings in the Gulf of Mexico. Journal of Physical Oceanography, 12(11), 1292-1309.

Eriksen, C. C. (1998). Internal wave reflection and mixing at Fieberling Guyot. Journal of Geophysical Research: Oceans, 103(C2), 2977-2994.

Esters, L., Landwehr, S., Sutherland, G., Bell, T. G., Christensen, K. H., Saltzman, E. S., ... & Ward, B. (2017). Parameterizing air-sea gas transfer velocity with dissipation. Journal of Geophysical Research: Oceans, 122(4), 3041-3056.
Esters, L., Landwehr, S., Sutherland, G., Bell, T. G., Christensen, K. H., Saltzman, E. S., ... & Ward, B. (2017). Parameterizing air-sea gas transfer velocity with dissipation. Journal of Geophysical Research: Oceans, 122(4), 3041-3056.
Everett, J. D., Baird, M. E., Oke, P. R., & Suthers, I. M. (2012). An avenue of eddies: Quantifying the biophysical properties of mesoscale eddies in the Tasman Sea. *Geophysical Research Letters*, *39*(16)

Fairall, C. W., Bradley, E. F., Hare, J. E., Grachev, A. A., & Edson, J. B. (2003). Bulk parameterization of air–sea fluxes: Updates and verification for the COARE algorithm. Journal of climate, 16(4), 571-591.

Fer, I., Peterson, A. K., & Ullgren, J. E. (2014). Microstructure measurements from an underwater glider in the turbulent Faroe Bank Channel overflow. Journal of Atmospheric and Oceanic Technology, 31(5), 1128-1150.

Fine, E.C., MacKinnon, J.A., Alford, M.H. and Mickett, J.B. (2018). Microstructure Observations of Turbulent Heat Fluxes in a Warm-Core Canada Basin Eddy. *Journal of Physical Oceanography*, *48*(10), pp.2397-2418.

Friedlingstein, P., Dufresne, J. L., Cox, P. M., & Rayner, P. (2003). How positive is the feedback between climate change and the carbon cycle?. Tellus B: Chemical and Physical Meteorology, 55(2), 692-700.

Gargett, A. E. (1984). Vertical eddy diffusivity in the ocean interior. *Journal of Marine Research*, *42*(2), 359-393.

Gargett, A., & Garner, T. (2008). Determining Thorpe scales from ship-lowered CTD density profiles. Journal of Atmospheric and Oceanic Technology, 25(9), 1657-1670.

Gent, P. R., & Mcwilliams, J. C. (1990). Isopycnal mixing in ocean circulation models. *Journal of Physical Oceanography, 20*(1), 150-155.

Gleckler, P. J., Durack, P. J., Stouffer, R. J., Johnson, G. C., & Forest, C. E. (2016). Industrial-era global ocean heat uptake doubles in recent decades. Nature Climate Change, 6(4), 394-398.

Griffies, S. M., Winton, M., Anderson, W. G., Benson, R., Delworth, T. L., Dufour, C. O., . . . Rosati, A. (2015). Impacts on ocean heat from transient mesoscale eddies in a hierarchy of climate models. *Journal of Climate, 28*(3), 952-977.

Grimshaw, R., Pelinovsky, E., & Talipova, T. (2007). Modelling internal solitary waves in the coastal ocean. Surveys in Geophysics, 28(4), 273-298.

Hamilton, P. (1990). Deep currents in the Gulf of Mexico. Journal of Physical Oceanography, 20(7), 1087-1104.

Hasumi, H., & Suginohara, N. (1999). Effects of locally enhanced vertical diffusivity over rough bathymetry on the world ocean circulation. Journal of Geophysical Research: Oceans, 104(C10), 23367-23374.

Hebert, D., Oakey, N., & Ruddick, B. (1990). Evolution of a Mediterranean salt lens: Scalar properties. *Journal of Physical Oceanography, 20*(9), 1468-1483.

Holbrook, W. S., & Fer, I. (2005). Ocean internal wave spectra inferred from seismic reflection transects. Geophysical Research Letters, 32(15).

Inoue, R., Yamazaki, H., Wolk, F., Kono, T. and Yoshida, J. (2007). An estimation of buoyancy flux for a mixture of turbulence and double diffusion. *Journal of physical oceanography*, 37(3), pp.611-624.

Ivey, G. N., & Nokes, R. I. (1989). Vertical mixing due to the breaking of critical internal waves on sloping boundaries. Journal of Fluid Mechanics, 204, 479-500.

Jayne, S. R., & Marotzke, J. (2002). The oceanic eddy heat transport. *Journal of Physical Oceanography*, *32*(12), 3328-3345.

Jouanno, J., Ochoa, J., Pallàs-Sanz, E., Sheinbaum, J., Andrade-Canto, F., Candela, J., & Molines, J. (2016). Loop current frontal eddies: Formation along the Campeche bank and impact of coastally trapped waves. *Journal of Physical Oceanography*, *46*(11), 3339-3363.

Kaiser K., M. Canedo-Oropeza, R. McMahon & R. M. W. Amon (2017), Origins and transformations of dissolved organic matter in large Arctic rivers, Scientific Reports 7, Article Number: 13064, doi:10.1038/s41598-017-12729-1

Karlsson, J., Serikova, S., Vorobyev, S. N., Rocher-Ros, G., Denfeld, B., & Pokrovsky, O. S. (2021). Carbon emission from Western Siberian inland waters. Nature communications, 12(1), 1-8.

Keenan, T. F., & Williams, C. A. (2018). The terrestrial carbon sink. Annual Review of Environment and Resources, 43, 219-243.

Kelley, D. E. (1990). Fluxes through diffusive staircases: A new formulation. *Journal of Geophysical Research: Oceans*, *95*(C3), 3365-3371.

Kitaigorodskii, S. A. "On the fluid dynamical theory of turbulent gas transfer across an air-sea interface in the presence of breaking wind-waves." Journal of physical oceanography 14, no. 5 (1984): 960-972.

Klymak, J. M., Legg, S., Alford, M. H., Buijsman, M., Pinkel, R., & Nash, J. D. (2012). The direct breaking of internal waves at steep topography. Oceanography, 25(2), 150-159.

Kolodziejczyk, N., Ochoa, J., Candela, J., & Sheinbaum, J. (2012). Observations of intermittent deep currents and eddies in the Gulf of Mexico. *Journal of Geophysical Research: Oceans, 117*(C9).

Lamb, K. G. (2014). Internal wave breaking and dissipation mechanisms on the continental slope/shelf. Annual Review of Fluid Mechanics, 46, 231-254.

Laurila, T., Aurela, M., & Tuovinen, J. P. (2012). Eddy covariance measurements over wetlands. In Eddy covariance (pp. 345-364). Springer, Dordrecht.

Lavrova, O., & Mityagina, M. (2017). Satellite survey of internal waves in the Black and Caspian Seas. Remote Sensing, 9(9), 892.

Ledwell, J. J. (1984). The variation of the gas transfer coefficient with molecular diffusity. In Gas transfer at water surfaces (pp. 293-302). Springer, Dordrecht.

Lorke, A., & Peeters, F. (2006). Toward a unified scaling relation for interfacial fluxes. Journal of Physical Oceanography, 36(5), 955-961.

Mahadevan, A., D'asaro, E., Lee, C., & Perry, M. J. (2012). Eddy-driven stratification initiates North Atlantic spring phytoplankton blooms. *Science, 337*(6090), 54-58.

McGillicuddy Jr, D. J., Robinson, A. R., Siegel, D. A., Jannasch, H. W., Johnson, R., Dickey, T. D., . . . Knap, A. H. (1998). Influence of mesoscale eddies on new production in the Sargasso Sea. *Nature, 394*(6690), 263.

MacIntyre, S., Bastviken, D., Arneborg, L., Crowe, A. T., Karlsson, J., Andersson, A., ... & Melack, J. M. (2020). Turbulence in a small boreal lake: Consequences for air–water gas exchange. Limnology and Oceanography.

McEwan, A. D. (1983). The kinematics of stratified mixing through internal wavebreaking. Journal of Fluid Mechanics, 128, 47-57.

McGuire, A. D., Anderson, L. G., Christensen, T. R., Dallimore, S., Guo, L., Hayes, D. J., ... & Roulet, N. (2009). Sensitivity of the carbon cycle in the Arctic to climate change. Ecological Monographs, 79(4), 523-555.

McMillan, J. M., Hay, A. E., Lueck, R. G., & Wolk, F. (2016). Rates of dissipation of turbulent kinetic energy in a high Reynolds number tidal channel. *Journal of Atmospheric and Oceanic Technology*, *33*(4), 817-837.

Ménesguen, C., Hua, B., Papenberg, C., Klaeschen, D., Geli, L., & Hobbs, R. (2009). Effect of bandwidth on seismic imaging of rotating stratified turbulence surrounding an anticyclonic eddy from field data and numerical simulations. *Geophysical Research Letters*, *36*(24)

Merckelbach, L., Smeed, D., & Griffiths, G. (2010). Vertical water velocities from underwater gliders. *Journal of Atmospheric and Oceanic Technology*, *27*(3), 547-563.

Merckelbach, L., Berger, A., Krahmann, G., Dengler, M., & Carpenter, J. R. (2019). A dynamic flight model for Slocum gliders and implications for turbulence microstructure measurements. Journal of Atmospheric and Oceanic Technology, 36(2), 281-296.

Meunier, T., Ménesguen, C., Schopp, R., & Le Gentil, S. (2015). Tracer stirring around a meddy: The formation of layering. *Journal of Physical Oceanography*, *45*(2), 407-423.

Meunier, T., Pallás-Sanz, E., Tenreiro, M., Portela, E., Ochoa, J., Ruiz-Angulo, A., & Cusí, S. (2018). The vertical structure of a loop current eddy. *Journal of Geophysical Research: Oceans*, *123*(9), 6070-6090. doi:10.1029/2018JC013801

Meunier, T., Pallás-Sanz, E., Tenreiro, M., Ochoa, J., Ruiz-Angulo, A., & Buckingham, C. (2019). Observations of Layering under a Warm-Core Ring in the Gulf of Mexico. *Journal of Physical Oceanography*, *49*(12), 3145-3162.

Meunier, T., Sheinbaum, J., Pallàs-Sanz, E., Tenreiro, M., Ochoa, J., Ruiz-Angulo, A., ... & de Marez, C. (2020). Heat Content Anomaly and Decay of Warm-Core Rings: the Case of the Gulf of Mexico. *Geophysical Research Letters*, *47*(3), e2019GL085600.

Miles, J. W., & Howard, L. N. (1964). Note on a heterogeneous shear flow. Journal of Fluid Mechanics, 20(2), 331-336.

Molinari, R. L., & Mayer, D. A. (1982). Current meter observations on the continental slope at two sites in the eastern Gulf of Mexico. Journal of Physical Oceanography, 12(12), 1480-1492.

Mowbray, D. E., & Rarity, B. S. H. (1967). A theoretical and experimental investigation of the phase configuration of internal waves of small amplitude in a density stratified liquid. Journal of Fluid Mechanics, 28(1), 1-16.

Mukherjee, S., Ramachandran, S., Tandon, A., & Mahadevan, A. (2016). Production and destruction of eddy kinetic energy in forced submesoscale eddy-resolving simulations. *Ocean Modelling*, *105*, 44-59.

Munk, W. H. (1966, August). Abyssal recipes. In Deep Sea Research and Oceanographic Abstracts (Vol. 13, No. 4, pp. 707-730). Elsevier.

Nasmyth, P. W. (1970). Oceanic Turbulence, *PhD dissertation.*

Nightingale, P. D., Liss, P. S., & Schlosser, P. (2000). Measurements of air-sea gas transfer during an open ocean algal bloom. Geophysical Research Letters, 27(14), 2117-2120.

Nikurashin, M., & Ferrari, R. (2013). Overturning circulation driven by breaking internal waves in the deep ocean. Geophysical Research Letters, 40(12), 3133-3137.

Oakey, N. S. (1982). Determination of the rate of dissipation of turbulent energy from simultaneous temperature and velocity shear microstructure measurements. *Journal of Physical Oceanography*, *12*(3), 256-271.

Ochoa, J., Ferreira-Bartrina, V., Candela, J., Sheinbaum, J., López, M., Pérez-Brunius, P., ... & Amon, R. M. (2021). Deep-Water Warming in the Gulf of Mexico from 2003 to 2019. Journal of Physical Oceanography, 51(4), 1021-1035, DOI: https://doi.org/10.1175/JPO-D-19-0295.1

Olascoaga, M. J., & Haller, G. (2012). Forecasting sudden changes in environmental pollution patterns. Proceedings of the National Academy of Sciences

Olascoaga, M.J., Beron-Vera, F.J., Haller, G., Trinanes, J., Iskandarani, M., Coelho, E.F., Haus, B.K., Huntley, H.S., Jacobs, G., Kirwan, A.D. and Lipphardt, B.L. (2013). Drifter motion in the Gulf of Mexico constrained by altimetric Lagrangian coherent structures. Geophysical Research Letters, 40(23), 6171-6175.

Olson, D. B. (1991). Rings in the ocean. *Annual Review of Earth and Planetary Sciences, 19*(1), 283-311.

Osborn, Thomas R. "Vertical profiling of velocity microstructure." Journal of Physical Oceanography 4, no. 1 (1974): 109-115.

Osborn, T. R. (1980). Estimates of the local rate of vertical diffusion from dissipation measurements. *Journal of Physical Oceanography, 10*(1), 83-89. doi:EOTLRO>2.0.CO;2

Palmer, M. R., Stephenson, G. R., Inall, M. E., Balfour, C., Düsterhus, A., & Green, J. (2015). Turbulence and mixing by internal waves in the Celtic Sea determined from ocean glider microstructure measurements. Journal of Marine Systems, 144, 57-69.

Pawlowicz, R., 2020. "M_Map: A mapping package for MATLAB", version 1.4m, [Computer software], available online at www.eoas.ubc.ca/~rich/map.html.

Pérez-Brunius, P., Furey, H., Bower, A., Hamilton, P., Candela, J., García-Carrillo, P., & Leben, R. (2018). Dominant circulation patterns of the deep Gulf of Mexico. Journal of Physical Oceanography, 48(3), 511-529.

Polzin, K. L., Toole, J. M., Ledwell, J. R., & Schmitt, R. W. (1997). Spatial variability of turbulent mixing in the abyssal ocean. Science, 276(5309), 93-96.

Portela, E., Tenreiro, M., Pallàs-Sanz, E., Meunier, T., Ruiz-Angulo, A., Sosa-Gutiérrez, R., & Cusí, S. (2018). Hydrography of the central and western Gulf of Mexico. Journal of Geophysical Research: Oceans, 123(8), 5134-5149.

Prokushkin, A. S., Tokareva, I. V., Prokushkin, S. G., Abaimov, A. P., Guggenberger G. (2008). Fluxes of Dissolved Organic Matter in Larch Forests in the Cryolithozone of Central Siberia. Russian Journal of Ecology, Vol. 39, No. 3, pp. 151–159.

Prokushkin A. S., Pokrovsky O.S., Shirokova L. S., Korets M.A., Viers J., Prokushkin S. G., Amon R. M. W., Guggenberger G. and McDowell W.H. (2011). Sources and the flux pattern of dissolved carbon in rivers of the Yenisey basin draining the Central Siberian Plateau. Environ. Res. Lett. 6 045212 (14pp) doi:10.1088/1748-9326/6/4/045212.

Putrasahan, D. A., Kamenkovich, I., Le Hénaff, M., & Kirtman, B. P. (2017). Importance of ocean mesoscale variability for air-sea interactions in the Gulf of Mexico. *Geophysical Research Letters, 44*(12), 6352-6362.

Raymond P. A., McClelland J. W., Holmes R. M., Zhulidov A. V., Mull K., Peterson B. J., Striegl R. G., Aiken G. R. and Gurtovaya T. Y. (2007). Flux and age of dissolved organic carbon exported to the Arctic Ocean: A carbon isotopic study of the five largest arcticrivers, Global Biogeochem. Cycles 21: GB4011, doi:10.1029/2007GB002934.

Raymond, P. A., Zappa, C. J., Butman, D., Bott, T. L., Potter, J., Mulholland, P., ... & Newbold, D. (2012). Scaling the gas transfer velocity and hydraulic geometry in streams and small rivers. Limnology and Oceanography: Fluids and Environments, 2(1), 41-53.

Reiche, S., Hübscher, C., Brenner, S., Betzler, C., & Hall, J. K. (2018). The role of internal waves in the late Quaternary evolution of the Israeli continental slope. Marine Geology, 406, 177-192.

Rivas, D., Badan, A., & Ochoa, J. (2005). The ventilation of the deep Gulf of Mexico. *Journal of Physical Oceanography, 35*(10), 1763-1781. doi:10.1175/JPO2786.1

Ruddick, B., Anis, A., & Thompson, K. (2000). Maximum likelihood spectral fitting: The batchelor spectrum. *Journal of Atmospheric and Oceanic Technology, 17*(11), 1541-1555.

Ruddick, B. R., Oakey, N. S., & Hebert, D. (2010). Measuring lateral heat flux across a thermohaline front: A model and observational test. *Journal of Marine Research, 68*(3-4), 523-539.

Rudnick, D. L., Gopalakrishnan, G., & Cornuelle, B. D. (2015). Cyclonic eddies in the Gulf of Mexico: Observations by underwater gliders and simulations by numerical model. *Journal of Physical Oceanography, 45*(1), 313-326.

Sansón, L. Z., Pérez-Brunius, P., & Sheinbaum, J. (2017). Surface relative dispersion in the southwestern Gulf of Mexico. Journal of Physical Oceanography, 47(2), 387-403.

Scheifele, B., Waterman, S., Merckelbach, L., & Carpenter, J. (2018). Measuring the dissipation rate of turbulent kinetic energy in strongly stratified, low-energy environments: A case study from the Arctic Ocean. *Journal of Geophysical Research: Oceans (1978–2012), 123*(8), 5459-5480. doi:10.1029/2017JC013731

Schultze, L. K., Merckelbach, L. M., & Carpenter, J. R. (2017). Turbulence and mixing in a shallow shelf sea from underwater gliders. *Journal of Geophysical Research: Oceans, 122*(11), 9092-9109.

Shay, L. K., Goni, G. J., & Black, P. G. (2000). Effects of a warm oceanic feature on hurricane opal. *Monthly Weather Review*, *128*(5), 1366-1383. doi:EOAWOF>2.0.CO;2

Shcherbina, A. Y., D'Asaro, E. A., & Nylund, S. (2018). Observing finescale oceanic velocity structure with an autonomous Nortek acoustic Doppler current profiler. Journal of atmospheric and oceanic technology, 35(2), 411-427.

Schuur, E. A., Abbott, B. W., Bowden, W. B., Brovkin, V., Camill, P., Canadell, J. G., ... & Zimov, S. A. (2013). Expert assessment of vulnerability of permafrost carbon to climate change. Climatic Change, 119(2), 359-374.

Schuur, E. A., McGuire, A. D., Schädel, C., Grosse, G., Harden, J. W., Hayes, D. J., ... & Vonk, J. E. (2015). Climate change and the permafrost carbon feedback. Nature, 520(7546), 171-179.

Shvidenko, A., Schepaschenko, D., McCallum, I., & Nilsson, S. (2010). Can the uncertainty of full carbon accounting of forest ecosystems be made acceptable to policymakers?. Climatic change, 103(1), 137-157.

Soden, B. J., & Held, I. M. (2006). An assessment of climate feedbacks in coupled ocean–atmosphere models. Journal of climate, 19(14), 3354-3360.

Sosa-Gutiérrez, R., Pallàs-Sanz, E., Jouanno, J., Chaigneau, A., Candela, J., & Tenreiro, M. (2020). Erosion of the Subsurface Salinity Maximum of the Loop Current Eddies From Glider Observations and a Numerical Model. Journal of Geophysical Research: Oceans, 125(7), e2019JC015397.

Striegl, R. G., Dornblaser, M. M., McDonald, C. P., Rover, J. R., & Stets, E. G. (2012). Carbon dioxide and methane emissions from the Yukon River system. Global Biogeochemical Cycles, 26(4).

Toole, J. M., Schmitt, R. W., Polzin, K. L., & Kunze, E. (1997). Near-boundary mixing above the flanks of a midlatitude seamount. Journal of Geophysical Research: Oceans, 102(C1), 947-959.

Thorpe, S. A. (1977). Turbulence and mixing in a Scottish loch. Philosophical Transactions of the Royal Society of London. Series A, Mathematical and Physical Sciences, 286(1334), 125-181.

Thorpe, S. A., & Haines, A. P. (1987). On the reflection of a train of finite-amplitude internal waves from a uniform slope. Journal of Fluid Mechanics, 178, 279-302.

Thorpe, S. A. (2007). An introduction to ocean turbulence (Vol. 10). Cambridge: Cambridge University Press.

Treguier, A. M., Held, I. M., & Larichev, V. D. (1997). Parameterization of quasigeostrophic eddies in primitive equation ocean models. *Journal of Physical Oceanography, 27*(4), 567-580. doi:POQEIP>2.0.CO;2

Umlauf, L., Burchard, H., & Bolding, K. (2005). GOTM-scientific documentation: version 3.2. Institut für Ostseeforschung.

Villas Bôas, A. B., Sato, O. T., Chaigneau, A., & Castelão, G. P. (2015). The signature of mesoscale eddies on the air-sea turbulent heat fluxes in the South Atlantic Ocean. *Geophysical Research Letters, 42*(6), 1856-1862.

Wanninkhof, R. (1992). Relationship between wind speed and gas exchange over the ocean. Journal of Geophysical Research: Oceans, 97(C5), 7373-7382.

Wanninkhof, R., & McGillis, W. R. (1999). A cubic relationship between air-sea CO2 exchange and wind speed. Geophysical Research Letters, 26(13), 1889-1892.

Wanninkhof, R., Park, G. H., Takahashi, T., Sweeney, C., Feely, R., Nojiri, Y., ... & Khatiwala, S. (2013). Global ocean carbon uptake: magnitude, variability and trends. Biogeosciences, 10(3), 1983-2000.

Wanninkhof, R. (2014). Relationship between wind speed and gas exchange over the ocean revisited. Limnology and Oceanography: Methods, 12(6), 351-362.

Whalen, C. B., de Lavergne, C., Garabato, A. C. N., Klymak, J. M., Mackinnon, J. A., & Sheen, K. L. (2020). Internal wave-driven mixing: governing processes and consequences for climate. Nature Reviews Earth & Environment, 1(11), 606-621.

Wieringa, J. (1980). A revaluation of the Kansas mast influence on measurements of stress and cup anemometer overspeeding. Boundary-Layer Meteorology, 18(4), 411-430.

Wiles, Philip J., Tom P. Rippeth, John H. Simpson, and Peter J. Hendricks. "A novel technique for measuring the rate of turbulent dissipation in the marine environment." Geophysical Research Letters 33, no. 21 (2006).

Willmott, A. J., & Edwards, P. D. (1987). A numerical model for the generation of tidally forced nonlinear internal waves over topography. Continental Shelf Research, 7(5), 457-484.

Wunsch, C. (1999). Where do ocean eddy heat fluxes matter? *Journal of Geophysical Research: Oceans*, *104*, 13235-13249. doi:10.1029/1999JC900062

Zappa, Christopher J., Wade R. McGillis, Peter A. Raymond, James B. Edson, Eric J. Hintsa, Hendrik J. Zemmelink, John WH Dacey, and David T. Ho. "Environmental turbulent mixing controls on air-water gas exchange in marine and aquatic systems." Geophysical Research